In this work spin polarized currents were observed and studied in various low dimensional semiconductor systems under excitation with THz radiation. The measurements demonstrate that the microscopic origin of the photocurrents is the asymmetric spin-dependent scattering, which results in a spatial separation of electrons with opposite spins. During the spin separation a spin current flows, which is transformed into a net electric current by the application of an external magnetic field. This effect, known as the MPGE, was observed in different types of low dimensional GaAs structures and DMS (CdMn) Te QWs. Besides the fundamental question on the origin of the spin current formation, the variation of the inversion asymmetry in low dimensional systems, which is of particular interest for spintronics related research, was studied. To achieve this goal, spin polarized currents have been utilized as an experimental access to the inversion asymmetry.

Universitätsverlag Regensburg

ISBN 978-3-86845-068-2

gefördert von:

Alumni der physikalischen Fakultät der Universität Regensburg e.V.

Universität Regensburg

Dissertationsreihe Physik - Band 18

Peter Olbrich

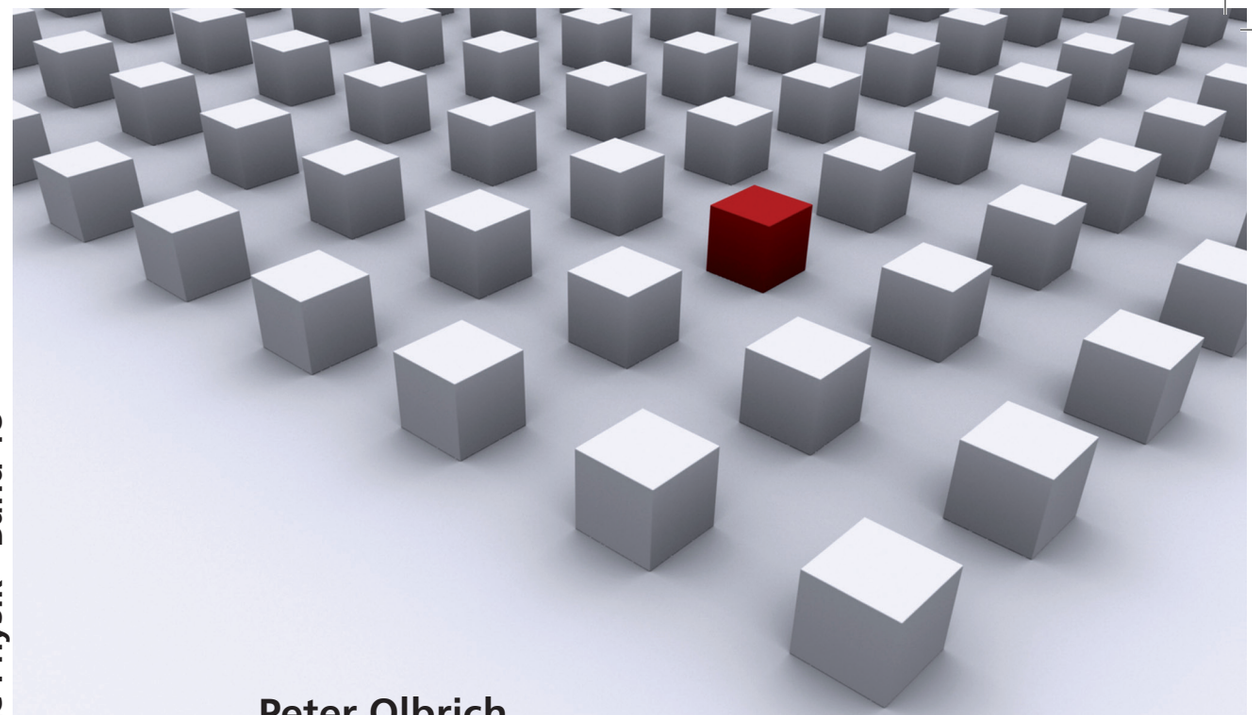

Peter Olbrich

THz radiation induced spin polarized currents in low dimensional semiconductor structures

Universitätsverlag Regensburg

18 Dissertationsreihe Physik

Peter Olbrich

THz radiation induced spin polarized currents in low dimensional semiconductor structures

THz radiation induced spin polarized currents in low dimensional semiconductor structures

Dissertation zur Erlangung des Doktorgrades der Naturwissenschaften (Dr. rer. nat.) der naturwissenschaftlichen Fakultät II - Physik der Universität Regensburg vorgelegt von

Peter Olbrich

aus Regensburg
Juni 2010

Die Arbeit wurde von Prof. Dr. Sergey D. Ganichev angeleitet.
Das Promotionsgesuch wurde am 22.06.2010 eingereicht.
Das Kolloquium fand am 22.07.2010 statt.

Prüfungsausschuss:
Vorsitzender: Prof. Dr. Gunar Bali
1. Gutachter: Prof. Dr. Sergey D. Ganichev
2. Gutachter: Prof. Dr. Christian Schüller
weiterer Prüfer: Prof. Dr. Franz Giessibl

Dissertationsreihe der Fakultät für Physik der Universität Regensburg, Band 18

Herausgegeben vom Präsidium des Alumnivereins der Physikalischen Fakultät:
Klaus Richter, Andreas Schäfer, Werner Wegscheider, Dieter Weiss

Peter Olbrich

THz radiation induced spin polarized currents in low dimensional semiconductor structures

Universitätsverlag Regensburg

Bibliografische Informationen der Deutschen Bibliothek.
Die Deutsche Bibliothek verzeichnet diese Publikation
in der Deutschen Nationalbibliografie. Detailierte bibliografische Daten
sind im Internet über http://dnb.ddb.de abrufbar.

1. Auflage 2010
© 2010 Universitätsverlag, Regensburg
Leibnitzstraße 13, 93055 Regensburg

Konzeption: Thomas Geiger
Umschlagentwurf: Franz Stadler, Designcooperative Nittenau eG
Layout: Peter Olbrich
Druck: Docupoint, Magdeburg
ISBN: 978-3-86845-068-2

Alle Rechte vorbehalten. Ohne ausdrückliche Genehmigung des Verlags ist es nicht gestattet, dieses Buch oder Teile daraus auf fototechnischem oder elektronischem Weg zu vervielfältigen.

Weitere Informationen zum Verlagsprogramm erhalten Sie unter:
www.univerlag-regensburg.de

THz radiation induced spin polarized currents in low dimensional semiconductor structures

DISSERTATION ZUR ERLANGUNG DES DOKTORGRADES DER NATURWISSENSCHAFTEN (DR. RER. NAT.)
DER FAKULTÄT II - PHYSIK

DER UNIVERSITÄT REGENSBURG

vorgelegt von

Peter Olbrich

aus
Regensburg

im Jahr 2010

Promotionsgesuch eingereicht am: 22.06.2010
Die Arbeit wurde angeleitet von: Prof. Dr. Sergey D. Ganichev

Prüfungsausschuss: Vorsitzender: Prof. Dr. Gunar Bali
1. Gutachter: Prof. Dr. Sergey D. Ganichev
2. Gutachter: Prof. Dr. Christian Schüller
weiterer Prüfer: Prof. Dr. Franz Giessibl

Contents

List of Figures

List of Tables

1 Introduction

In recent years spintronics became a fast growing research area in solid state physics, aimed to revolutionize the information and communication technology. While the procession of digital signals using charge currents consumes electric power the utilization of the spin degree of freedom of an electron constitutes a dissipation less spin current. The task is to find new spintronic materials and to improve techniques to produce spin-based devices, allowing injection, control, transport, manipulation and detection of spin-polarized carrier flows [1, 2].

Promising systems for spintronics applications are low dimensional gyrotropic semiconductor structures, which due to the spin-orbit coupling can be utilized to generate and manipulate the spin degree of freedom. This effect has an important consequence as it influences the splitting of the conduction band or the spin relaxation according to the D'yakonov-Perel' mechanism [1–5]. Furthermore, it allows the manipulation of spins via an electric field as well as a generation of a nonequilibrium spin polarization by an electric current [2, 4, 6–15]. Another effect of spin-orbit coupling in low-dimensional semiconductor structures is the possibility to excite spin currents, which constitute oppositely directed flows of spin-up and -down electrons of equal strength. Resulting from the fact that both charge flows with different spin compensate each other, the total electric current emerged in the system is zero. However, this still causes a spatial separation and accumulation of spin-up and -down carriers at the sample edges. Pure spin currents can be generated in low-dimensional or inversion asymmetric bulk semiconductor in different ways. For instance, recently it has been demonstrated electrically with the spin Hall effect or optically via interband optical transitions [2, 4, 15–17]. To the same time another root of pure spin currents, namely the zero-bias spin separation, was observed in gyrotropic semiconductor structures and attracted growing attention [18]. This effect yields spin currents, which in contrast to the spin Hall effect do not need an electric current to flow. It is a consequence of asymmetric spin-dependent scattering and can be obtained using different methods leading to a nonequilibrium state of a two-dimensional electron gas (2DEG).

This work is aimed to the investigation of this novel phenomena and to explore its origin. In particular, various roots of the conversion of pure spin currents into an electric current will be studied. Here terahertz (THz) radiation is used to induce electron gas heating by means of Drude absorption, followed by spin dependent energy relaxation. However, most recently we demonstrated that even microwave radiation can be applied for the spin current generation, linking opto-electronics to transport. In gyrotropic media the Drude absorption itself becomes spin-dependent. It will be shown that this process yields a spin separation because it involves electron scattering by phonons, static defects, etc. [18]. To convert the pure spin current into a measurable electric current the Magnetogyrotopic PhotoGalvanic Effect (MPGE) is utilized [19, 20]. It is based on the Zeeman spin splitting of the conduction band electrons, which is induced by an external magnetic field and thus, leads to a difference between the oppositely propagating spin polarized carrier flows. Since the electric current is given by the sum of both spin currents, a detectable signal arises, which is in first order proportional to the applied magnetic field and the effective g^*-factor.

At the beginning of this work the microscopic pictures and phenomenological equations for the zero-bias spin separation and the MPGE have been developed and verified in (001)-grown GaAs quantum well (QW) structures. However, these experiments raised a lot of open questions on the current formation. They concern the role of the Bulk Inversion (BIA) and Structure Inversion Asymmetry (SIA) as well as the interplay of spin and orbital effects. This work is aimed to clarify these open questions and is organized as follows. Chapter 2 introduces the theoretical background and includes various aspects of spin-dependent properties of 2DEGs. Chapter 3 is devoted to the description of the generation of THz radiation, the experimental techniques and the experimental setup, as well as the investigated samples. The influence of Rashba and Dresselhaus spin splitting, which originate from SIA and BIA, as well as their dependence on the symmetry of n-doped (110)-grown GaAs QWs is analyzed in Chapter 4. Chapter 5 is aimed to the investigation of spin polarized currents in dependence on the g^*-factor. To achieve this goal n-doped (001)-grown diluted magnetic semiconductors (DMS) QWs were applied, in which the g^*-factor is strongly enhanced by the temperature as well as the exchange

interaction between the conduction band electrons and the magnetic ions. It will be demonstrated that the manipulation of the g^*-factor changes the Giant Zeeman splitting of the conduction band. This is reflected in the MPGE and results in a strong variation of the spin polarized electric current, supporting the spin dependent origin of this effect. As addressed above, the photogalvanic effects strongly depend on the symmetry of the investigated system. In Chapter 6 a method is used to controllably change the symmetry by a lateral periodic potential, etched into the surface of (001)-grown GaAs QWs. These samples open a new and promising access to the generation of magnetic field independent and dependent photogalvanic effects.

2 Theoretical basics

This chapter presents the theoretical background and introduces the basic phenomenological equations as well as the microscopic pictures, which are necessary to explain the experimental results of this work. It starts with the discussion of gyrotropy: a fundamental requirement, which is connected to the symmetry of the investigated system. Further, the spin-orbit interaction in gyrotropic semiconductor structures, which results in a linear in wavevector $\boldsymbol{k}$ and spin $\boldsymbol{\sigma}$ contribution to the Hamiltonian, is addressed. These additional parts are known as Rashba/Dresselhaus terms. Another effect of the spin-orbit interaction are $\boldsymbol{k}$-linear terms in the scattering. This is reflected in the zero-bias spin separation, which describes the generation of spin currents resulting from asymmetric processes in the absorption and relaxation of a gyrotropic 2DEG. By means of an external magnetic field the opposite propagating spin flows can be converted into a measurable electric current applying the magnetogyrotropic photogalvanic effect. Since the experimental data are supported by time-resolved Kerr rotation measurements, determining the symmetry of the samples by studying spin dephasing of spin oriented carriers, spin relaxation processes are addressed. In addition, the effect of magnetic ions in semiconductor heterostructures, increasing the conversion of pure spin currents into an electric current, is investigated. Therefore, basic properties of diluted magnetic semiconductors are discussed. Apart from the MPGE the excitation of low-dimensional systems with THz radiation can lead to photocurrents, which should be taken into account in the discussion of the results aimed to the understanding of the zero-bias spin separation and the MPGE. These magnetic field independent photogalvanic effects are introduced and described by their corresponding phenomenological equations.

2.1 Gyrotropy

Gyrotropic media allow a coupling between an axial A_m and polar vector P_l, interconnected by a second rank pseudo tensor M_{lm}, given by $P_l = M_{lm}A_m$. This means that the corresponding point group symmetries do not distinguish between certain components of polar vectors, like an electric current or electron

momentum, and axial vectors, like the spin or magnetic field [21–23]. The well known effects of gyrotropic media are reflected in a linear in light or electron wave vector $\boldsymbol{k}$ spatial dispersion resulting in optical activity (gyrotropy) or Rashba/Dresselhaus band spin-splitting in semiconductor structures, respectively [21, 23–26].

A fundamental, but not sufficient requirement for such a media is the lack of inversion symmetry. This case is described by 21 non-centrosymmetric crystal classes. From them only the point groups T_d, C_{3h} and D_{3h} are non-gyrotropic. The 18 remaining gyrotropic crystal classes can be further decomposed into 7 non-enantiomorphic (C_s, C_{2v}, C_{3v}, S_4, D_{2d}, C_{4v} and C_{6v}) and 11 enantiomorphic (chiral) classes. The latter group is characterized by an absence of reflection planes or rotation-reflection axes [21, 25, 26]. Often it is misleading stated that gyrotropy (optical activity) can be obtained only in non-centrosymmetric crystals without mirror reflection planes. In fact, it is possible in the 7 non-enantiomorphic classes, as well as they allow for instance, the spin orientation by electric current [8, 9].

2.2 Spin-Orbit Interaction

All mechanisms discussed in this work are based on the spin-orbit interaction, which is usually calculated relativistically and quantum mechanically. It can be visualized in a non-relativistic way leading to a similar result, which differs only in the value of the pre-factor and the electron magnetic moment. A charged particle moving with a velocity $\boldsymbol{v}$ in an external electric field $\boldsymbol{E}$ feels the influence of a magnetic field $\boldsymbol{B} = (1/c)\boldsymbol{E} \times \boldsymbol{v}$. The strength of this electric field induced from the atoms nuclear charge increases with their weight and thus gives rise to the magnetic field acting on the spin of an electron. Both $\boldsymbol{v}$ and $\boldsymbol{E}$ lay in the plane of the orbital movement, whereas $\boldsymbol{B}$ is parallel to the angular moment $\boldsymbol{L}$ of the orbit. It introduces an energy difference dependent on the orientation of the electron spin with respect to $\boldsymbol{B}||\boldsymbol{L}$. This effect, which is due to spin-orbit interaction, can be written as $A(\boldsymbol{LS})$, where A depends on the electrons state in the atom, and can be mediated by any electric field. Furthermore, it influences the splitting of atomic levels, known as fine structure, which increases with the weight of the atoms [4].

2.2.1 Spin-Orbit Interaction and Optical Orientation

In semiconductors the spin-orbit interaction has a strong effect on the valence band and is necessary to describe the band structure. Without this interaction the valence band at the $\Gamma-$point, described by a p-type wave function, is 3-fold degenerated, or 6-fold taking into account spin degeneracy. Including the spin-orbit coupling allows the electron to interact with the magnetic field resulting from its orbital motion. Thus, the 6-fold degeneracy breaks apart into a 4- and a 2-fold degeneracy, noted as Γ_8 and Γ_7, respectively. The 4-fold degenerate states (total angular momentum $j = 3/2$) are located on top of the valence band. They consist of the heavy hole (HH) and the light hole (LH) band, where the latter one is characterized by a stronger curvature. The 2-fold degenerate levels ($j = 1/2$) form the split-off band (SO), which is separated by the energy gap Δ_{SO}. The minima of the s-type conduction band states (Γ_6) in a direct gap semiconductor are separated by the band gap E_g from the highest valence band level, shown in Fig. 1(a) [14, 27, 28]. In a 2D system however, the degeneracy of the LH and HH states is lifted and the LH states drop energetically below the HH [15].

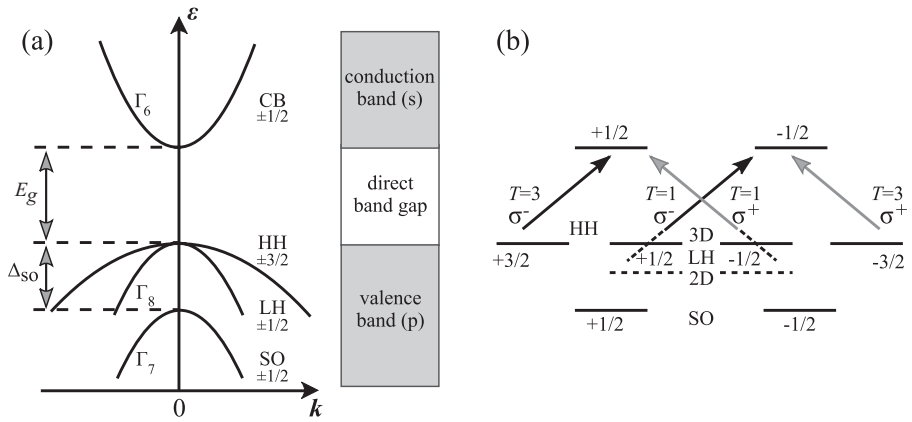

Figure 1: (a) Band structure of a direct gap semiconductor close to the Γ-point ($\boldsymbol{k} = 0$). (b) Selection rules between the conduction band and the valence band states. The relative transmission rates T are given for the optical transitions with circularly polarized light. For the 3D bulk semiconductor the HH and LH states are degenerate, while for the 2D case the LH energy is lower than the HH.

Thus, the spin-orbit interaction gives rise to the possibility of optical orientation of electrons in a 3D bulk material and is even more effective in 2D systems [5, 15]. Here by means of left (right) circularly polarized light an angular momentum of -1 (+1) can be transferred to the electron. This allows to achieve a high degree of spin polarization P taking into account angular momentum and energy conservation laws. While for bulk systems the maximum achievable value is $P = 50\%$ ($P \approx 25\%$ considering recombination processes), the energy difference between HH and LH states allows theoretically $P = 100\%$. The transitions from the Γ-point and their rates are shown in Fig. 1(b), here the 2D case is illustrated with dashed lines [14, 15].

The spin-orbit interaction allows not only optical spin orientation in semiconductors it influences the effective g^*-factor of electrons and other phenomena as well. In the former case it changes the g^*-factor and thus affects the Zeeman splitting, which is proportional to g^* [14, 15]. Furthermore, the spin-orbit interaction gives rise to spin splitting of the bulk energy dispersion.

2.2.2 SIA and BIA in (001)-grown low dimensional structures

While the above phenomena do not have a strong symmetry restriction the below discussed bulk and structure inversion asymmetry only exist in gyrotropic media. The spin degeneracy of electron and hole states is usually described by $E_\uparrow(\boldsymbol{k}) = E_\downarrow(\boldsymbol{k})$ at $B = 0$ and is a result of a combined effect of the space inversion symmetry ($E_\uparrow(\boldsymbol{k}) = E_\uparrow(-\boldsymbol{k})$) and time inversion symmetry ($E_\uparrow(\boldsymbol{k}) = E_\downarrow(-\boldsymbol{k})$). The Kramers doublets are lifted only if the time inversion symmetry is broken, like in the case of an external magnetic field $\boldsymbol{B}$. As a consequence of the spin-orbit interaction in bulk semiconductors without an inversion center, the space inversion symmetry and thus spin degeneracy is lifted even in the absence of an external magnetic field. The effect of spin splitting in bulk materials is described by cubic in $\boldsymbol{k}$ Dresselhaus terms in the Hamiltonian. For the case of gyrotropic systems, like zinc-blende structure based low-dimensional heterostructures, different spin-dependent $\boldsymbol{k}$-linear terms appear in the electron 2D Hamiltonian. These $\boldsymbol{k}$-linear terms originate from the $\boldsymbol{k}$-cubic spin-orbit induced Dresselhaus coupling terms of the bulk material and are a result of the bulk inversion asymmetry. A further contri-

bution is the structure inversion asymmetry. It is independent on the crystal lattice and stems either from the asymmetry of the structure induced during the growth or from external parameters, like for instance an applied electric field or strain. The resulting $\boldsymbol{k}$-linear terms are known as Rashba terms. A third contribution is given by the asymmetry of the Interfaces (IIA), which can be neglected or accounted to BIA, because it shows phenomenologically a similar behavior. In the following only SIA and BIA are discussed, as they are the main terms contributing to the spin splitting.

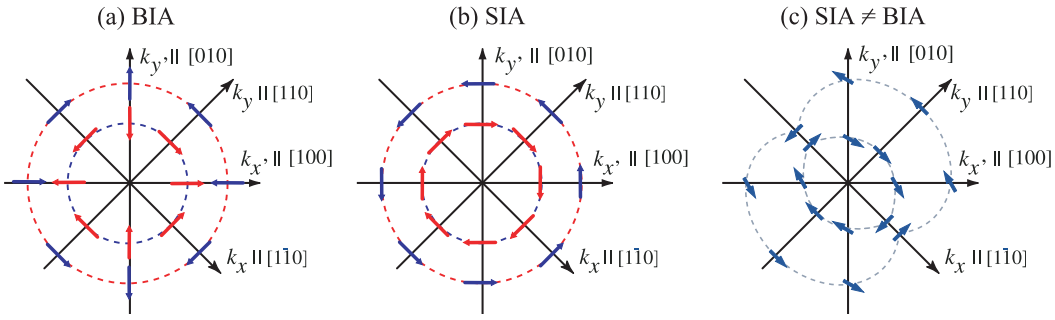

Figure 2: (a) BIA and (b) SIA in (001) grown zinc-blende type QWs. (c) Superposition of SIA and BIA for the case of BIA ≠ SIA.

For (001)-grown 2-dimensional structures the Hamilton operator, caused by SIA and BIA (H_{SO}^{SIA} and H_{SO}^{BIA}, respectively), are given in a coordinate system along the cubic axis $x' \parallel [100]$ and $y' \parallel [010]$ given by

$$H_{SO}^{\mathrm{SIA}} = \beta^{\mathrm{SIA}}(\sigma_{x'} k_{y'} - \sigma_{y'} k_{x'}), \tag{1}$$

$$H_{SO}^{\mathrm{BIA}} = \beta^{\mathrm{BIA}}(\sigma_{x'} k_{x'} - \sigma_{y'} k_{y'}). \tag{2}$$

The rotation of the x'- and y'-axis around 45°, resulting in $x \parallel [1\bar{1}0]$ and $y \parallel [110]$ parallel to the crystallographic axis, remains the form of the SIA induced terms, compare Eqs. (1) and (3). It is a result of the rotational symmetry of the in-plane Rashba spin splitting, induced by an electric field along the growth direction of the heterostructure. In contrast, the BIA induced terms H_{SO}^{BIA} described by Eqs. (2) and (4) strongly depend on the coordinate

frame. SIA and BIA described in the coordinate system x, y and z are given by

$$H_{SO}^{\mathrm{SIA}} = \beta^{\mathrm{SIA}}(\sigma_x k_y - \sigma_y k_x), \tag{3}$$

$$H_{SO}^{\mathrm{BIA}} = \beta^{\mathrm{BIA}}(\sigma_x k_y + \sigma_y k_x). \tag{4}$$

The resulting spin splitting of H_{SO}^{BIA} and H_{SO}^{SIA}, as shown in Fig. 2(a) and 2(b) can be represented by an effective in-plane magnetic field $B_{eff}(k) = B_{eff}^{\mathrm{SIA}}(k) + B_{eff}^{\mathrm{BIA}}(k)$. Figure 2(c) shows the case of $\beta^{\mathrm{SIA}} \neq \beta^{\mathrm{BIA}}$ resulting in a superposition of both terms [29]. For the case of $\beta^{\mathrm{SIA}} = \beta^{\mathrm{BIA}}$ ($\beta^{\mathrm{SIA}} = -\beta^{\mathrm{BIA}}$) the effective magnetic field $B_{eff}(k)$ points along the axis $x \parallel [1\bar{1}0]$ ($y \parallel [110]$) and allows a considerable long spin relaxation time for spins aligned in the $x-$ (y-)direction.

2.3 Magnetogyrotropic Photogalvanic Effect

The MPGE is a photogalvanic effect, which arises in the presence of an external magnetic field under excitation with polarized and unpolarized radiation. It is allowed in gyrotropic media only. The application of an external magnetic field converts pure spin currents resulting from the zero-bias spin separation into an electric current. This chapter includes the description of the fundamental theory and microscopic picture of the MPGE in (001)-grown GaAs heterostructures [18, 30]. During this work it has been demonstrated that the current resulting from the MPGE can be further separated to yield information about the strength of Rashba and Dresselhaus spin splitting in different materials and growth directions [19, 20, 31, 32].

2.3.1 Phenomenological theory of the MPGE

The direction of the magnetic field induced photocurrent, its magnitude as well as its dependence on the radiation polarization state and the magnetic field with respect to the crystallographic axes is described by the phenomenological theory of the MPGE. This theory does not require the knowledge of the involved microscopic mechanism, because it operates with measurable physical quantities.

The phenomenological equation describing the MPGE [30] within a linear approximation in the magnetic field strength $\boldsymbol{B}$ and assuming normal incident radiation is given by

$$j_\alpha = \sum_{\beta\gamma\delta} \phi_{\alpha\beta\gamma\delta}\, B_\beta\, I\, \frac{\left(e_\gamma e_\delta^* + e_\delta e_\gamma^*\right)}{2} + \sum_{\beta\gamma} \mu_{\alpha\beta\gamma} B_\beta \hat{e}_\gamma I P_{\mathrm{circ}}. \tag{5}$$

Here $\boldsymbol{\phi}$ is a fourth rank pseudo-tensor being symmetric in the last two indices, $\boldsymbol{e} = \mathbf{E}/|\mathbf{E}|$ the (complex) unit vector of the light polarization, $\mathbf{E}$ the radiation electric field, $\hat{\boldsymbol{e}}$ the unit vector pointing in the light propagation direction, I the radiation intensity and P_{circ} the radiation circular polarization degree. The first term on the right side of Eq. (5) including the pseudo-tensor $\boldsymbol{\phi}$ describes the photocurrent which can be induced by unpolarized and linearly polarized radiation. The helicity dependent contribution to the photocurrent is represented by the second term containing the third rank tensor $\boldsymbol{\mu}$. A characteristic sign for the latter part is a change of sign in the samples response upon switching the helicity of the circular polarization.

The description of the MPGE in (001)-grown heterostructures is based on the phenomenological Eq. (5) taking into account the corresponding point group of the investigated samples. QWs grown along this direction can be separated into two groups: symmetric structures, which belong to the D_{2d} and asymmetric structures, associated with the C_{2v} symmetry. The phenomenological equations for both systems look quite similar and differ only in the relation between the parameters S_1 to S_4 and S_1' to S_4', which result from the non-vanishing components of the tensors $\phi_{\alpha\beta\gamma\delta}$ and $\mu_{\alpha\beta\gamma}$. In the case of (001)-grown asymmetric QW structures Eq. (5) reduces to [30]

$$\begin{aligned} j_x/I = {} & S_1 B_y + S_2 B_y \left(|e_x|^2 - |e_y|^2\right) + S_3 B_x \left(e_x e_y^* + e_y e_x^*\right) \\ & + S_4 B_x P_{\mathrm{circ}}, \end{aligned} \tag{6}$$

$$\begin{aligned} j_y/I = {} & S_1' B_x + S_2' B_x \left(|e_x|^2 - |e_y|^2\right) + S_3' B_y \left(e_x e_y^* + e_y e_x^*\right) \\ & + S_4' B_y P_{\mathrm{circ}}, \end{aligned} \tag{7}$$

and is described in the coordinate system given by

$$x \parallel [1\bar{1}0],\ y \parallel [110],\ z \parallel [001]. \tag{8}$$

The first part on the right side of Eqs. (6) and (7) described by S_1 and S_1' emerges a polarization independent current, only proportional to the strength of the magnetic field $\boldsymbol{B}$. The other fractions clearly show a dependence on the light's polarization, which allow in combination with the magnetic field orientation to separate the parameters $S_1...S_4$ and $S_1'...S_4'$ experimentally.

2.3.2 Microscopic model of the MPGE

The microscopic model describing the MPGE has been developed to explain this effect in (001)-grown GaAs QWs. This model can be applied as well to (001)-grown InAs-based QWs, (110)-oriented GaAs QWs and (001)-grown (CdMn)Te DMS structures. It is based on a spin-dependent asymmetry in the electron scattering, leading to the zero-bias spin separation under Drude absorption [18, 20, 33]. The presence of spin-orbit interaction, allowed in gyrotropic media, like the investigated QWs, yields an additional asymmetric spin-dependent term, which is linear in the wave vector $\boldsymbol{k}$ and Pauli spin matrices $\boldsymbol{\sigma}$, to the scattering matrix elements, given by

$$\begin{aligned} \hat{V}_{\mathrm{el-phon}}(\boldsymbol{k}', \boldsymbol{k}) &= \Theta_c \sum_j \varepsilon_{jj} + \Theta_{cv} \xi \sum_j \left[(\boldsymbol{k}' + \boldsymbol{k}) \times \boldsymbol{\sigma}\right]_j \varepsilon_{j+1\ j+2}, \qquad (9) \\ \xi &= \frac{i\hbar V_{cv}}{3m^*} \frac{\Delta_{\mathrm{so}}}{E_{\mathrm{g}}(E_{\mathrm{g}} + \Delta_{\mathrm{so}})}. \end{aligned}$$

Equation (9) shows the scattering matrix element of the electron-phonon interaction $\hat{V}_{\mathrm{el-phon}}(\boldsymbol{k}', \boldsymbol{k})$ including the intraband and interband constants Θ_c and Θ_{cv}, the phonon-induced strain tensor $\epsilon_{jj'}$, which is dependent on the phonon wavevector $\boldsymbol{q} = \boldsymbol{k}' - \boldsymbol{k}$. The term ξ, which has especially for zinc-blende based QWs the form shown in Eq. (9), includes the effective mass m^* of the free electrons, the bandgap E_{g}, the spin-orbit-splitting of the bulk-semiconductors valence band Δ_{so} and the interband matrix element $V_{cv} = \langle S|\hat{p}_z|Z\rangle$ of the momentum operator. Microscopically Eq. (9) is a result of BIA and SIA and thus reflects both contributions in the scattering.

As in non-gyrotropic media the absorption of radiation usually results in an equilibrium distribution of heated electrons, the asymmetric scattering in gyrotropic media leads to different scattering rates from the lower states to their

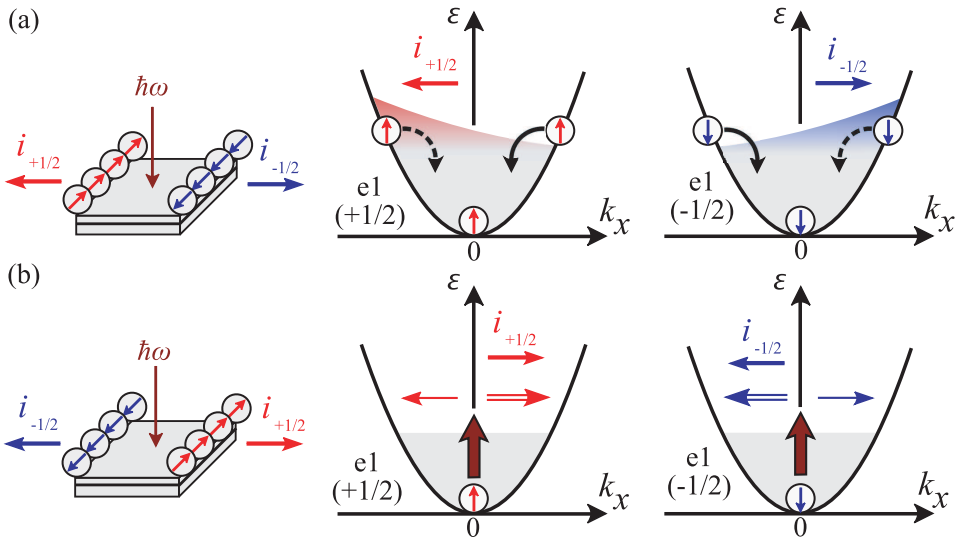

Figure 3: Asymmetry in (a) the relaxation process of a homogeneous heated electron gas and (b) the excitation via Drude absorption. The tilted shadowed areas indicate schematically the non-equilibrium distribution of states with positive and negative $\boldsymbol{k}$.

final states $\mathbf{k}_f$ and $-\mathbf{k}_f$ in a subband [18]. In the spin-up and spin-down subbands the scattering assisted photoexcitation of carriers due to Drude-like absorption causes spin currents of equal strength propagating in opposite directions so that the total electric current is zero, schematically shown in Fig. 3(b).

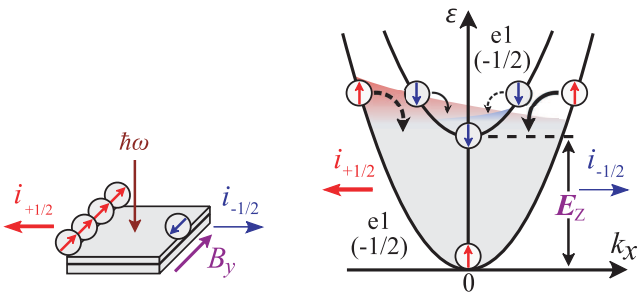

Figure 4: Asymmetry in the relaxation process of a homogeneous heated electron gas in the Zeeman splitted subbands. The tilted shadowed areas indicate schematically the non-equilibrium distribution of states with positive and negative $\boldsymbol{k}$.

The Zeeman effect, which is induced by an external magnetic field, separates the spin-up and -down subbands energetically and disturbs the balance of the carrier distribution of both types. As a result of this, the pure spin current is transformed into an measurable electric current dependent on the magnetic field strength. This effect is schematically shown in Fig. 4 and has been experimentally observed for the first time in (001)-oriented GaAs QWs [30]. The photocurrent due to the relaxation mechanism [schematically shown in Fig. 3(a)] is independent on the polarization state of the incident radiation. In the same way the asymmetric scattering modifies the energy relaxation it influences the excitation process of the photoexcited carriers gas. The electric current, resulting from the latter mechanism, carries a characteristic polarization dependence.

2.4 Spin relaxation times and relaxation mechanisms

Spin relaxation plays an important role in the discussion of the experimental results. It is of particular interest for the understanding of the results obtained from time-resolved Kerr rotation and how they are linked to the sample's symmetry. Thus, in the following a general description of spin relaxation is introduced and the for this work main relaxation processes are described. In fact, four mechanisms of spin relaxation in semiconductors exist, generally the D'yakonov-Perel', Elliot-Yafet, Bir-Aronov-Pikus and specially for (110)-grown QWs the spin dephasing mechanism due to intersubband scattering [34–38]. This section is mainly focused on the description of the D'yakonov-Perel' spin relaxation, since it is the dominating relaxation mechanism in most of the investigated samples.

2.4.1 D'yakonov-Perel' Mechanism

An inertially spin polarized electron gas underlies, e.g. due to the presence of a magnetic field $\boldsymbol{B}$ whose magnitude or orientation changes in time, different relaxation processes. In the case of low dimensional gyrotropic heterostructures the spin polarization is affected by an effective magnetic field $B_{eff}(k)$ resulting from BIA and SIA.

Generally speaking a spin which precesses around a magnetic field $\boldsymbol{B}$ with a rotation frequency ω is tilted from its initial orientation. After a time τ_c (correlation time) the alignment of $\boldsymbol{B}$ changes randomly and the spin is forced to rotate around the new direction of $\boldsymbol{B}$, which leads to a loss of the initial spin within a few cycles. This process increases with the dimensionless product $\omega\tau_c$ of the magnetic field induced rotation frequency and the switching (correlation) time.

The common situation is $\omega\tau_c << 1$, where the spin experiences only a very slow rotation and a very short correlation time. By $t/\tau_c = n$ the number of field switchings in the time t is given, in which the spin is tilted n-times around the squared precession angle $(\omega\tau_c)^2$. The initial orientation is lost in any case if the spin is rotated around $90° = \pi/2$, but for simplicity it is enough to set the product $(\omega\tau_c)^2(t/\tau_c) = 1$. From this the spin relaxation time τ_s can be estimated

$$\frac{1}{\tau_s} \approx \omega^2\tau_c. \tag{10}$$

The second case is $\omega\tau_c >> 1$, in which the precession frequency is high compared to τ_c and the spin rotates many times around the magnetic field. While the spin perpendicular to $\boldsymbol{B}$ vanishes rapidly, the parallel component remains for $t < \tau_c$. After the magnetic field is realigned, the spin polarization is lost completely. Thus the spin relaxation time for this process is proportional to the correlation time, $\tau_s \propto \tau_c$ [4].

The D'yakonov-Perel' (DP) Mechanism is the main spin relaxation process at high temperature and is greatly enhanced, if the dimensionality of the system is reduced from 3D to 2D, where it dominates the relaxation for n-doped QWs [3,39]. It describes the loss of the spin orientation between scattering events in the presence of a $\boldsymbol{k}$-dependent spin splitting of the electron subband and is valid in the collision dominated limit $\omega\tau << 1$ for a spin which precesses around an effective magnetic field $\boldsymbol{B}_{eff}(\boldsymbol{k})$. After a scattering event the alignment of $\boldsymbol{B}_{eff}(\boldsymbol{k})$ has changed and thus, forces the spin to rotate in a different direction. Similar to the common case described above, the spin relaxation time τ_s reduces

for a stronger precession $\boldsymbol{\Omega_k}$ or longer momentum relaxation times τ, described by

$$\frac{1}{\tau_s} \propto \left\langle \boldsymbol{\Omega}_{\boldsymbol{k}}^2 \tau \right\rangle , \tag{11}$$

where the brackets mean an averaging over the electron energy distribution. Replacing τ in Eq. (11) by a temperature dependent parameter τ^*, which similarly to the momentum relaxation time τ_p can be obtained by Hall mobility measurements, yields the temperature dependent spin relaxation time, given by

$$\frac{1}{\tau_s} = \Omega_0^2 \tau^*, \tag{12}$$

including the effective Larmor frequency Ω_0 at the Fermi energy at $T = 0$ K. In addition, it has been shown experimentally and theoretically that even electron-electron scattering contributes to the DP mechanism as well as any other scattering processes of carriers [3].

2.4.2 Elliot-Yafet, Bir-Aronov-Pikus and Intersubband Scattering Relaxation Mechanism

Besides the dominating D'yakonov-Perel' mechanism three other processes may contribute to the spin relaxation, the Elliot-Yafet (EY), the Bir-Aronov-Pikus (BAP) and the Intersubband Scattering Relaxation (ISR) mechanism [35–38].

The EY mechanism is a electron spin-flip scattering, which results from $\boldsymbol{k}$-dependent admixture of valence-band states to the conduction band wave function. This effect increases with the strength of spin-orbit coupling, which relates the spin relaxation times of the carriers with its momentum relaxation times. Thus, the EY mechanism contributes strongly to the spin relaxation in bulk narrow gap semiconductors, like InSb. For *bulk semiconductors* the spin relaxation time due to the EY mechanism is given by

$$\frac{1}{\tau_s(E_e)} \approx \left(\frac{\Delta_{\mathrm{SO}}}{E_g + \Delta_{\mathrm{SO}}}^2 \right) \left(\frac{E_e}{E_g} \right)^2 \frac{1}{\tau_p(E_e)}, \tag{13}$$

where Δ_{SO} is the spin-orbit coupling of the valence band, E_e is the electron kinetic energy, E_g is the band gap and the ratio $\frac{E_e}{E_g}$ is a size for the admixture of

the valence and conduction band wavefunction. In the case of *QW structures* Eq. (13) transforms to

$$\frac{1}{\tau_s(E_e)} \approx \left(\frac{\Delta_{\mathrm{SO}}}{E_g + \Delta_{\mathrm{SO}}}\right)^2 \left(\frac{E_{e1}E_e}{{E_g}^2}\right) \frac{1}{\tau_p(E_e)}, \tag{14}$$

showing that the EY mechanism is proportional to the quantum-confinement energy E_{e1} [3].

The BAP Mechanism represents a relaxation process, in which the spin polarization of conduction electrons vanishes due to a scattering by holes in p-doped samples and is important for band-band excitation. It is a spin-flip of photoexcited electrons as a result of a electron-hole exchange interaction and prevails at low temperatures as well as a moderate density of holes [3]. The holes appear as a result of doping or due to interband optical excitation [4].

The recently observed ISR describes a decrease of the spin relaxation of spins oriented along the [110]-direction in (110)-grown GaAs structures at elevated temperatures. It is based on the scattering of electrons between different quantum well subbands. This mechanism may contribute to the spin relaxation times measured in (110)-grown samples [38].

2.5 Magnetic ions in diluted magnetic semiconductor

As a part of this work comprises experiments with diluted magnetic semiconductors the crystal structure as well as the main electronic and optical properties of this material system are described in this chapter. CdTe belongs similar to GaAs to the zinc-blende type crystals, but is a II-VI semiconductor. If Mn is implemented during the growth, the Cd atoms in the lattice will be replaced randomly and new magnetic properties of this composition arise, dependent on the concentration x of the Mn^{2+} cations. Therefore, the resulting $Cd_{1-x}Mn_xTe$ compound is associated to the group of DMS.

2.5.1 Crystal structure and electronic properties

Dependent on the concentration x, $Cd_{1-x}Mn_xTe$ has different optical, electric and magnetic properties compared to the non-magnetic CdTe. For $0 < x \leq$

0.77 this material crystallizes in the zinc-blende structure and for $x > 0.77$ it adopts the crystal structure of the host material MnTe, known as NiAs structure, which is neither zinc-blende nor wurzite. Quantitatively the band structure increases linearly with x, given by [40]

$$\begin{aligned} E_g(300\text{ K}) &= (1.528 + 1.316x)\text{ eV}, \\ E_g(4.2\text{ K}) &= (1.606 + 1.592x)\text{ eV}. \end{aligned} \tag{15}$$

Over a wide range of x, $Cd_{1-x}Mn_xTe$ is a direct semiconductor with a minimum at the Γ point ($\boldsymbol{k} = 0$), allowing a parabolic approximation of the band [41]. As Mn^{2+} replaces Cd^{2+} (both contribute their $4s^2$ electrons to the binding with Te^{2-}), the magnetic ions do not add electrons or holes to the system, in contrast to the III-V semiconductor GaAs, where it acts as an acceptors and results in a p-doping. The d-shell of Manganese is compared to Cadmium only half filled and the occupied levels ($e_d^{+\sigma}$) in the valence band and the unoccupied ($e_d^{-\sigma}$) in the conduction band of the $3d^5$ shells are split-off energetically by $E_{eff} \approx 7$ eV. Thus, Mn remains electrically neutral in $Cd_{1-x}Mn_xTe$, because this splitting is much larger than the band gap E_g and the semiconducting properties of DMS in zero magnetic field look quite similar to those of non-magnetic CdTe [40].

2.5.2 Magnetic properties

While Manganese is electrically neutral in the compound $Cd_{1-x}Mn_xTe$, the presence of its half filled $3d$ shell is responsible for the magnetic properties of this material. According to Hund's rule, the spins of the five electrons in the ground state of this d shell have to be aligned parallel so that the total quantum number $S = \sum_{i=1}^{5} s_i = 5/2$ and the total angular momentum $L = 0$.

In the crystal lattice an interaction between the Mn^{2+} ions is intermediated by the crystal anions Te^{2-}. Resulting from this, different types of exchange processes appear, like the nearest-neighbor and the five times smaller next-nearest-neighbor exchange process (described by the exchange integrals J and J_{NNN}, respectively), which both carry an antiferromagnetic character. They are based on three different contributions, the two-hole-, the one-hole-one-electron and the two-electron process. The first one plays the major role and

is named *super exchange* mechanism. It is an indirect exchange interaction due to the anions, which involves the valence band. The minor contributions are the one-hole-one-electron-process, which accounts only 5% to the exchange interaction, and the two-electron process, which is negligible [40].

If the concentration x of Manganese is low, like in the *dilute limit* ($x < 0.01$), the Mn^{2+} spins can be regarded as isolated and their interaction is vanishingly small. In this case and for high temperatures the system is described in the *paramagnetic phase*. In the dilute limit the magnetization $\boldsymbol{M}$ is described by the Brillouin function

$$\boldsymbol{M} = -x\, N_0\, \mathrm{g_{Mn}}\, \mu_B\, \langle S_z \rangle = x\, N_0\, \mathrm{g_{Mn}}\, \mu_B\, S\, \boldsymbol{B}_S\left(\frac{\mathrm{g_{Mn}}\, \mu_B\, S\, \boldsymbol{B}}{k_B\, T}\right), \tag{16}$$

where N_0 is the number of Mn^{+2} ions per unit volume, $\mathrm{g_{Mn}}$ the Manganese g-factor, k_B is the Boltzmann constant, μ_B the Bohr magneton and $\langle S_z \rangle$ the average spin per Mn site. $\boldsymbol{B}_S$ is the Brillouin function of the spin $S = 5/2$ resulting for the Mn^{2+} d-shell and $\boldsymbol{B}$ the applied magnetic field.

For low magnetic fields or high temperatures, where the argument of the Brillouin function $g\mu_B S\boldsymbol{B}/k_B T << 1$, the magnetization $\boldsymbol{M}$ is linear in $\boldsymbol{B}$ and reduces to

$$\boldsymbol{M} = \chi_{Mn}\boldsymbol{B}, \tag{17}$$

$$\chi_{Mn} = \frac{C_0\, x}{T} = \frac{N_0\, x\, (\mathrm{g}_{Mn}\, \mu_B)^2\, S\, (S+1)}{3\, k_B T}, \tag{18}$$

with the static magnetic susceptibility χ_{Mn} in the Curie form.

The description of the magnetization $\boldsymbol{M}$ for high temperatures and arbitrary x cannot be expressed by the standard Brillouin function, because the Mn-Mn interaction has to be taken into account. A more general formulation for $\boldsymbol{M}$ results by exchanging the magnetic ion mole fraction x and temperature T in Eq. (16) with the phenomenological fitting parameters x_{eff} and T_{eff}, given by

$$\boldsymbol{M} = x_{eff}\, N_0\, \mathrm{g_{Mn}}\, \mu_B\, S\, \boldsymbol{B}_S\left(\frac{\mathrm{g}\, \mu_B\, S\, \boldsymbol{B}}{k_B\, T_{eff}}\right). \tag{19}$$

In Eq. (19) $x_{eff} < x$ corresponds to the effective average concentration of Mn and $T_{eff} = T_{\mathrm{Mn}} + T_0$ accounts the antiferromagnetic interactions [42]. Here T_0

represents the temperature of the lattice and T_{Mn} the Mn temperature. For magnetic fields up to 5 T and temperatures between 1.5 K and 20 K, x_{eff} is nearly equal to the number of "free Mn spins", which corresponds to the effective amount of Mn atoms excluding the nearest neighbor interaction [4].

An important consequence arises from the exchange interaction between the $3d^5$ electrons of Manganese and the s or p band electrons of $Cd_{1-x}Mn_xTe$. This is known as the $sp-d$ exchange interaction and affects different phenomena, which involve electrons in the conduction and valence bands, exciton levels and impurities, because they are based on the same effects resulting from an Mn modified band structure. This influence is accounted by adding a Kondo-like exchange term $\hat{H}_{ex}^{sp-d}$ to the original Hamiltonian $\hat{H}_0$, given by

$$\hat{H} = \hat{H}_0 + \hat{H}_{ex}^{sp-d} = \hat{H}_0 + \sum_{\boldsymbol{R}_i} J^{sp-d}\left(\boldsymbol{r} - \boldsymbol{R}_i\right) \boldsymbol{S}_i \cdot \boldsymbol{\sigma}, \tag{20}$$

where J^{sp-d} is the electron-ion $sp-d$ exchange coupling constant, $\boldsymbol{S}_i$ and $\boldsymbol{\sigma}$ are the spin operators for the Mn^{2+} and the band electrons with the corresponding coordinates $\boldsymbol{R}_i$ and $\boldsymbol{r}$, respectively.

Equation (20) can be solved theoretically and allows to calculate the exchange integral α for s-like Γ_6 electrons and β for p-like Γ_8 electrons. Experimentally the corresponding values of the $sp-d$ exchange constants $N_0\alpha$ and $N_0\beta$, which are specific for different materials, are obtained in magneto-optical or quantum transport measurements. While α and β are nearly independent on the Mn concentration x, they are of opposite sign ($\alpha > 0$ and $\beta < 0$) and $|\alpha| < |\beta|$. For example, in $Cd_{1-x}Mn_xTe$ the exchange constants are $N_0\alpha = 0.22$ eV and $N_0\beta = -0.88$ eV. Both exchange interactions underlie obviously an interplay of two fundamental physical origins. The first one is a $1/r$ potential exchange interaction between the d electrons of Manganese and the s or p type band electrons, through which the spin of the electrons is aligned parallel to the Mn^{2+} ions. This corresponds to a ferromagnetic interaction, adding a positive contribution to the exchange constant. The second one is due to the hybridization of the $3d^5$ levels with the p band electrons (interaction with s band electrons is forbidden by symmetry) leading to a very strong antiferromagnetic interaction and thus to a negative contribution. While the exchange constant α for s-like electrons stems from the positive $s-d$ potential interaction only, β

arises from both the positive $p-d$ potential and the much stronger negative $p-d$ hybridization interaction [40]. In n-type DMS samples like Iodine doped $Cd_{1-x}Mn_xTe$, the exchange constant is determined by α, whereas it is governed by β for p-type materials, like $Ga_{1-x}Mn_xAs$ or $In_{1-x}Mn_xAs$, in which Manganese itself is the acceptor, leading to a p-doped semiconductor.

2.6 THz radiation induced photocurrents

In this work mainly the magnetic field induced photogalvanic effect is investigated, but however, in most of the investigated samples photocurrents are allowed even in the absence of an external magnetic field. Due to their strength and polarization dependence they allow to extract important information about the electron gas heating. The considered effects are based on THz radiation incident on a doped semiconductor. Such kind of photocurrents are allowed for oblique or normal incident radiation, dependent on the samples symmetry and growth direction. Due to the fact that these currents are independent on the magnetic field $\boldsymbol{B}$, a switching of the direction of $\boldsymbol{B}$ does not yield a change of sign. Thus, these contributions can be excluded from the previously discussed MPGE. Since experimental data to photocurrents in response to linear or circular polarized radiation are shown in this work, the corresponding phenomenological equations are presented in this section.

The phenomenological equation describing the current induced by THz light is given by

$$j_\lambda = \sum_{\lambda\mu\nu} \chi_{\lambda\mu\nu} I e_\mu e_\nu^* + \sum_{\delta\mu\nu} T_{\lambda\delta\mu\nu} q_\delta I e_\mu e_\nu^*, \tag{21}$$

with the complex conjugated $e_\nu^* = e_\nu^*(\omega) = e_\nu(-\omega)$ of e_ν. In general the complex amplitude of the electric field $\boldsymbol{E}$ is written in the form $\boldsymbol{E} = E\boldsymbol{e}$ with its real amplitude E and the complex unity vector of the polarization $\boldsymbol{e}$ with $|\boldsymbol{e}|^2 = 1$ and $E^2 = I$. The first part of the right hand side of Eq. (21) represents the photogalvanic effects and is described by the third rank tensor $\chi_{\lambda\mu\nu}$ [3,43]. In contrast, the second term is determined by a fourth rank tensor $T_{\lambda\delta\mu\nu}$ and contains the wave vector $\boldsymbol{q}$, which constitutes the photon drag effect.

The term $e_\mu e_\nu^*$ in Eq. (21) can be simplified by decomposing it into a symmetric and asymmetric product given by

$$e_\mu e_\nu^* = \{e_\mu e_\nu^*\} \ + [e_\mu e_\nu^*] \ , \tag{22}$$

$$\{e_\mu e_\nu^*\} = \tfrac{1}{2}(e_\mu e_\nu^* + e_\nu e_\mu^*) \text{ and } \ [e_\mu e_\nu^*] = \tfrac{1}{2}(e_\mu e_\nu^* - e_\nu e_\mu^*). \tag{23}$$

In a similar way, $\chi_{\lambda\mu\nu}$ can be separated into a product of two tensors. While its real part is symmetric in the last two indices with $\chi_{\lambda\mu\nu} = \chi_{\lambda\nu\mu}$, its asymmetric contribution, equal to the imaginary part, can be replaced by the second rank pseudo tensor $\gamma_{\lambda\rho}$ and the totally asymmetric Levi-Civita tensor $\delta_{\rho\mu\nu}$. The asymmetric part of the product $\chi_{\lambda\mu\nu} e_\mu e_\nu^*$ reduces to

$$\chi_{\lambda\mu\nu}\,[e_\mu e_\nu^*] \ = \ i \sum_\rho \gamma_{\lambda\rho}\delta_{\rho\mu\nu}\,[e_\mu e_\nu^*] \ = \ \gamma_{\lambda\rho} i(\boldsymbol{e} \times \boldsymbol{e}^*)_\rho. \tag{24}$$

Including this simplifications, Eq. (21) can be written in the form

$$j_\lambda = \sum_{\lambda\mu\nu} \chi_{\lambda\mu\nu} I\,\{e_\mu e_\nu^*\} + \sum_\rho \gamma_{\lambda\rho} I i(\boldsymbol{e} \times \boldsymbol{e}^*)_\rho + \ \sum_{\delta\mu\nu} T_{\lambda\delta\mu\nu} I q_\delta e_\mu e_\nu^*. \tag{25}$$

The three terms on the right hand side of Eq. (25) represent the linear and circular photogalvanic effect as well as the photon drag effect, respectively. While the first and the last term are allowed in systems lacking a center of inversion, the circular photogalvanic effect requires additionally gyrotropy. These effects are described under the assumption of homogeneous samples and spatially homogeneous optical excitation [3, 43].

3 Experimental methods and techniques

This chapter is dedicated to the description of the experimental setup and techniques used in this work. It includes pulsed and continuous wave (*cw*) THz laser sources as well as optical elements to vary the polarization state of the radiation. Furthermore, details of the samples, like the material systems, physical properties and geometries are shown. In addition to the photocurrent measurements photoluminescence (PL) and time resolved Kerr rotation (TRKR) were investigated. These techniques are explained shortly at the end of this chapter.

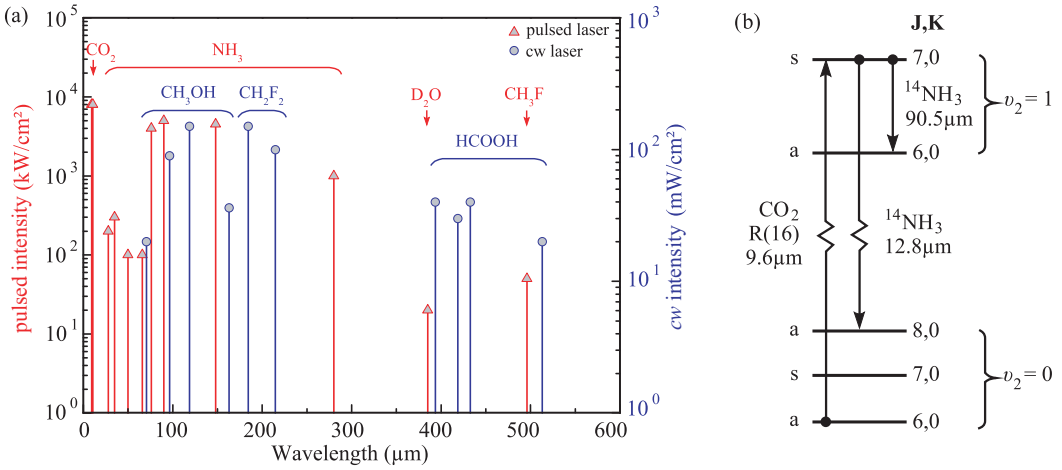

Figure 5: (a) Laser lines in the THz range due to optical pumping of a molecular laser by a pulsed laser (red triangles) and a *cw* laser (blue circles). (b) Excitation process of NH_3 by CO_2 radiation.

3.1 Generation of THz radiation

In order to generate photocurrents in the samples THz radiation was applied, aimed to induce Drude absorption. This radiation can be produced using different devices and techniques, like the *p*-Ge laser [44], free electron laser [45], quantum cascade lasers [46], THz time-domain spectroscopy systems (for review see [47]) and many other. The laser systems, which were chosen for the experiments are THz molecular gas laser optically pumped with a CO_2 laser.

They allow to produce radiation in wide range of power and frequency, can operate in the *cw* or pulsed mode and are robust systems, which operate at room temperature.

3.1.1 Optically pumped molecular THz laser

An effective way to create intensive THz laser radiation is to use molecular gases as active media, which are pumped optically by a pulsed or *cw* CO_2 laser. For example one can use NH_3, D_2O, CH_3F, CH_3OH and many more. As this type of laser is currently not so widely used, the physics and characteristics describing these monochromatic and powerful radiation sources will be briefly introduced. The lasing for the most wavelengths is based on stimulated Raman scattering and therefore, these sources can be classified as Raman laser. Here, a permanent electric dipole moment of the molecule is necessary in order to transform the Mid-InfraRed (MIR) CO_2 radiation into the THz region [48]. The optical pumping with MIR radiation results in an excitation of vibrational-rotational transitions, which relax due to rotational transitions shown in Fig. 5(b). The wavelength of the light depends on the one hand on the pump energy and on the other on the laser gas. Therefore, the whole THz range is covered with discrete laser lines by using this technique. For the experiments only several strong lines, shown in Fig. 5(a), are used.

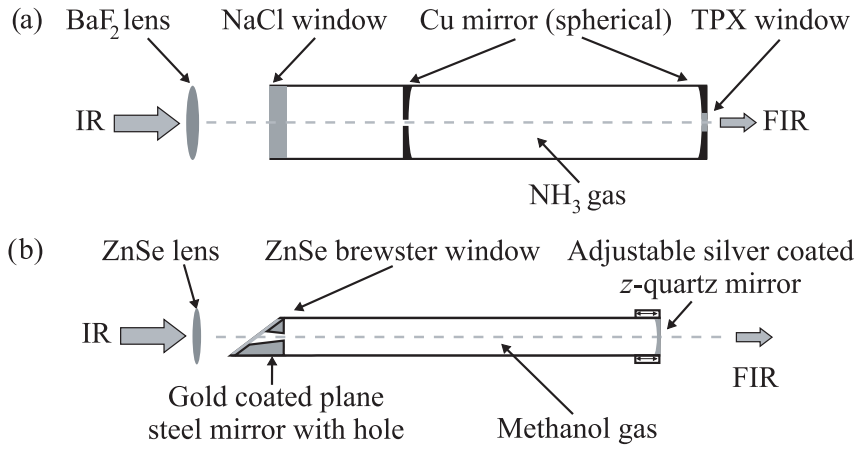

Figure 6: THz laser resonator for (a) pulsed and (b) *cw* radiation.

3.1.1.1 Pulsed THz radiation: The pulsed CO_2 radiation was focused using a BaF_2 lens through a NaCl window into a glass cylinder filled with NH_3 gas. Two gold coated spherical mirrors aligned to the optical axis of the resonator allow a reflection of the exciting beam to obtain a maximal absorption. While the decoupling TPX (4-Methylpenthen-1) window is transparent for the emitted THz radiation, the IR radiation from the CO_2 laser is absorbed completely, see Fig. 6(a). The emitted THz pulse has a length of $t_p \approx 100$ ns and a maximum peak power P_p of several kW, dependent on the laser gas.

3.1.1.2 cw THz radiation: In the case of the *cw* THz laser a ZnSe lens is used to focus the CO_2 radiation, through a ZnSe Brewster window and the cone of a gold coated plane steel mirror, into the resonator, see Fig. 6(b). Inside this tube methanol gas is provided as active media. By changing the position of the adjustable silver coated dielectric z-cut quartz mirror the wavelength and mode structure can be set. This mirror acts due to a uncoated annulus as a transmission window for the produced THz radiation. The IR radiation is reflected due to the mirrors dielectric properties [49].

3.1.2 Calibration of the laser system

It is of particular interest for the experiment to know for every pulse or period of time the exact power, which acts on the sample. To include the variation of intensity a beam splitter (mylar film) was inserted in the optical path, reflecting a small part of the beam to a reference detector. The ratio between the reflected and transmitted part of the radiation is wavelength dependent, which is characteristic for the beam splitter material. Furthermore, each optical device, like $\lambda/4$-, $\lambda/2$-plates, grids, filters or absorbers, has a characteristic spectral absorption and reflection, which has to be taken into account. The corresponding spectra were obtained using a Fourier Transform InfraRed (FTIR) spectrometer. In order to calibrate the system, shown in Fig. 7, a second detector or powermeter is placed at the sample spot and allows to determine the ratio between both radiation paths.

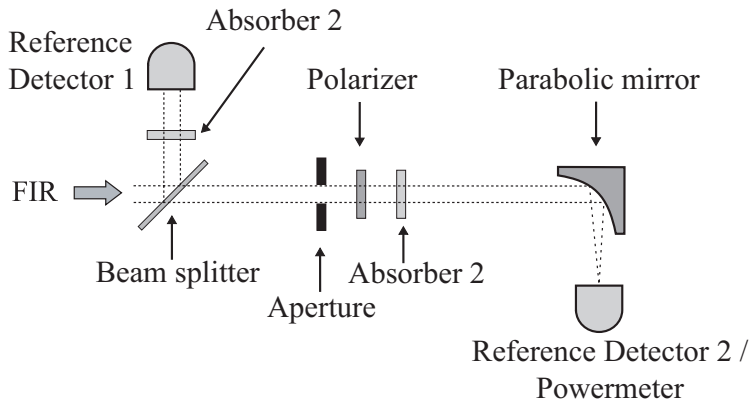

Figure 7: Calibration of the THz laser system including several optical devices.

3.2 Variation of the light's polarization state

The photocurrents investigated in this work are strongly influenced by the radiation polarization. In fact, it will be demonstrated below that the various contributions to the current can be described in simple terms of the four Stokes parameters: s_0 characterizes the intensity of the radiation, s_1 and s_2 the degree of linear polarization and s_3 the degree of circular polarization. The linear polarization emitted from the THz lasers is changed utilizing birefringent medias. While such elements are standard devices in the IR and visible region, they are commercially unavailable for THz radiation and had to be produced by ourself. As a suitable media we chose x-cut quartz. This material has two different refraction indices n_o and n_eo for the in plane ordinary and extraordinary axis, respectively [43, 50, 51]. The difference of the refraction indices $\Delta n = n_\mathrm{o} - n_\mathrm{eo}$ in the THz range was obtained applying a FTIR spectrometer, using parallel and crossed polarizers. Thus, we obtained $\Delta n(\lambda)$, allowing us to calculate and fabricate $\lambda/2$- and $\lambda/4$-plates, specially for each wavelength.

The electric field vector $\boldsymbol{E}$ of linear polarized light incident normal to the optical axis c, defined as the slow axis (higher refraction index), can be decomposed into to two parts $\boldsymbol{E}_{||}$ and $\boldsymbol{E}_{\perp}$ (parallel and perpendicular to the main symmetry axis). Hence, a phase shift $\Delta\phi$, dependent on the plates thickness d, its

orientation in respect to the optical axis and the wavelength λ, arises due to two different propagation velocities for both beams inside the media, given by

$$\Delta\phi = k_o d - k_{eo} d = \frac{2\pi d}{\lambda}\Delta n. \tag{26}$$

Equation (26) is used to calculate the thickness d necessary to obtain plates, which allows us vary the light's polarization state. Thus, two important cases should be distinguished in the following. In the experiment $\lambda/2$-plates were used to rotate the plane of linear polarization and $\lambda/4$-plates to obtain circularly (elliptically) polarized radiation.

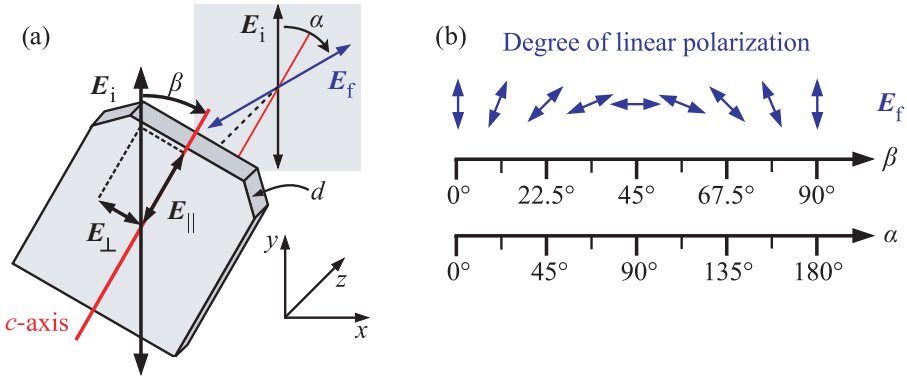

Figure 8: (a) Sketch of $\lambda/2$ plate with initial and final polarization of radiation, (b) degree of linear polarization.

The variation of the linear polarization is described by the two Stokes parameters s_1 and s_2. In the case of a $\lambda/2$-plate the phase shift $\Delta\phi$ has to be an odd multiple of 180°, or in detail $\Delta\phi = (2n+1)\pi$, where n is numbering the order. Then the linear polarization $\boldsymbol{E}_f$ is rotated in respect to the initial $\boldsymbol{E}_i$ around the azimuth angle α which is equal to the double rotation angle β, see Figs. 8(a) and (b). Higher orders of $\lambda/2$-plates, described by $n = 1, 2, ...$, are possible as well, but result in thicker plates emerging a stronger absorption of radiation. In a coordinate system where z is the propagation direction (parallel to the rotary axis of the $\lambda/2$-plate), $x \,||\, \boldsymbol{E}_i$ and y are detection plane axes, the

rotation of the linear polarized light $\boldsymbol{E}_f$ can be described by its two components E_x and E_y according to the three Stokes parameters, given by [52, 53]

$$s_0 = |E|^2 = I, \tag{27}$$

$$\frac{s_1}{s_0} = \frac{(|E_x|^2 - |E_y|^2)}{|E|^2} = \cos(2\alpha), \tag{28}$$

$$\frac{s_2}{s_0} = \frac{(E_x E_y^* + E_y E_x^*)}{|E|^2} = \sin(2\alpha). \tag{29}$$

The $\lambda/4$-plate gives an access to the fourth Stokes parameter s_3, describing

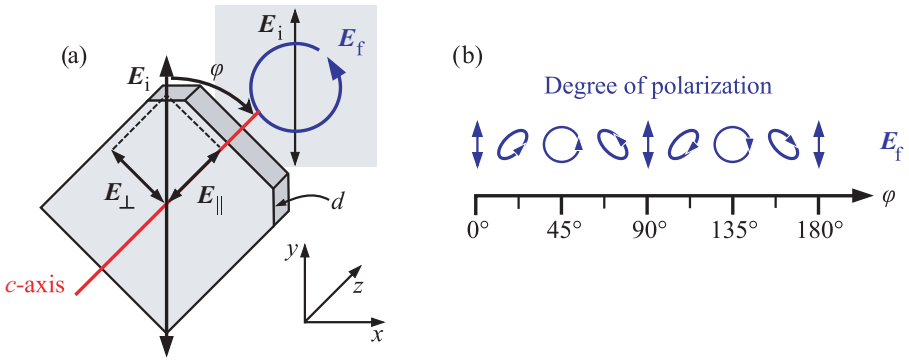

Figure 9: (a) Sketch of $\lambda/4$-plate with initial and final polarization states of the radiation, (b) degree of polarization.

the circular polarization of the radiation. In contrast to the $\lambda/2$-plate, the $\lambda/4$-plates thickness d is chosen to result in a phase shift $\Delta\phi = 90° = (2n + \frac{1}{2})\pi$. If φ is the angle which describes the rotation of the c-axis in respect to the initial polarization E_i, exactly at $\varphi = 45° + n \cdot 180°$ and $\varphi = 135° + n \cdot 180°$ fully right and left circular polarized light results, respectively, see Figs. 9(a) and (b). For the case, that the initial polarization is parallel either to the ordinary or to the extraordinary refraction index at $\varphi = n \cdot 90°$ the light passes through the plate without being influenced, so that $\boldsymbol{E}_i = \boldsymbol{E}_f$. In between these positions the polarization state is elliptically, giving rise to a part of the radiation which is polarized perpendicular to $\boldsymbol{E}_i$ with its maximum at $\varphi = 22.5° + n \cdot 90°$.

The dependence on the rotation of the $\lambda/4$-plate is described by the Stokes parameters s_0, s_1, s_2 and s_3 given by [52, 53]

$$s_0 = |E|^2, \tag{30}$$

$$\frac{s_1}{s_0} = \frac{(|E_x|^2 - |E_y|^2)}{|E|^2} = \frac{1+\cos(4\varphi)}{2}, \tag{31}$$

$$\frac{s_2}{s_0} = \frac{(E_x E_y^* + E_y E_x^*)}{|E|^2} = \frac{\sin(4\varphi)}{2}, \tag{32}$$

$$\frac{s_3}{s_0} = \frac{i(E_x E_y^* - E_y E_x^*)}{|E|^2} = P_{\text{circ}} = \sin(2\varphi). \tag{33}$$

3.3 Experimental setup

The components of the experimental setup communicate via GPIB (General Purpose Interface Bus) or the parallel printer port and are controlled via a software written in Labview . For example, it allows to actuate the magnetic field, as well as driving a step motor rotating λ/4-, λ/2-plates or grid polarizers. Furthermore, a continuously recording of data, with temporal defined steps or a feedback from the operator is possible. All parameters, like the magnetic field strength, angle of rotation, temperature, reference and sample signals are transmitted from each device to the measurement PC and stored in a file.

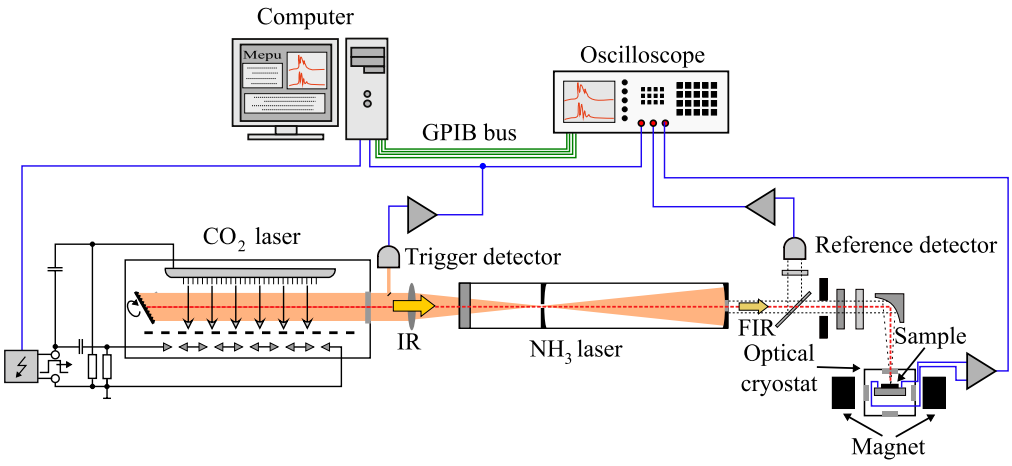

Figure 10: Experimental setup of the optically pumped pulsed THz laser.

In the case of the pulsed laser system, shown in Fig. 10, the signals are amplified and then digitalized by a digital storage oscilloscope. The pulse length t_p is in the order of 100 ns and corresponds to a frequency of 10 MHz. To resolute the temporal shape of this signal, high frequency electronics up to 300 MHz is required. In contrast to the pulsed system the laser radiation in the *cw* system, shown in Fig. 11, had to be chopped optically and therefore, operates at much lower frequencies in the region between 0.1 kHz and 1 kHz. Due to the fact that the intensity of the *cw* THz laser is by a factor of 10^6 lower compared to the one emitted from the pulsed system, low noise pre-amplifiers in combination with lock-in technique had to be utilized to decrease the influence of surrounding electrically noise. For an additional improvement of the signal processing, both the reference and sample beam were chopped at different frequencies.

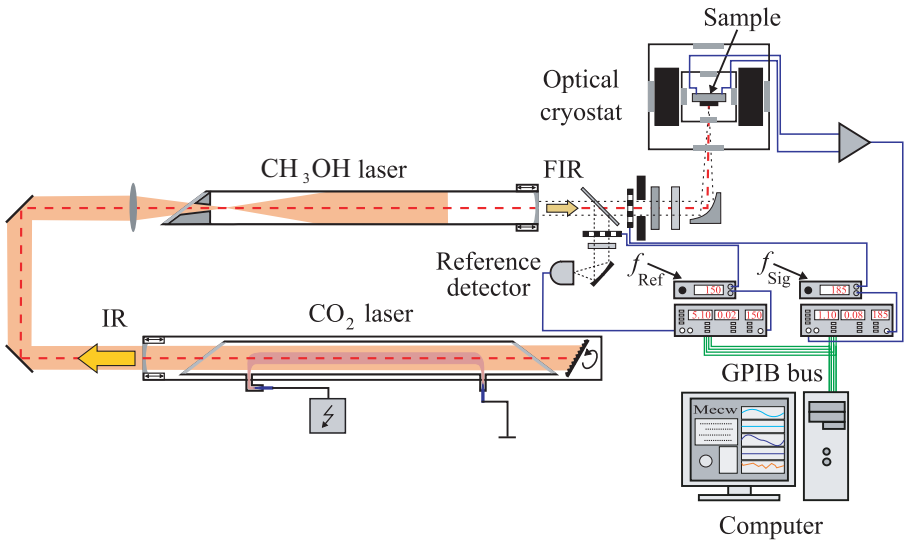

Figure 11: Experimental setup of the optically pumped *cw* THz laser.

For the magnetic field dependent experiments two different types of magnets were used. A water cooled magnet, which can reach up to $\boldsymbol{B} \leq |0.6|$ T without concentrators ($\boldsymbol{B} \leq |1.0|$ T with concentrators) and a superconductive one, which is placed in a liquid helium bath inside a Oxford Spectromag Cryostat ($\boldsymbol{B} \leq |7.0|$ T).

Due to the lack of special devices in the THz range the wavelength of the THz sources were measured applying a home-made Michelson interferometer, shown

in Fig. 12(a). Another important tool to probe the quality, mode structure as well as the minimum focus area of the THz beam is a pyroelectric camera. This device allows to image the intensity distribution in a detection square of one half inch (12.8 mm) side length with 128 rows of 128 small pyroelectric sensors [a corresponding image is shown in Fig. 12(b)]. It has a resolution of 0.1 mm and is applicable in a wide spectral region, for microwave up to ultra-violet (UV) radiation.

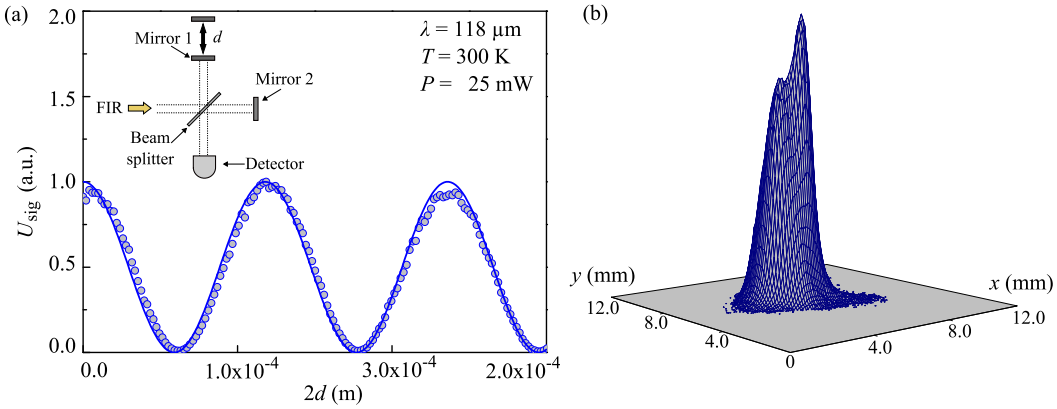

Figure 12: (a) Measurement of wavelength using a Michelson interferometer, as shown in the inset. (b) 3D image of a THz pulse recorded at $\lambda = 118$ µm with a pyroelectric camera.

3.4 Samples description

All samples investigated in this work were grown by molecular-beam epitaxy (MBE). They differ in growth direction, along [110]- or [001]-axis, and their material compositions, GaAs/$Al_xGa_{1-x}As$ or $Cd_yMg_{1-y}Te/Cd_xMn_{1-x}Te$. The samples were square shaped with a side length of 5 mm and the edges were oriented along the crystallographic directions. For the photocurrent measurements ohmic contacts were alloyed on the four corners and the four centers of the edges using Indium.

3.4.1 (110)-grown GaAs samples

As discussed in the previous chapter, the first measurements on the zero-bias spin separation were carried out on (001)-grown GaAs samples. The application of samples with another growth direction, due to symmetry arguments addressed in Section 4.1.2, substantially changes the current behavior as well as spin relaxation processes. An important example is given by (110)-grown n-type GaAs/$Al_{0.3}Ga_{0.7}As$ heterostructures.

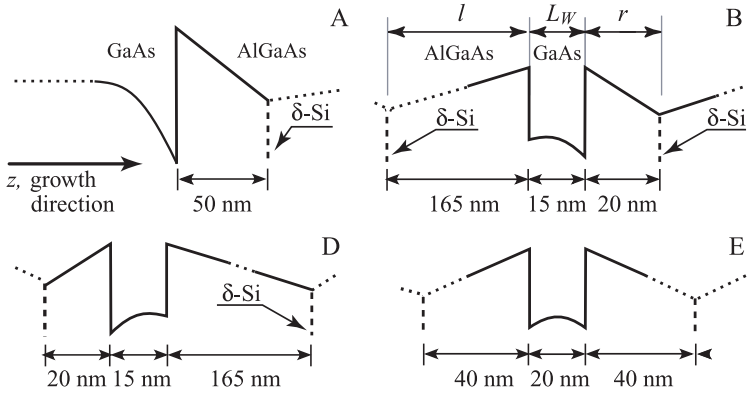

Figure 13: Band profiles of QWs and doping positions for the (110)-grown samples A, B, D and E.

The investigated samples were Si-δ-doped emerging a mobility μ and carrier density n_s measured in the dark at 4.2 K between $0.8 \cdot 10^5$ and $2.2 \cdot 10^5$ cm^2/Vs and between $1.5 \cdot 10^{11}$ cm^{-2} and $4.0 \cdot 10^{12}$ cm^{-2}, respectively [19, 31]. Their corresponding conduction-band profiles resulting from the varied δ-doping positions in respect to the QW widths L_W are shown in Fig. 13. The edges of the samples were oriented along the crystallographic directions $x \parallel [1\bar{1}0]$ and $y \parallel [00\bar{1}]$. An essential difference in the investigated structures is hidden in their doping profile, which strongly affects the symmetry. The heterojunction, indicated as sample A, shows the most significant and strongest asymmetric band structure stemming from the triangular confinement potential. In samples B and D, the doping layers are asymmetrically shifted off the QW center either to the left or to the right, respectively. This yields an asymmetric potential profile inside the QWs (see Fig. 13). To observe a higher response the QW sequence was repeated ten times with a periodicity of 200 nm, so that the

right side doping of the first QW is the left side doping of the second one. In contrast, sample E was grown fully symmetric containing Si-δ-sheets, placed in the center of each barrier between adjacent QWs [19].

3.4.2 (001)-grown DMS samples

The influence of the variation of the g^*-factor on the MPGE, providing an important access to its microscopic origin, was investigated by means of diluted magnetic semiconductors. In these samples the implanted magnetic ions emerge a strong modification of g^*, dependent on different parameters, like the temperature and Mn concentration. The DMS samples are single QW structures grown by MBE on (001)-oriented GaAs substrates with evenly spaced $Cd_{1-x}Mn_xTe$ thin layers [20]. This magnetic insertions were introduced during the growth of the 10 nm wide QW [Fig. 14(a)] applying digital alloy technique [54–57]. The DMS samples differ mainly in their manganese concentration x and the way it is embedded in the QW. DMS sample A contains two layers of three-monolayer-thick $Cd_{0.8}Mn_{0.2}Te$, whereas DMS sample B contains three single monolayers of $Cd_{0.86}Mn_{0.14}Te$. As a reference, DMS sample C was grown without Mn inserted in the QW. For a free carrier concentration all samples were modulation doped with Iodine donors in the top layer at a 15 nm distance from the QW. Table 1 shows the corresponding values for n_e and μ. The sample edges were oriented along $x \parallel [1\bar{1}0]$ and $y \parallel [110]$ directions.

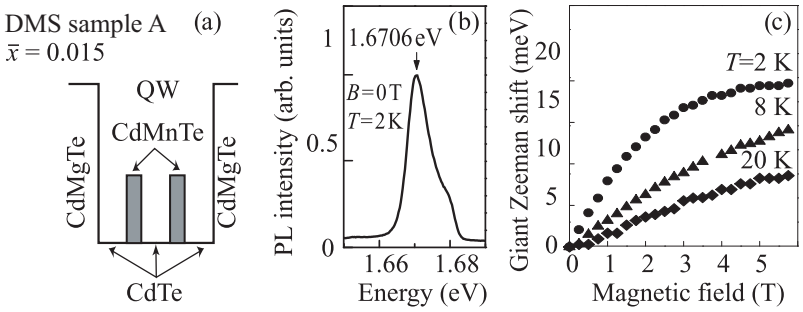

Figure 14: DMS sample A: (a) Sketch of the structure. (b) Photoluminescence spectrum at $B = 0$T. (c) Shift of the PL line corresponding to one half of the total giant Zeeman splitting.

Further necessary data were obtained applying photoluminescence measurements. A typical PL spectrum of DMS sample A without an applied magnetic field is shown in Fig. 14(b). The linewidth of this peak is about 11 meV and corresponds to the Fermi energy ε_F [58]. A spectral shift of the line to lower energies is observed if an external magnetic field $\boldsymbol{B}$ is applied. This reflects the giant Zeeman splitting of the band [40]. In Fig. 14(c) the relative shift of the peak maximum is plotted in respect to the strength of the applied magnetic field. The data show a strong temperature dependence and are about 2.5 times larger than the giant Zeeman splitting of the conduction band states. In Table 1 the sample parameters $\bar{x}$ and ϵ_F, extracted from the PL measurements, are summarized.

DMS sample	x	$\bar{x}$	μ, cm^2/Vs	n_e, cm^{-2}	ε_F, meV
A	0.20	0.015	9500	$4.7 \cdot 10^{11}$	11.7
B	0.14	0.013	16000	$6.2 \cdot 10^{11}$	15.4
C	0	0	59000	$4.2 \cdot 10^{11}$	10.4

Table 1: DMS sample parameters, including the effective average concentration of Mn $\bar{x}$, estimated from the giant Zeeman shift of the interband emission line [Fig. 14(c)], mobility μ and electron sheet density n_e, obtained at 4.2 K in the dark.

3.4.3 (001)-grown GaAs samples with lateral structures

The photogalvanic effects strongly depend on the symmetry of the investigated samples and therefore usually are affected by e.g. the growth direction, doping profile, gate voltage or the crystal structure. However, as we demonstrate here it can be also controllable varied by a specially designed lateral structure [59, 60]. The photocurrents are studied in (001)-GaAs/$Al_{0.3}Ga_{0.7}As$ MBE grown n-type single modulation-doped quantum well (QW) structures of 30 nm width with a superimposed lateral grating on the top cap. At a temperature $T = 4.2$ K (300 K) the superlattice (SL) samples exhibit a mobility $\mu \approx 5 \cdot 10^6$ cm^2/Vs ($\approx 6 \cdot 10^3$ cm^2/Vs) at a carrier density $n_e \approx 2 \cdot 10^{11}$ cm^{-2} ($\approx 1.2 \cdot 10^{11}$ cm^{-2}). Electron beam lithography was used to transfer slits into a photoresist on top of the samples. The properties of the used technique allowed

to write an area of $150 \cdot 150\,\mu m^2$ in size. Therefore this step was repeated 64 times to obtain a large patterned area. After subsequent reactive ion etching process, using $SiCl_4$, the 0.5 µm wide one-dimensional grooves in a distance of 2.5 µm were produced, as shown in the corresponding electron micrograph in Fig. 15(a). In this process care was taken not to etch through the QW. The gratings are oriented either along $\langle 010 \rangle$ (SL sample 1) or close to $\langle 110 \rangle$ (SL samples 2, 3) crystallographic directions. In the SL samples 2 and 3 the electron micrograph shows that the grooves cross section are almost symmetric, whereas the profile of SL sample 1 is asymmetric, shown in Fig. 37(b). This different depth in both sides of the grooves is a result of the anisotropic etching properties along [110] and $[1\bar{1}0]$ directions [61]. In addition to the structured samples an unpatterned reference sample 4 was prepared. The effects of an external in-plane magnetic field were studied in a sample with a different type of lateral potential. The superlattice in SL sample 5 consists of a asymmetric sequence of slits with different thickness, accordingly $(4-3-2)$ µm with 3 µm thick spacer separating the grooves, shown in Fig. 15(b). This was repeated periodically and results in an asymmetric lateral potential, which allows to be controllable produced. The slits were oriented along one of the crystallographic axis <110>. At room temperature the sample exhibits a mobility $\mu \approx 4.3 \cdot 10^3\,cm^2/Vs$ at a carrier density $n_e \approx 1.8 \cdot 10^{11}\,cm^{-2}$.

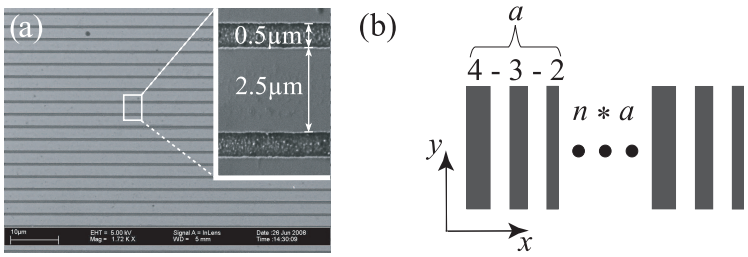

Figure 15: (a) REM picture of a etched surface structure (SL samples 2) with equal distances between the grooves. (b) Sketch of SL sample 5 with $(4-3-2)$µm grooves (dark lines) with 3µm thick spacer separating.

3.5 Photoluminescence and Kerr rotation

The time-resolved photoluminescence (TRPL) measurements, applied to study the photocarrier dynamics were carried out in cooperation with the group of Prof. Schüller from the University of Regensburg and is addressed here only briefly. The samples were excited nonresonantly above the Fermi energy, utilizing a Ti-Sapphire laser system with a excitation density of about 130 W/cm^2. The samples were placed in a He flow cold finger cryostat with optical windows, allowing a controllable sample temperature in the range between 4 K and room temperature. The pump beam is circularly polarized after passing a $\lambda/4$-plate and excites electron-hole pairs within the QWs, which are then spin-polarized due to optical selection rules, see Fig. 16(a). After collecting the emitted photoluminescence radiation via an achromat and focusing it onto a Hamamatsu streak camera system, which is synchronized to the Ti-Sapphire laser, an ultrafast temporal measurement of the light intensity is possible. The time-resolved spectra are averaged over a spectral window of 40 meV in order to evaluate the time-resolved PL data. This range was centered around the maximum of the PL emission from the QWs and shifted in the temperature-dependent measurements accordingly to lower energies as the PL energy decreases. For exciting and probing a Ti-Sapphire laser system, with a pulse length of 600 fs, is used. By analyzing the maximum and the half-width of the PL spectra the bandgap and the Fermi energy of the n-doped QWs are extracted. To record

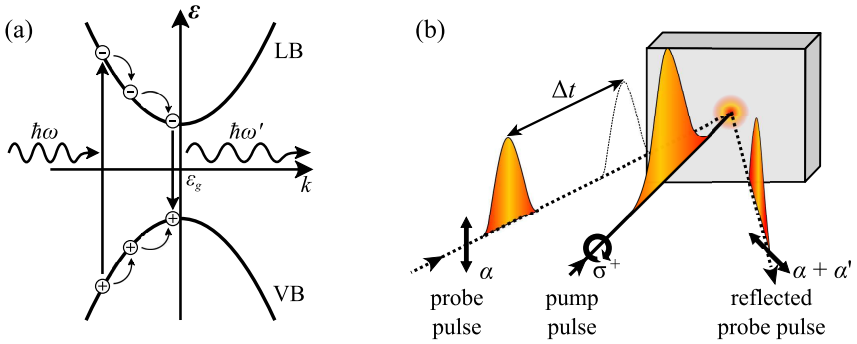

Figure 16: (a) Photoluminescence due to recombination of excited electron hole pairs under emission of light $\hbar\omega' < \hbar\omega$. (b) schematic illustration of the time resolved Kerr rotation.

the nonequilibrium spin polarization within the sample the magneto-optic Kerr effect was exploited using a weaker and linearly polarized time-delayed probe pulse. This method allows to extract spin relaxation times of the conduction band electrons. In the presence of a spin polarization normal to the sample plane, the linear polarization of the pump pulse, which is reflected on the surface of the sample is tilted by a small angle α', being proportional to the spin polarization. The ideal central wavelength of the laser for the further experiments is tuned above the PL maximum to excite electrons slightly above the Fermi energy. Due to the fact that the temperature influences the onset of the absorption, the laser wavelength has to be adjusted for temperature dependent measurements accordingly. A beam splitter separates the laser pulse train into two parts: a probe and a pump beam. The linearly polarized probe pulse train is delayed with respect to the pump beam via a mechanical delay line. Both beams are focused onto the sample surface at near-normal incidence with an achromat, resulting in a laser spot size of about 80 µm. The reflected probe beam is tilted with respect to its initial linear polarization of the probe beam due to Kerr rotation. This small rotation is analyzed using an optical bridge detector and measured as a function of the delay between the pump and probe pulses, see Fig. 16(b).

4 BIA/SIA in (110)-grown Heterostructures

The presence of the MPGE, which is described in terms of the zero-bias spin separation, was demonstrated in (001)-grown GaAs QW structures showing that the measured effect is well described by the phenomenological equations (6)-(7) and may be used as a tool to study BIA and SIA [30]. In this work, the magnetic field dependent effect was observed for the first time in (110)-grown GaAs/AlGaAs heterostructures and a method was developed to measure the degree of the sample's structural asymmetry [19,31]. In contrast to (001)-grown samples these type of structures are of particular interest, because they emerge a circular and linear photogalvanic current even at zero magnetic field and normal incidence of radiation. Both effects result from the bulk inversion asymmetry, which induces an effective magnetic field pointing along the growth direction, while the structure inversion asymmetry yields an in-plane effective magnetic field, similar to (001)-grown structures. The MPGE is a versatile tool to investigate BIA and SIA and yields a photocurrent dependent on the polarization state of the radiation, the orientation of the magnetic field and the temperature. The obtained experimental results are supported by the theory of the MPGE in (110)-grown heterostructures, which was developed in parallel to the experimental work. Furthermore, the data show that the structure inversion asymmetry can be controlled and tuned to zero by shifting the position of the δ-doping layer. While the photocurrent in the presence of an in-plane field is observed in asymmetric structures, it vanishes in symmetrically doped QWs. Additional time-resolved Kerr rotation measurements confirm the MPGE data, showing that in symmetrically doped QWs the spin relaxation time is maximal. Obtaining such symmetric (110)-grown GaAs/AlGaAs QW structures is of particular interest for spintronic devices, because they offer a opportunity to vary the spin dephasing for instance by the application of an external gate voltage.

4.1 Influence of BIA/SIA on the MPGE

4.1.1 Photocurrent Experiments

In the experiment the MPGE is induced applying THz radiation. This leads to indirect intra-subband (Drude-like) optical transitions in the lowest size-quantized conduction subband $e1$, because the photon energies are smaller than the subband separation and much larger than the $\boldsymbol{k}$-linear spin splitting. For this purpose an optically pumped molecular NH_3 laser was applied [43]. The emitted radiation with a pulse length of about 100 ns at the wavelength $\lambda = 90$, 148 and 280 µm (corresponding photon energies $\hbar\omega$ are 13.7 meV, 8.4 meV and 4.4 meV) has a peak power of about 10 kW. As sketched in the inset of Fig. 17, showing the experimental geometry, the samples were irradiated along the growth direction. In Section 3.4.1 the investigated (110)-grown structures are described with their corresponding sample parameters. An optical cryostat allowed to investigate the MPGE in a wide temperature range from 4.2 K to 293 K. In addition an external magnetic field, varied from $B = -0.8$ T to $B = 0.8$ T, was applied either parallel (along y) or normal to the QW (parallel to z) generated by a conventional water cooled electromagnet. The photocurrent was observed in unbiased structures via the voltage drop across a 50 Ω load resistor and after amplification recorded with a storage oscilloscope. An important detail is given by the signals temporal behavior, which should reproduce the shape of the excitation pulse, ensuring the involvement of fast relaxation processes in the current generation. In addition to the MPGE measurement, time-resolved Kerr rotation was applied to investigate the spin dynamics in the samples. This was done in cooperation with the group of Prof. Schüller and is described in Section 3.5.

In the absence of the magnetic field samples A, B and D show a response under illumination with linearly or circularly polarized radiation. The observed photocurrents represent the linear and circular photogalvanic effects will be discussed in Section 4.4. As the following experiments are focused on the MPGE, the magnetic field independent background is eliminated in the polarization and temperature dependences by

$$J^{\mathrm{MPGE}} = [J(+\boldsymbol{B}) - J(-\boldsymbol{B})]/2. \tag{34}$$

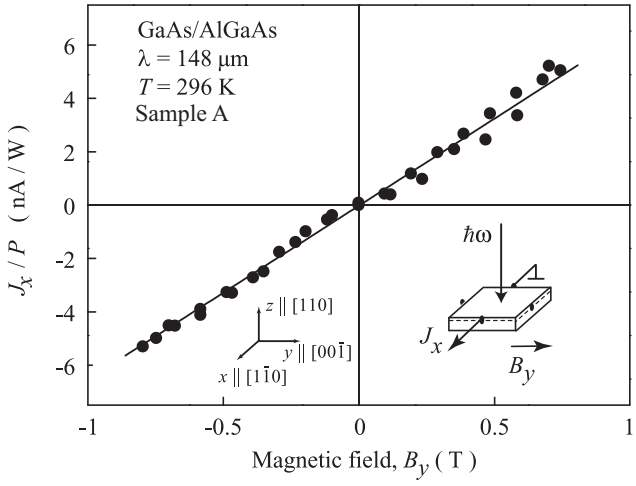

Figure 17: Magnetic field dependent photocurrent in sample A at RT and magnetic field $\boldsymbol{B}$ parallel to the y-axis. The sample was illuminated under normal incident unpolarized radiation ($\lambda = 148$ μm). The inset shows the sketch of the experimental setup excluding magnetic field independent currents. The linear in B fit is after Eqs. (35) and (36).

As a result of this the MPGE, which is an odd in $\boldsymbol{B}$ contribution and therefore, changes its sign upon switching the magnetic field direction, is extracted from the experimental data. This equation was not applied for the measurements of the current under variation of the magnetic field, because the chosen geometry and the orientation of the radiation polarization exclude photogalvanic effects at $B = 0$.

The samples A, B and D show under irradiation with normal incident unpolarized radiation a photocurrent $\boldsymbol{J}$ in the direction, which is perpendicular to the applied external in-plane magnetic field $\boldsymbol{B}$ (transverse geometry). The polarization state of the initially linearly polarized radiation was unpolarized via a brass cone (150 mm length with an angle of 4°) which depolarizes the radiation due to multiple reflections in the cone. In the theoretical description the current density j is used, while in the experiment the electric current J, which is proportional to the current density, is measured. Figure 17 shows the corresponding magnetic field dependence of J/P detected in sample A, a single-side doped heterojunction belonging to the point group C_s, under illumination with unpolarized radiation at room temperature (RT). The observed

photocurrent is linear in the magnetic field and changes its sign upon changing the direction of $\boldsymbol{B}$.

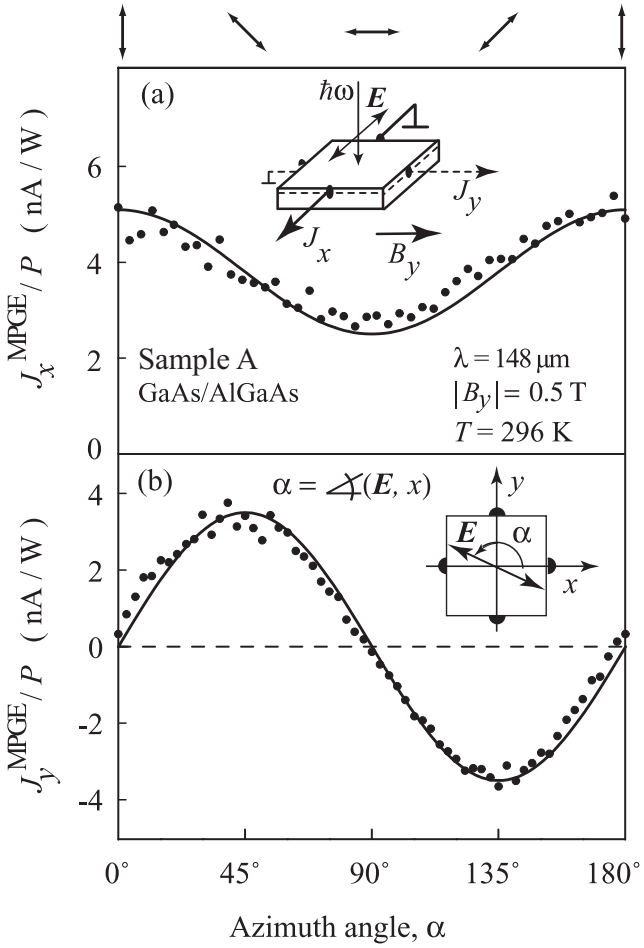

Figure 18: MPGE photocurrent measured in sample A (a) in the transversal geometry along x and (b) in the longitudinal geometry along y as a function of angle α for a magnetic field applied in y-direction. The photocurrents are excited by linearly polarized radiation with the wavelength $\lambda = 148$ μm, power $P \approx 5$ kW and temperature $T = 296$ K. Full lines are fits to Eqs. (35) and (36) with corresponding polarization dependences given by Eqs. (37) and (38). On top, the linear polarization corresponding to various angles α is plotted. The inset shows the experimental geometry. An additional inset in the lower panel displays the sample and the radiation polarization viewing from the source of radiation side.

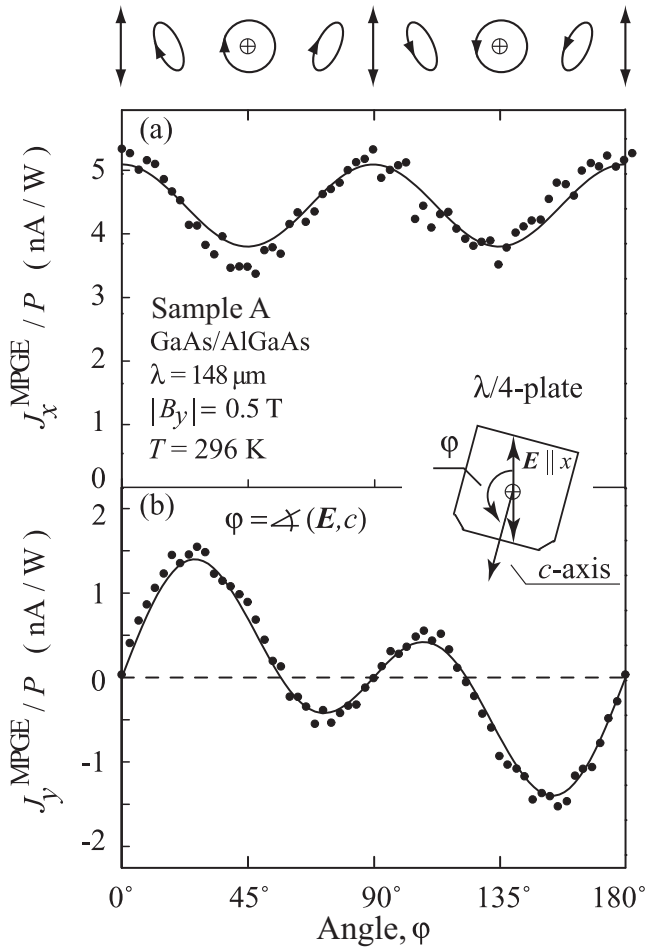

Figure 19: MPGE photocurrent measured in sample A (a) in the transversal geometry along x and (b) in the longitudinal geometry along y as a function of the angle φ for a magnetic field applied in y-direction. The photocurrents are excited by linearly polarized radiation with wavelength $\lambda = 148$ μm, power $P \approx 5$ kW and temperature $T = 296$ K. Full lines are fits to Eqs. (35) and (36). On top, the polarization ellipses corresponding to various angles φ are plotted. Full lines are fits of the photocurrent to the sum of Eqs. (35) and (36) as well as (39) and (40) with corresponding polarization dependence given by Eqs. (41) to (43).

The dependence of the magnetic field induced photocurrent on the variation of the linear polarization, utilizing a $\lambda/2$-plate, is shown in Fig. 18 for sample A in two different geometries. Figure 18(a) represents J_x^{MPGE} measured

perpendicular to the magnetic field B_y (transversal geometry). The case of J_y^{MPGE} parallel to B_y, shown in Fig. 18(a), is named longitudinal geometry. Both J_x^{MPGE} and J_y^{MPGE} show a clear dependence on the azimuth angle α.

Figures 19(a) and (b) show the signal in dependence on the rotation of the $\lambda/4$-plates, described by the angle φ, for both geometries. The various contributions to the formation of these photocurrents are characterized by different dependences of the photocurrent magnitude on the radiation polarization state, as well as the orientation of the magnetic field with respect to the crystallographic axes. The results obtained for $\lambda = 90$ μm, $\lambda = 148$ μm and $\lambda = 280$ μm are qualitatively the same and therefore, only the data obtained for $\lambda = 148$ μm are presented.

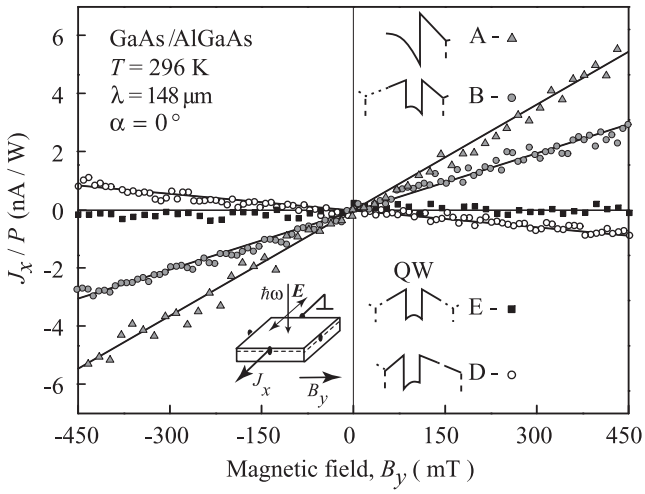

Figure 20: Magnetic field dependences of the photocurrents measured in x-direction for the radiation polarized along x and the in-plane magnetic field $\boldsymbol{B} \parallel y$ for the four samples A, B, D and E. The magnetic field independent background (see Sec. 4.4) is subtracted. The left inset shows the experimental geometry. Four right insets show the band profile and the δ-doping position of the investigated samples.

Figure 20 shows the experimental data of J_x dependent on the magnetic field strength B_y for the four samples A, B, D and E. The set of data is obtained at room temperature and fixed linearly polarized radiation with $\boldsymbol{e} \parallel x$. Samples A and B show a linear dependence of the photocurrent on the magnetic field,

both with positive slope, while the signal vanishes for the symmetrically grown sample E. In contrast sample D, which is an asymmetrically grown QW with inverted asymmetry compared to sample B (see insets of Fig. 20), emerges a current with a negative slope.

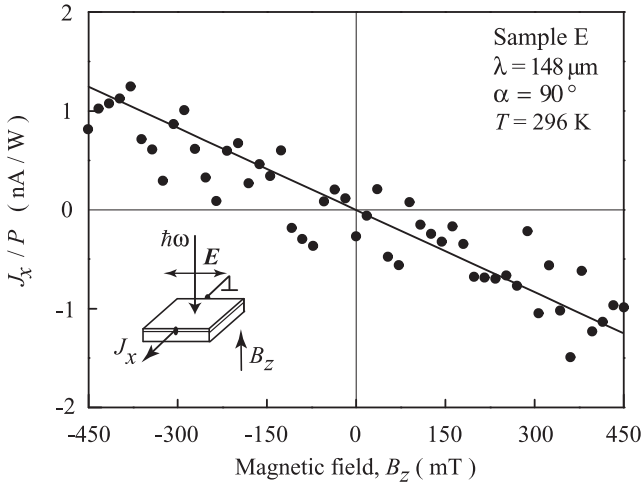

Figure 21: Magnetic field dependence of the photocurrent J_x for sample E measured for radiation polarized along x and a magnetic field perpendicular to the QWs at $T = 296$ K.

In order to investigate the MPGE in the symmetric sample E the magnetic field was oriented along the growth direction, parallel to the incident radiation. Figure 21 shows the photocurrent J_x in dependence of B_z at room temperature and a fixed linearly polarized radiation along x. A similar result was obtained for sample A, for which the dependence on the rotation of the linearly polarized radiation in the presence of a magnetic field B_z is shown in Fig. 22.

4.1.2 Discussion

An easy access to understand the experimental results constitutes the analysis of the samples symmetry, as well as the knowledge of the transformation of polar and axial vectors in these systems. In the experiments discussed in this chapter (110)-grown GaAs quantum wells belonging to zinc-blende structure were investigated under normal incident radiation. For this types of samples the symmetry, which is affected drastically by the equivalence or

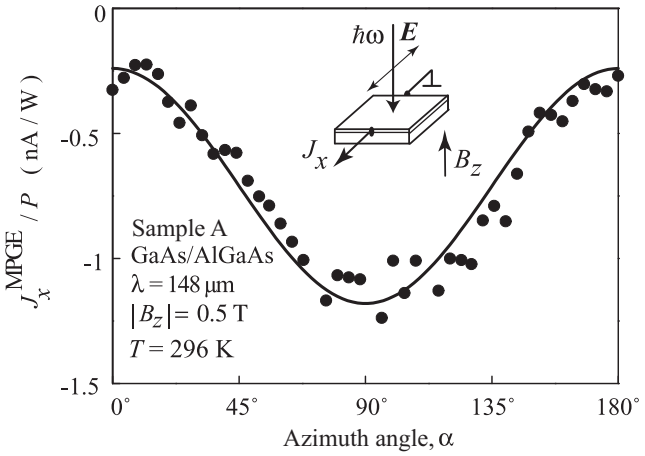

Figure 22: Photocurrent J_x^{MPGE} as a function of angle α measured at for sample A normal incidence for a magnetic field perpendicular to the QWs. The photocurrent is excited by linearly polarized radiation with the wavelength $\lambda = 148$ μm, power $P \approx 5$ kW and temperature $T = 296$ K. Full lines are fits to Eqs. (35) and (36). The inset shows the experimental geometry.

non-equivalence of the QW interfaces, plays an important role. They belong either to the C_{2v} or C_s symmetry class (symmetric and asymmetric samples, respectively). Here it should be noted that the C_{2v} point group describes asymmetrically (001)-grown GaAs QWs as well, but the important difference is the orientation of its two mirror planes perpendicular to the QW plane.

However, in Fig. 23 the symmetry elements of both, the symmetrical and asymmetrical (110)-grown QWs are shown in the coordinate frame with the in-plane axes $x \parallel [1\bar{1}0]$ and $y \parallel [00\bar{1}]$, and the growth direction $z \parallel [110]$. By taking into account symmetry considerations the phenomenological equation (5) can be analyzed. It shows that a photocurrent $\boldsymbol{j}$ is allowed to flow only if its in-plane component transforms in the same way as the product of components of the magnetic field $\boldsymbol{B}$ and polarization vector $\boldsymbol{e}$. For simplification in the following unpolarized radiation is considered. In this particular case the photocurrent is determined by a coupling of a polar vector $\boldsymbol{j}$ to an axial vector $\boldsymbol{B}$, because $\left(e_\gamma e_\delta^* + e_\delta e_\gamma^*\right) = \delta_{\gamma,\delta}$ becomes an invariant and $P_{\mathrm{circ}} = 0$. The symmetry elements of the C_s point group, to which asymmetric (110)-grown structures

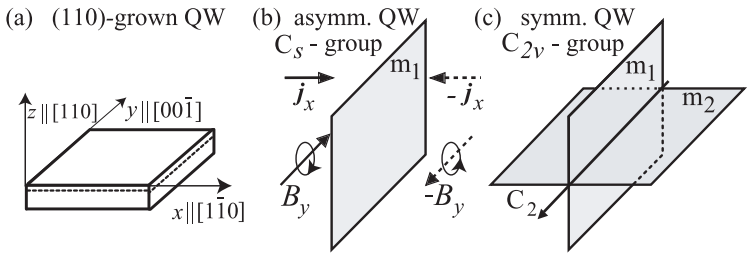

Figure 23: (a) Sample orientation with corresponding coordinate system, (b) shows the mirror planes of symmetric and (c) of asymmetric QWs grown along $z \parallel [110]$. (b) shows the reflection of the polar vector component j_x and axial vector component B_y at the plane m_1, which allows a linear coupling $j_x \propto B_y$ for asymmetric QWs. This coupling is forbidden for (c) symmetric QWs, because the mirror plane m_2 does not modify j_x but changes the sign of the in-plane component of the axial vector B_y.

belong, are the identity and the mirror reflection plane $m_1 = (yz)$ normal to the x-axis. Studying the reflection of axial and polar vectors on m_1 shows that the current component j_x and the magnetic field component B_y transform in the same manner ($j_x \to -j_x$, $B_y \to -B_y$), see Fig. 23(b). In the same way the coupling $j_x \propto B_y$ is allowed, two further contributions emerge: $j_y \propto B_x$ and $j_x \propto B_z$. Resulting from this the generation of a magnetic field-induced photocurrent is possible for both in-plane and out-of-plane magnetic fields and was also observed experimentally. Exactly this case is shown in Fig. 17 in which the photocurrent J_x is linearly increasing with the magnetic field B_y in response to the illumination of the asymmetric sample A with unpolarized radiation.

The situation drastically changes for the symmetrically (110)-grown QW (sample E). While a linear in $\boldsymbol{B}$ photocurrent J_x was observed for a magnetic field oriented along the z-direction, see Fig. 21, no signal was detected for an in-plane magnetic field. This result is in contrast to sample A and stems from the higher point-group symmetry C_{2v} of sample B. This point group contains an second mirror plane m_2 laying for this kind of samples parallel to the interface plane, see Fig. 23(c). The transformation of axial and polar vectors keeps unchanged in respect to m_1, but changes taking into account m_2. The

in-plane components of the polar vector $\boldsymbol{j}$ are not modified by the reflection in m_2, whereas the in-plane components of the axial vector $\boldsymbol{B}$ change their polarity. This non equal behavior under a symmetry operation forbids a linear coupling of the current with the in-plane magnetic field. The only remaining contribution is the coupling between j_x and B_z, because they transform in the same way under m_1 and m_2. This shows that only in the presence of a magnetic field B_z a photocurrent j_x can be induced in symmetric (110)-oriented QWs, as observed in the experiment. Due to the fact that symmetric and asymmetric (110)-grown QWs emerge a significant different behavior in the photocurrent generation, as shown by this analysis, the MPGE is an ideal tool to measure the degree of asymmetry of (110)-grown heterostructures. Here, a magnetic field dependent photocurrent in the presence of an in-plane component of $\boldsymbol{B}$ can only be observed in asymmetric structures and vanishes for symmetric QWs.

However, for a detailed analysis of the experimental results it is necessary to take into account the phenomenological theory and the polarization of the radiation. This includes components of the polarization vector and therefore, results in additional polarization dependent contributions to the photocurrent. In the following the discussion of the MPGE, including its polarization dependence, for symmetrical and asymmetrical structures is presented.

For the case of asymmetrical structures (C_s point group) the extension of Eq. (5) and its limitation to normally incident and linearly polarized light leads to terms described by nine linearly independent constants $S_1 \dots S_9$ (see Table 2), given by

$$\begin{aligned} j_x/I = {} & S_1\, B_y + S_2 B_y(|e_x|^2 - |e_y|^2) + S_3 B_x(e_x e_y^* + e_y e_x^*) \\ & + S_4\, B_z + S_5 B_z(|e_x|^2 - |e_y|^2)\,, \end{aligned} \tag{35}$$

$$\begin{aligned} j_y/I = {} & S_6\, B_x + S_7 B_x(|e_x|^2 - |e_y|^2) + S_8 B_y(e_x e_y^* + e_y e_x^*) \\ & + S_9\, B_z(e_x e_y^* + e_y e_x^*)\,. \end{aligned} \tag{36}$$

Equations (35) and (36) can be simplified by the expressions

$$P_{\mathrm{lin}} = s_2/s_0 = (e_x e_y^* + e_y e_x^*) = \sin 2\alpha\,, \tag{37}$$

$$P'_{\mathrm{lin}} = s_1/s_0 = (|e_x|^2 - |e_y|^2) = \cos 2\alpha\,, \tag{38}$$

where α is the azimuth angle, defined as the angle between the plane of linear polarization and the sample's x-axis.

The terms on the right-hand side of the Eqs. (35) and (36), described by the constants S_1, S_4 and S_6, are independent on the linear polarization and thus, arise under excitation with unpolarized radiation. The magnetic field induced photocurrent can be excited by elliptically or circularly polarized radiation as well. In addition to the terms describing the dependence on the linearly polarized (parameters S_2, S_3, S_5, S_7, S_8, S_9) and unpolarized light (parameters S_1, S_4, S_6), see Eqs. (35) and (36), new helicity dependent contributions appear given by

$$j_x^{\rm circ}/I = S_{10} B_x P_{\rm circ} \,, \tag{39}$$

$$j_y^{\rm circ}/I = S_{11} B_y P_{\rm circ} + S_{12} B_z P_{\rm circ} \,. \tag{40}$$

The rotation of a $\lambda/4$-plate in respect to the initial linearly polarized laser radiation leads to linearly, elliptically and circularly polarization. The variation of the polarization state can be described taking into account the Stokes parameters as follows

$$P_{\rm lin} = s_2/s_0 = (e_x e_y^* + e_y e_x^*) = 1/2 \sin 4\varphi \,, \tag{41}$$

$$P'_{\rm lin} = s_1/s_0 = (|e_x|^2 - |e_y|^2) = 1/2(1 + \cos 4\varphi) \,, \tag{42}$$

$$P_{\rm circ} = s_3/s_0 = \sin 2\varphi \,, \tag{43}$$

where φ is the angle between the optical axis of the $\lambda/4$-plate and the direction of the initial polarization. The two Stokes parameters s_2 and s_1, already present in the Eqs. (37) and (38), describe the degrees of linear polarization $P_{\rm lin}$ and $P'_{\rm lin}$ along the bisector (xy) and the x- or y-axis, respectively. They vanish if the radiation is circularly polarized. In this case the third Stokes parameter s_3 describes the radiation helicity $P_{\rm circ}$. It is zero for linearly polarized radiation and reaches ± 1 for right- or left-handed circular polarization.

The microscopic model of the MPGE discussed in Section 2.3.2 is described by an asymmetric scattering of carriers, based on Eq. (9), in the relaxation and excitation mechanism, see Fig. 3(a) and (b). This processes lead to spin currents, which are transformed into a net electric current in the presence of an

$S_1=\frac{1}{2}(\phi_{xyxx}+\phi_{xyyy})$	$S_2=\frac{1}{2}(\phi_{xyxx}-\phi_{xyyy})$
$S_3=\phi_{xxxy}=\phi_{xxyx}$	$S_4=\frac{1}{2}(\phi_{xzxx}+\phi_{xzyy})$
$S_5=\frac{1}{2}(\phi_{xzxx}-\phi_{xzyy})$	$S_6=\frac{1}{2}(\phi_{yxxx}+\phi_{yxyy})$
$S_7=\frac{1}{2}(\phi_{yxxx}-\phi_{yxyy})$	$S_8=\phi_{yyxy}=\phi_{yyyx}$
$S_9=\phi_{yzxy}=\phi_{yzyx}$	$S_{10}=\mu_{xxz}$
$S_{11}=\mu_{yyz}$	$S_{12}=\mu_{yzz}$

Table 2: Definition of the parameters S_i $(i=1\ldots9)$ in Eqs. (35) and (36) as well as Eqs. (39) and (40) in terms of non-zero components of the tensors $\boldsymbol{\phi}$ and $\boldsymbol{\mu}$ for asymmetric (110)-grown heterostructures. Normal incidence of radiation along the z-axis is assumed.

in-plane magnetic field (Fig. 4). The electric current resulting from the excitation mechanism of the MPGE, carries a characteristic polarization dependence given by the terms being proportional to $S_2,\ S_3,\ S_5,\ S_7,\ S_8$ and S_9 in Eqs. (35) and (36). In the same way the asymmetric scattering modifies the excitation process, it influences the energy relaxation of the photoexcited carriers. The photocurrent due to this mechanism is independent on the polarization and is described by the terms proportional to S_1, S_4 and S_6 on the right hand side of Eqs. (35) and (36). In the experiment, the MPGE in the longitudinal geometry is detected for linear and circular polarized radiation, whereas the signal in the transversal direction was observed for linear- and unpolarized radiation. The results observed in both geometries are in full agreement with Eqs. (35 and 36), valid for asymmetric samples with broken structure inversion.

The dependence of the photocurrent strength on the orientation of the polarization plane of linearly polarized radiation, given by the angle α is shown in Fig. 18. Obviously, the current J_x^{MPGE} and J_y^{MPGE} can be fitted with an offset plus cos 2α and sin 2α, respectively. This is in accordance to the Eqs. (35) and (36) described by the three photocurrent contributions proportional to the parameters S_1, S_2 and S_8. The first contribution described by S_1 in the transverse geometry is even present, if the experiment is carried out with unpolarized radiation, see Fig. 17 and is of the same magnitude. The orientation of the magnetic field along the z-direction allows the investigation of the po-

larization independent S_4, as well as the polarization dependent parameters S_5 and S_9. Figure. 22 demonstrates the photocurrent J_x^{MPGE} for a magnetic field B_z detected in the single heterojunction (sample A) in dependence on the linear polarization. The current can be fitted by an offset and a $\cos 2\alpha$ function, reflecting the parameters S_4 and S_5 and is in good agreement with Eqs. (35) and (36).

Elliptically as well as circularly polarized radiation are allowed to induce a magnetic field dependent photocurrent J^{MPGE}, shown in Fig. 19 for sample A as a function of the angle φ. The dependence for the transverse and longitudinal geometry is represented in Fig. 19(a) and (b). They can be fitted by Eqs. (35) and (36) taking into account Eqs. (41) to (43). The fit parameters used for S_1, S_2, and S_8 correspond to those obtained in the experiments with purely linearly polarized radiation. In the presence of elliptically polarized light an additional helicity dependent current is permitted in the longitudinal geometry. This is in agreement with Eqs. (39) and (40), which additionally contain a term proportional to the parameter S_{11} and radiation helicity P_{circ}. Thus, the longitudinal current can be separated into two parts. The first one is described by the coefficient S_8 in the presence of linear and elliptical polarization. The second part is denoted by S_{11}, which reaches its maximum value for purely circular polarization and is zero for linear polarized light. A characteristic of the latter photocurrent is that a change in sign is not only observed under reversing the magnetic field direction, but as well under switching the helicity of the radiation from right- to left-handed, described by $J_y/I \propto B_y P_{\mathrm{circ}}$.

So far a contribution to the magnetic field induced photocurrent, which is proportional to the light helicity P_{circ}, has been observed in (001)-grown heterostructures only and is referred as the spin-galvanic effect [62]. This effect results from an optical orientation of carriers generated by the illumination of the sample by circularly polarized light. As in (001)-grown heterostructures only in-plane components of the spin orientation are allowed to drive a current, the presence of a magnetic field is required. The applied magnetic field induces, in a plane perpendicular to its direction, a Larmor precession of the oriented electronic spins, where the rotation direction changes under reversing the magnetic field, known as Hanle effect. A current now results due to

asymmetric spin relaxation processes leading to a equilibrium spin orientation. Generally speaking, the spin-galvanic current does not require the application a magnetic field, it may be considered as a magneto-photogalvanic effect under the above experimental conditions.

In (110)-grown symmetrical structures (C_{2v} point group) the equivalence of the QW interfaces is the reason for the appearing of a second mirror plane m_2. It lays perpendicular to the growth direction z, which is oriented along the impurities induced electric field. Polar vectors with components being parallel to m_2 (e_x, e_y, j_x, j_y) as well as out of plane components of axial vectors (B_z) are invariant under reflection on this mirror plane. In contrast the in-plane components of axial vectors (B_x, B_y) change their sign. Considering normally-incident light and the Eqs. (35) and (36) for linearly together with Eqs. (39) and (40) for circularly polarized light allows to describe the MPGE in symmetrical (110)-oriented QW structures, where $S_1,\ S_2,\ S_3,\ S_6,\ S_7,\ S_8,\ S_{10},\ S_{11} = 0$, by

$$j_x/I = S_4 B_z + S_5 B_z(|e_x|^2 - |e_y|^2)\ , \tag{44}$$

$$j_y/I = S_9 B_z(e_x e_y^* + e_y e_x^*) + S_{12} B_z P_{\mathrm{circ}}\ . \tag{45}$$

In contrast to the asymmetric structures, the current in the longitudinal and transversal geometry is forbidden for an in-plane magnetic field in the fully symmetric QW (sample E). This is due to the absence of the structure inversion asymmetry, and indeed not observed in the experiment. A symmetrical doping of (110)-grown QWs in fact results in a symmetric sample. This is due to the low growth temperature, which suppresses the segregation process of doping atoms during the growth of uncompleted layers [19].

The phenomenological equations and the polarization dependent measurements already demonstrated a significant difference in the magnetic field dependent photocurrent between symmetric and asymmetric samples. This can be utilized to detect the degree of asymmetry of (110)-grown QWs, reflecting the strength of SIA. Figure 20 shows the experimental data of the current J_x dependent on the magnetic field strength B_y for the samples A to E, obtained at room temperature and fixed linearly polarized radiation with $\boldsymbol{e} \parallel x$. For this geometry, the MPGE current for asymmetric (110)-grown QWs (samples A,

B, and D belong to the C_s point group) is given by $j_x/I = (S_1 + S_2)B_y$, whereas for symmetric (110)-grown QWs (Sample E belongs to the C_{2v} point group) it vanishes, so that $j_x/I = 0$. Phenomenologically the coupling of the x-component of the current (polar vector) with components of the magnetic field (axial vector) is determined, because $|e_x|^2$ is an invariant in (110)-grown structures. For the case of a magnetic field oriented along the y-direction a current is forbidden for sample E, as observed in the experiment. Taking into account the asymmetrical (110)-grown samples A, B and D, a current $J_x(B_y)$ is allowed and its magnitude strongly depends on the doping profile, as displayed in Fig. 20. Furthermore, following from the symmetry arguments, presented above, the MPGE for an in-plane $\boldsymbol{B}$-field stems from the structure inversion asymmetry and as a result it is proportional to the SIA coefficient. Therefore, if the doping layers are asymmetrically shifted off the barrier center from the left to the right side of the QWs (from sample B to D, see Fig. 13), the slope of the magnetic field dependent photocurrent reverses its sign (see Fig. 20).

A similar result is obtained using unpolarized polarization as shown for sample A in Fig. 17, which only differs in the magnitude due to the absence of the contribution described by the coefficient S_2. In addition to the above measurements Sample A was rotated by 90° so that the $\boldsymbol{B}$-field was oriented along the x-axis and the current is measured along the y-axis. In this geometry the detected signals are of the same magnitude and emerge a similar polarization dependence as before. These measurement prove the axial symmetry of the signal expected for the SIA contribution in a strongly asymmetric heterojunction.

The analysis of the data obtained from Fig. 20 clearly demonstrates that the MPGE in (110)-grown structures can be effectively used for measuring the degree of the structure asymmetry. From the absence of any photocurrent for an in-plane magnetic field in sample E it follows that the QW is highly symmetric and lacks the structure asymmetry. An important information is given by the two opposite slopes, observed for samples B and D with the same QW width. It clearly demonstrates that the sign of $(S_1 + S_2)$ can be inverted easily by reflecting the doping position with respect to the QW center.

For a special case, if the magnetic field is oriented perpendicularly to the quantum well plane, the MPGE is allowed for both symmetrical and asymmetrical structures, according to Eqs. (35) and (36) as well as (44) and (45). Indeed, the MPGE photocurrent for B_z is observed for all samples and is induced by BIA. For sample E it has been shown in Fig. 20 that no current is observed for an in-plane magnetic field. Changing $\boldsymbol{B}$ from in-plane to normal to the QW plane a currents arises, see Fig. 21. The signals observed for an out-of-plane B_z field stem from the BIA term, described by Eqs. (44)-(45) and are present in sample A as well (shown in Fig. 22). Hence, measurement of the MPGE gives us an experimental handle to analyze the inversion asymmetry in (110)-oriented structures.

4.2 Time-resolved experiments

In order to support the experimental results of the MPGE measurements time-resolved Kerr Rotation was applied to extract the corresponding spin relaxation times of the symmetric QW sample E and the asymmetric QW sample B.

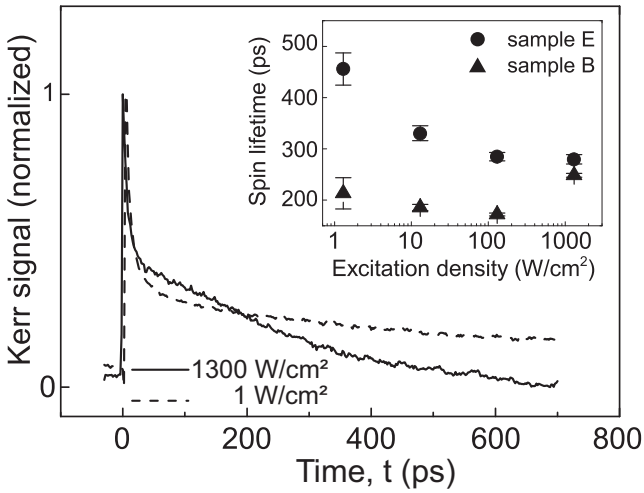

Figure 24: Normalized TRKR traces measured on sample E at 4 K, with high (1300 W/cm^2) and low (1 W/cm^2) excitation density. The inset shows the spin lifetime as a function of the excitation density at 4 K for samples E and B.

In Figure 24 the time dependence of the normalized TRKR signal for sample E for two different excitation densities, low (1300 W/cm^2) and high (1 W/cm^2) excitation, at 4 K are presented. The maximum in the Kerr signal at $t = 0$ ps results from spin-polarized photocarriers excited by the circularly polarized pump pulse and decays rapidly due to the relaxation of the photogenerated holes. In QWs this is known to be a very fast relaxation process, in the order of a few picoseconds [63]. The inset of Fig. 24 shows the extracted spin lifetime as a function of the excitation density at 4 K for samples E and B.

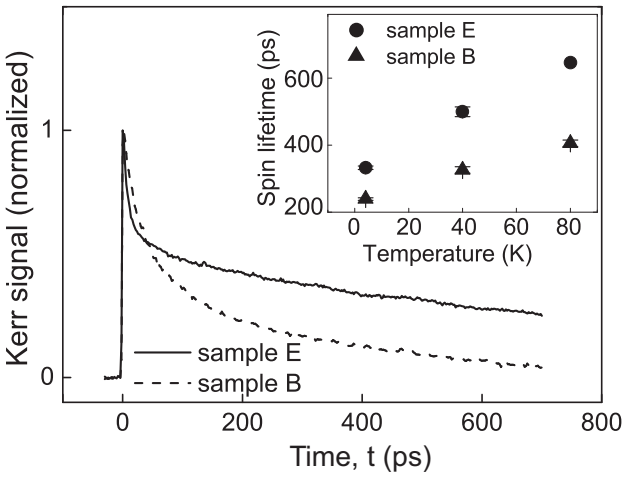

Figure 25: Normalized TRKR traces measured on samples E and B at 40 K with high excitation density. The inset shows the spin lifetime as a function of the sample temperature for both samples.

The traces in Fig. 25 show the corresponding normalized TRKR traces measured at 40 K and high excitation density in the samples B and E. Again the typical peak, already discussed for the excitation intensity dependent measurements, is observed in the Kerr signal in the first few ps after excitation. In the following the spin lifetime is investigated as a function of the sample temperature, shown in the inset of Fig. 25.

4.2.1 SIA and BIA in (110)-grown structures

In a similar way the symmetry of the the sample influences the MPGE the structure and bulk inversion asymmetry affects the spin relaxation in QW

structures. Thus, in the following BIA and SIA, which emerge a spin splitting of the electron subbands are discussed. The structure inversion asymmetry in (110)-grown 2-dimensional structures results in the Rashba spin splitting H_{SO}^{SIA} in the electron subbands, which can be described by an in-plane effective magnetic field $B_{eff}^{\mathrm{SIA}}(k)$, resulting from an electric field along the growth direction, see Fig. 26(b). In the absence of SIA only the bulk inversion asymmetry is present leading to the Dresselhaus spin splitting H_{SO}^{BIA}, representing a effective magnetic field $B_{eff}^{\mathrm{BIA}}(k)$ normal to the QW-plane. The corresponding Hamiltonian is given by [31]

$$H_{SO}^{\mathrm{SIA}} = \beta^{\mathrm{SIA}}(\sigma_x k_y - \sigma_y k_x), \tag{46}$$

$$H_{SO}^{\mathrm{BIA}} = \beta^{\mathrm{BIA}}(\sigma_z k_x). \tag{47}$$

The spin splitting due to BIA is shown in Fig. 26(a). Both terms in Eqs. (46) and (47) are valid for (110)-grown structures in the coordinate frame $x \,||\, [1\bar{1}0]$, $y \,||\, [00\bar{1}]$ and $z \,||\, [110]$. The sum of the effective magnetic fields $B_{eff}(k) = B_{eff}^{BIA}(k) + B_{eff}^{SIA}(k)$, which arises from BIA and SIA, is responsible for the spin relaxation according to the D'yakonov-Perel' mechanism.

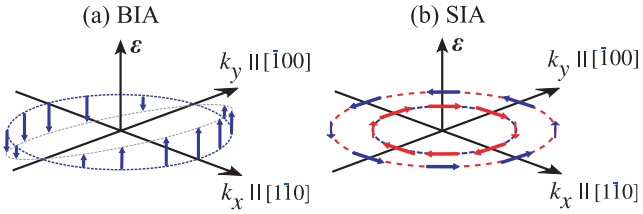

Figure 26: (a) BIA and (b) SIA in (110)-grown zinc-blende type heterostructures.

As already addressed above and observed experimentally, the MPGE reflects the behavior of both SIA and BIA. For the case of symmetric structures, in which only BIA is present the spin splitting is described by Eq. (47). Here the polar vector k_x is coupled to an axial vector σ_z via a second rank pseudo tensor β^{BIA}. This is similar to the first part of Eq. (44), which describes the MPGE for symmetric structures induced by unpolarized radiation. The current j_x is only allowed to flow in the presence of a magnetic field B_z (polar and axial vectors, respectively). In asymmetric structures SIA appears, given by Eq. (46) and is

described by a coupling between σ_x and k_y as well as σ_y and k_x, interconnected by the second rank pseudo tensor β^{SIA}. Again this is reflected in Eqs. (35) and (36) representing the MPGE for asymmetric structures, where the currents j_x and j_y arise for a magnetic fields B_y and B_x for unpolarized radiation, respectively. In addition Eq. (35) still contains the BIA contribution discussed previously since both, SIA and BIA, occur in asymmetric structures.

4.2.2 Discussion

The spin lifetime τ_s can be extracted from the time-resolved Kerr rotation and is demonstrated using the symmetrically doped QW (sample E) and the asymmetrically doped QW (sample B). The spins initially oriented along the z-direction do not precess around the BIA induced effective magnetic field $B_{eff}^{BIA}(k)$, which points along the growth direction. According to the D'yakonov-Perel' relaxation the spin relaxation time of symmetric samples, in which only BIA is present, should be much longer compared to those with SIA, see Section 4.2.1. In asymmetric samples the spins are forced to a precession $\Omega(k)$ around the total effective magnetic field $B_{eff}(k) = B_{eff}^{BIA}(k) + B_{eff}^{SIA}(k)$ and are slightly tilted from their initial orientation. After a scattering event the electron moves in the $\boldsymbol{k}$-space, which forces a reorientation of its spin with respect to $B_{eff}(k)$. Thus, the spin relaxation time τ_s due to the DP mechanism is inverse proportional to the precession $\Omega(k)$ and the scattering time τ_p of the electrons, because in the case of frequent scattering the change in $B_{eff}(k)$ is smaller compared to low scattering rates, see Section 2.4.1. For spins oriented along the z-direction the BIA term does not decrease the spin relaxation time in contrast to the SIA term, which determines the Rashba spin splitting. Therefore, it strongly influences the D'yakonov-Perel' relaxation [2, 4] and can be varied, e.g., due to asymmetric doping.

In order to extract τ_s from the time-resolved Kerr rotation data the process due to the relaxation of the photogenerated holes leading to a strong decrease of the TRKR signal, shown for sample E for short times in Fig. 24, has to be neglected. This is followed by a much slower decay, attributed to the spin relaxation and recombination of the photogenerated electrons. Additionally the time dependence of the normalized TRKR signal for sample E for two dif-

ferent excitation densities, high (1300 W/cm^2) and low (1 W/cm^2) excitation, at 4 K are presented in Fig. 24. Due to the fact that both traces yield a significant different behavior, intensity dependent measurements of τ_s have been performed for samples B and E, shown in the inset of Fig. 24. This results in an increase of the extracted spin lifetimes τ_s with decreasing excitation densities in sample E. Sample B behaves differently, a increase of the spin lifetime is observed for low and high excitation densities, but a decrease for a medium excitation density. The increase in the symmetric n-doped sample E can be attributed on the one hand to a remaining electron spin polarization after photocarrier recombination, because the photogenerated holes partially recombine with unpolarized, resident electrons. Therefore, the Kerr signal consists of a combination of the electron spin relaxation, which dominates in the case of the low excitation density compared to the doping concentration, and the photocarrier recombination, which increases the signal in the case of high excitation densities. On the other hand, in the symmetrically grown sample, where the DP mechanism is vanishingly small for spins aligned along the growth direction, other spin relaxation mechanisms may play a major role. Considering the Bir-Aronov-Pikus mechanism for low temperatures the spin relaxation of electrons includes their interaction with (unpolarized) holes. A decrease of the density of the photocreated holes by reducing the excitation density results in a weaker relaxation via the BAP mechanism. This has been shown recently by spin noise spectroscopy measurements [64], which demonstrate that in the absence of photogenerated holes and therefore a reduced influence of the BAP, the spin lifetime in (110)-grown QWs could reach values above 20 ns.

From the excitation density dependent data, it can be concluded, that in sample B, as it is grown asymmetrically, the DP mechanism dominates the spin relaxation. For this sample the influence of the BAP mechanism is vanishingly small, and a slight increase of the photogenerated holes does not noticeable affect the spin lifetime. The increase of τ_s for the highest excitation density may be due to a higher initial spin polarization, as observed previously in (001)-grown 2D electron systems [65].

For longer times the signal for sample E in Fig. 25 decays significantly slower compared to sample B. The temperature dependent data presented in the in-

set of Fig. 25 is obtained using an exponential fit to the TRKR traces starting at $t = 200$ ps, excluding the hole spin relaxation. In the investigated temperature range the spin lifetime of the symmetrically grown sample E is about 50 % larger compared to that of sample B. This data approves that the Rashba spin-orbit field and thus the spin relaxation via the DP mechanism is absent in sample E in contrast to the asymmetric sample B, where these effects shorten the spin lifetime. Due to the fact, that the temperature-dependent measurements were carried out at a high excitation density of about 1300 W/cm^2, the observed spin relaxation times in sample E are shorter than those in the intrinsic case, which means in the absence of photoexcited carriers.

The data obtained from this experiments allow to confirm the measurements of the MPGE showing that sample B is indeed asymmetric and sample E is symmetric, respectively.

4.3 Temperature dependence of the MPGE

While the behavior of the photocurrent upon the variation of phenomenological parameters, like the crystallographic direction, polarization, magnetic field direction, etc., is qualitatively the same for any mechanism of the current formation, the temperature dependence gives an access to their microscopic origin [18]. First of all the measurements demonstrate that all experimental features, like polarization and magnetic field dependences, persist down to liquid helium temperature. In addition the characteristic behavior of the involved processes should be reflected in the current formation.

The temperature dependence of the transverse to the magnetic field induced photocurrent J_x^{MPGE} was observed in sample A from RT down to 4.2 K at an in-plane magnetic field B_y with a strength of ± 0.45 T. The data is calculated according to Eq. (34) and is presented in Fig. 27. The magnitude at room temperature coincides with the one obtained from the magnetic field dependence shown in Fig. 20. A decrease of the temperature results in a significant increase of the photocurrent strength, which shows a constant behavior for $T \leq 50$ K.

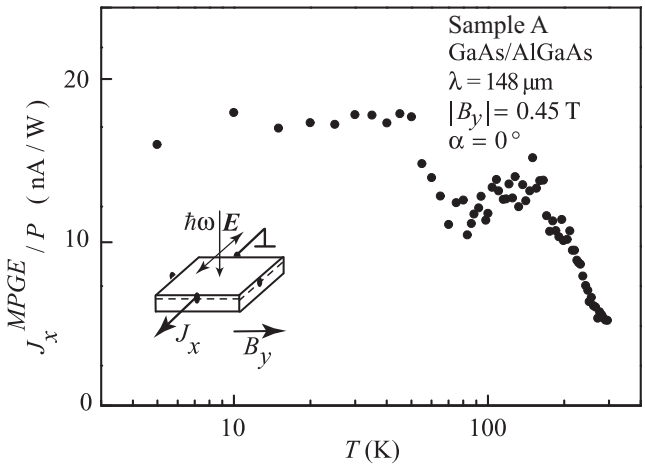

Figure 27: Temperature dependence of the magnetic field induced photocurrent J_x^{MPGE} in the transverse geometry observed in sample A. The data is obtained at an in-plane magnetic field of $|B_y| = 0.45$ T and radiation with $P \approx 10$ kW polarized along x.

Figure 27 demonstrates a similar temperature dependence as previously reported for the MPGE in (001)-oriented GaAs QWs [18]. For a fixed polarization the strength of the magnetic field induced current is governed by the frequency-dependent absorbance $\eta(\omega)$, momentum relaxation time τ_p, light intensity I and average spin S, which is proportional to applied magnetic field B, given by

$$j \propto \eta(\omega) I \tau_p S \propto I n_s S. \tag{48}$$

The different scattering mechanisms, like phonon or impurity scattering, which affect the current and emerge a temperature dependence, are included in the Drude absorption, since $\eta(\omega) \propto n_s/\tau_p$ at $\omega\tau_p >> 1$. To extract the temperature behavior the current formation has two be separated accordingly into a low (impurity scattering dominated) and a high temperature (phonon scattering dominated) region [18]:

i) For low temperatures the average spin is given by $S \propto 1/\varepsilon_F \propto 1/n_s$ and described by the Fermi energy, which determines the carrier density. Thus the current $j/I \propto$ const does not depend on τ_p or n_s and is constant in the low temperature region. In Fig. 27 this behavior can be seen in the region 4.2 K $\leq$ T $\leq$ 50 K.

ii) This is different for high temperatures where the average spin is described by the Boltzmann distribution, so that $S \propto 1/k_B T$. In this case the current $j/I \propto n_s/T$ and yields an inverse temperature dependence, see Fig. 27 for $T > 150\ K$.

iii) In the intermediate temperature region the analysis has so far not been treated theoretically, because there is a superposition of the two dominant scattering mechanism, the impurity and phonon scattering [18].

The increase of the MPGE response at low temperature on the one hand allows the investigation of the temperatures dependence of SIA and on the other hand increases the sensitivity of the method. As expected, sample E did not show a response to the MPGE at low temperature (not shown here), which demonstrates that the structure remains symmetric. This is an important result in respect to a recent work on gate-dependent Kerr measurements, where surprisingly a strong temperature dependence of SIA has been reported [66,67].

4.4 Photocurrents at zero magnetic field

By the discussion of the MPGE in (110)-grown heterostructures it was noted that for this crystallographic orientation a photogalvanic current appears even at zero magnetic field. To extract the magnetic field dependent part from the total photocurrent, Eq. (34) was applied. However, these THz radiation induced photogalvanic effects in (110)-grown QWs, which have been demonstrated for the first time as a result of this work, are of independent interest and will be discussed in this section. These effects can be applied as well for a detector of the Stokes parameters which was developed during this work, but is not included in this thesis [52, 53]. The magnetic independent part of the photocurrent can be obtained by

$$J = [J + (\boldsymbol{B}) + J(-\boldsymbol{B})]/2, \tag{49}$$

showing the same result as the photocurrent measured at zero magnetic field. Thus the, previous experimental setup was used for $\boldsymbol{B} = 0$ T and the samples were illuminated under normal incidence, see inset of Fig. 28. Figures 28(a) and (b) show the observed photocurrent of sample A for $\lambda = 148$ µm as a

function of the azimuth angle α and the angle φ. Both signals show a strong dependence on linearly and circularly polarized radiation.

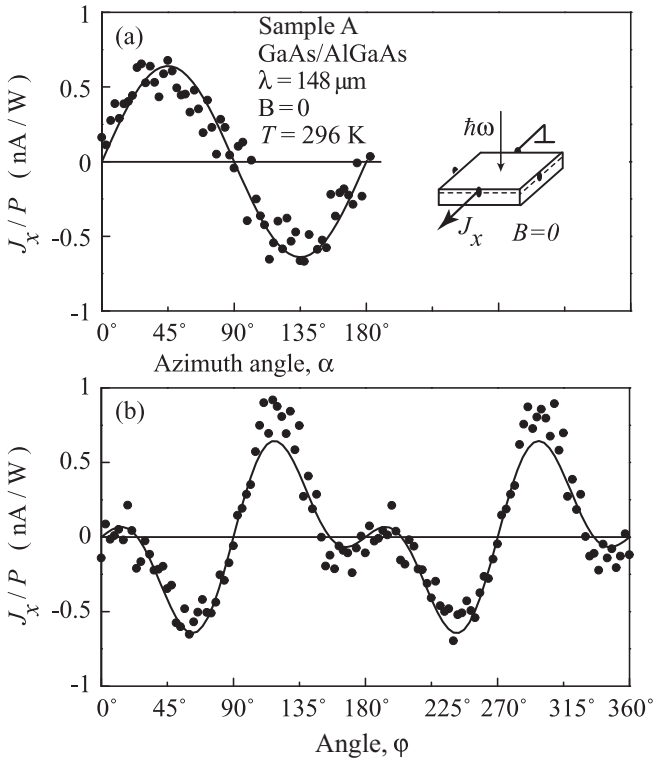

Figure 28: Photocurrent, measured at $\boldsymbol{B} = 0$ T along the crystallographic direction $x \parallel [1\bar{1}0]$ as a function of (a) azimuth angle α and (b) the angle φ for sample A. The photocurrent is excited by radiation with the wavelength $\lambda = 148$ μm, power $P \approx 5$ kW and temperature $T = 296$ K. Full lines are fits to Eqs. (50) and (51). The inset shows the experimental geometry.

The experimentally observed signals under normal incidence of radiation, displayed in Figs. 28(a) and (b) for sample A, can result from two types of photocurrents competing the MPGE and can occur simultaneously, see Section 2.6. The first group depends on the linear and circular polarization of the radiation, the so called linear (LPGE) and circular photogalvanic effects (CPGE), respectively. The second one is proportional to the momentum of light, known as the photon drag effect, which is excluded from the experiment due normal incident radiation [3, 43]. The LPGE and CPGE are allowed in (110)-grown

QWs at normal incidence of light as a result of the specific crystallographic orientation. The CPGE can be described similar to the MPGE, where the in-plane component of the current (j_x, axial vector) transforms in the same way as the out of plane component of the circularly polarized light ($P_{\mathrm{circ}}\hat{e}_z$, polar vector) in respect to m_1. The mirror plane m_2 does not alter the coupling $j_x \propto P_{\mathrm{circ}}\hat{e}_z$ under the assumed conditions. Therefore in both asymmetrical and symmetrical (110)-grown structures, the CPGE is allowed to flow only in one direction, which is perpendicular to m_1.

Phenomenologically the photocurrents for normal incidence of radiation, including the LPGE and the CPGE are given by [3]

$$j_x/I = C_1(e_x e_y^* + e_y e_x^*) + C_2 P_{\mathrm{circ}} \,, \tag{50}$$

$$j_y/I = C_3 + C_4(|e_x|^2 - |e_y|^2) \,, \tag{51}$$

where the parameters C_1 and C_4 describe the linear photogalvanic effect, while C_2 stands for the circular photocurrent, which reverses its direction upon switching the light helicity. The parameter C_3 describes the polarization independent effect. Equations (50) and (51) show that the magnetic field independent photocurrent as well follows the Stokes parameters s_0 to s_3. However, in contrast to the MPGE, the direction and polarization dependence of these currents is now fixed to the crystallographic orientation of the sample and not to the orientation of the magnetic field.

The experiment shows that in the investigated samples the photocurrent at zero magnetic field is mainly driven by the LPGE and results in a carrier flow along the x- and y-directions for linearly as well as for elliptically polarized radiation. Here only the dependence of J_x in sample A obtained at room temperature and zero magnetic field is shown, see Fig. 28. A similar behavior is obtained in all samples. Figure 28(a) shows that $J_x(\alpha)$ is in full correspondence to Eq. (50) and can be fitted with a $\sin(2\alpha)$ function according to the rotation of the linear polarization described by the Stokes parameter $s_2 = P_{\mathrm{lin}}$. The dependence on the radiation helicity φ [see Fig. 28(b)] reveals that in x-direction, being perpendicular to the mirror reflection plane m_1, the circular photogalvanic effect overweights the linear photogalvanic effect. This additional helicity dependent contribution arises from the Stokes parameter

$s_3 = P_{\mathrm{circ}}$ given by the second part on the right side of Eq. (50). In contrast to the LPGE, the CPGE is absent in y-direction (not shown here). The obtained experimental data for the magnetic field independent photocurrents J_x and J_y are in good agreement with the phenomenological Eqs. (50) and (51).

4.5 Summary

In this chapter photocurrents resulting from the MPGE are studied in n-doped zinc-blende based (110)-grown heterostructures. The generation is based on Drude absorption of normally incident THz radiation in the presence of an in-plane and out of plane magnetic field. The obtained experimental results are in full agreement with the phenomenological description which is based on symmetry arguments. Furthermore, the existence of polarization-dependent as well as polarization-independent photocurrents exhibit that the asymmetry in photoexcitation and energy relaxation contribute substantially to the MPGE in (110)-grown heterostructures. The experiments show that the MPGE provides a tool to probe the degree of structure inversion asymmetry, which defines the spin relaxation in (110)-grown QWs. To proof the data from the MPGE experiments, time time-resolved Kerr rotation and luminescence are used to investigate the spin relaxation. Sample E is confirmed independently to be really symmetric by MPGE measurements, showing no current at an in-plane magnetic field, and by TRKR experiments, demonstrating the longest spin relaxation time for the symmetrically doped QWs, setting an upper limit of spin dephasing in GaAs QWs. This is in contrast to (001)-grown structures, where such a growth procedure results in a substantial SIA [32, 68], stemming most likely from an impurity segregation process at high growth temperatures, and subsequently, from the diffusion length of dopant atoms. Indeed, the growth temperature of high-quality (001)-oriented QWs is higher than 600°C, while (110)-structures are grown at 480°C [69]. This difference in the growth temperature leads in the case of (001)-oriented heterostructures to a substantial dopant migration and results in structure asymmetry of nominally symmetrically doped QWs. The investigation of the MPGE, in particular the sign reversal by inversion of the structure asymmetry and the zero current response of the MPGE for symmetrical structures, provides an effective access to study the

symmetry of (110)-oriented QWs. The increase of the photocurrent amplitude with decreasing temperature demonstrates that the MPGE can be applied to investigate the structure inversion asymmetry in a wide range of temperatures including the technologically important room temperature, where many methods, like weak localization or polarized luminescence, hardly can not be used. In summary, the photocurrent measurements provide the necessary feedback to reliably grow structures with long spin relaxation times.

Moreover, these experimental results support the spin-dependent origin of the MPGE, which is directly connected to the g-factor and thus to the Zeeman splitting of the conduction band. However, recently it was demonstrated theoretically that additional contributions can yield a similar magnetic field dependent current based on orbital effects [70]. In contrast to the mechanism of the MPGE based on zero-bias spin separation, this mechanism is not coupled to the spin of the electrons and therefore, yields a current, which is independent on the Zeeman band splitting. To demonstrate that the spin dependent mechanism exists and plays an essential role, DMS structures were chosen. In this type of samples the Zeeman spin splitting can be controllably varied and drastically enhanced by the temperature as well as by the Mn ion concentration. By these parameters even a change of sign of the magnetic field dependent signal upon a variation of the temperature is allowed.

5 Spin currents in diluted magnetic systems

This chapter reports on the observation of the zero-bias spin separation in (001)-grown (Cd,Mn)Te/(Cd,Mg)Te diluted magnetic semiconductors quantum wells and is aimed to proof the spin dependent origin of the MPGE [20]. Up till now pure spin currents in low-dimensional semiconductor structures due to this penomena have been reported only for non-magnetic materials [19, 30, 31]. The described effect is based on the free carrier absorption of THz radiation, causing pure spin currents. In DMS the application of an external in-plane magnetic field, which converts the spin current into a net electric current, is greatly enhanced compared to non-magnetic structures. This is due to two magnetic ion induced contributions. On the one hand, the giant Zeeman spin splitting of the conduction band arises and on the other, the spin-dependent exchange interaction between electrons and magnetic impurities modifies the current formation vastly. The phenomenological and microscopic description of the zero-bias spin separation and the MPGE in DMS samples is based on the description of (001)-grown GaAs structures, discussed in Chapter 2.3. Here the properties of DMS offer a promising option to enhance these spin dependent effects, increased by the exchange interaction between electrons and magnetic ions [4, 13, 20, 40, 71]. In addition, the strength of these effects can be controllably enhanced by varying the temperature, magnetic field and concentration of the magnetic ions.

5.1 Photocurrent Experiments

In order to avoid radiation induced heating of the Mn system, the spin photocurrents were generated under application of low power *cw* radiation of a CH_3OH laser, which was chopped at a frequency of 225 Hz. The emitted radiation has a wavelength $\lambda = 118\,\mu m$ and a power $P \approx 0.5\,mW$ at the sample. In addition a high power pulsed NH_3 laser operating at $\lambda = 148\,\mu m$ and $P \approx 40\,kW$ was utilized to achieve a higher excitation intensity [43]. The energy of the THz photons in the region of $\hbar\omega \approx 10\,meV$ was chosen to be comparable for both laser systems and to induce free carrier absorption only. In the experiment the radiation polarization vector was oriented along the x-axis and

the in-plane magnetic field was aligned along the y-direction. This transversal measurement geometry with normal incidence of radiation in (001)-oriented, unbiased devices excludes other effects known to cause photocurrents and is sketched in the inset of Fig. 29. The electric signals were measured over a pair of ohmic contacts along the crystallographic direction $x \parallel [1\bar{1}0]$ (Fig. 29, inset). The signal at *cw* excitation was picked up across a 1 MΩ load resistor and extracted after amplification by using lock-in technique. In the case of illumination with pulsed radiation, the photocurrent response across a 50 Ω load resistor was amplified and recorded via a storage oscilloscope. The DMS samples A, B and C are described in Chapter 3.4.2 and differ mainly in the Mn^{2+} concentration. The corresponding parameters are summarized in Table 1.

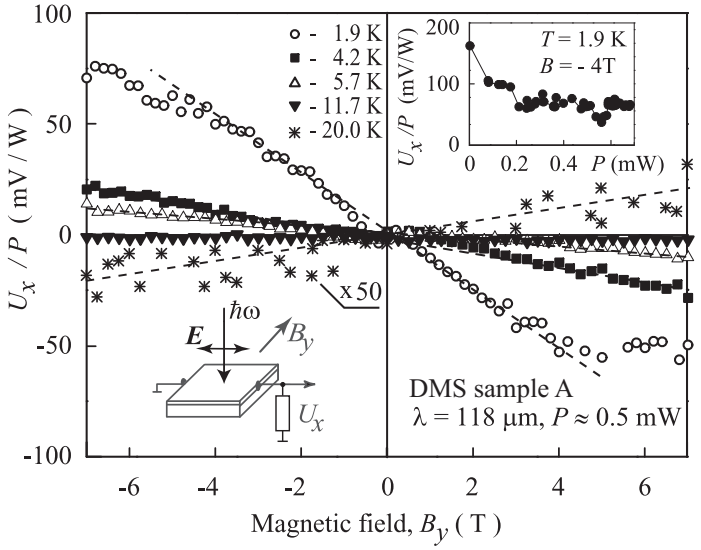

Figure 29: Magnetic field dependence of the photosignal in response to a low excitation power measured in the DMS sample A. The insets show U_x/P as a function of P and the experimental geometry, with the radiation electric field $\boldsymbol{E} \parallel x$ and $\boldsymbol{B} \parallel y$.

In Fig. 29 the signal U_x of DMS sample A under low power *cw* excitation is shown as a function of the in-plane magnetic field B_y. The significant change in sign under reversing the magnetic field direction is observed in a temperature range between 1.9 K and 20 K. As for $T = 20$ K the slope of the signal is positive and linearly increasing with B_y the signal nearly vanishes for $T = 11.7$ K and changes its slope at $T = 5.7$ K. A further cooling down to liquid helium

temperature shows that the currents increases rapidly and finally at $T = 1.9$ K a saturation at high magnetic fields is observed. The inset of Fig. 29 shows intensity dependent measurements of U_x at $T = 1.9$ K and $B = -4$ T. Here the increase of the radiation power P results in a decrease of the normalized signal U_x/P. The same characteristic behavior of the magnetic field dependent signal was obtained for DMS sample B, displayed in Fig. 30(a) for a positive magnetic field. By cooling the sample from 22 K to 5.8 K a sign reversal of the slope is observed. The current increases strongly for lower temperatures and finally for $T = 4.2$ K a saturation sets in for high magnetic fields.

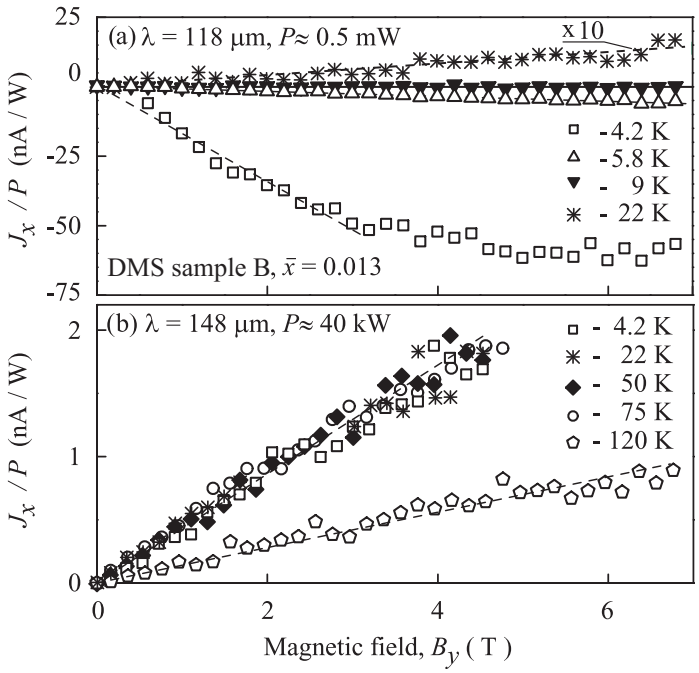

Figure 30: Magnetic field dependence of the photocurrent J_x normalized by the radiation power P measured in the DMS sample B. (a) Low power excitation, (b) high power excitation.

An amplification of the effect in the intensity dependence (addressed above for DMS sample A) was achieved by means of a high power pulsed laser. This, in contrast to the low power excitation, drastically changes the behavior of the photocurrent in DMS sample B, see Fig. 30(b). The photocurrent increases linearly with the magnetic field strength and is nearly independent on T for low temperatures. To investigate this behavior in more detail, the tempera-

ture dependence of the signals was analyzed. Figure 31 shows $J_x(T)$ in DMS sample B for low excitation power at $B = +5$ T. While the photocurrent for $T > 20$ K does not emerge a strong variation and is nearly constant (see inset of Fig. 31), J_x increases strongly for $T < 10$ K, which is in correspondence to Fig. 30(a).

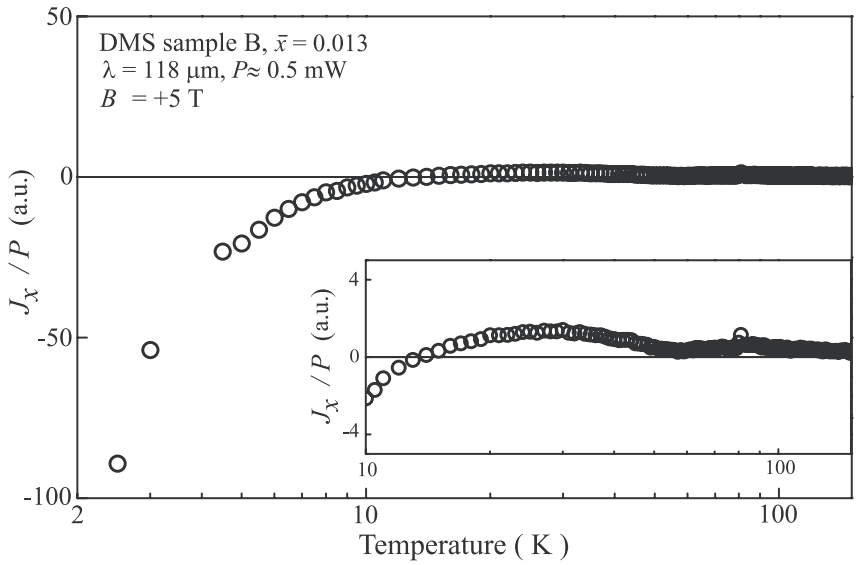

Figure 31: Temperature dependence of J_x/P obtained at low excitation power for DMS sample B. The inset shows the same dependence with a different scale.

A detailed temperature dependence under pulsed excitation is shown in Fig. 32 for DMS sample B and the nonmagnetic reference sample C at a fixed magnetic field $B_y = 4$ T. Remarkably here is the similar behavior of both samples. For $T < 100$ K the photocurrent becomes almost independent of the sample temperature, but decreases with increasing temperature for higher T. As a high excitation intensity results in an increased signal to noise ratio, it is possible to obtain measurable signals at higher temperatures in the DMS samples A and B as well as in the non-magnetic reference sample C (DMS samples B and C are shown in Fig. 32). The inset of Fig. 32 shows $J_x(B_y)$, which is linear in the magnetic field $\boldsymbol{B}$ for the nonmagnetic sample C at $T = 4.2$ K and $T = 70$ K. Its magnitude corresponds to the one obtained in the DMS sample B under high excitation, see Fig. 30.

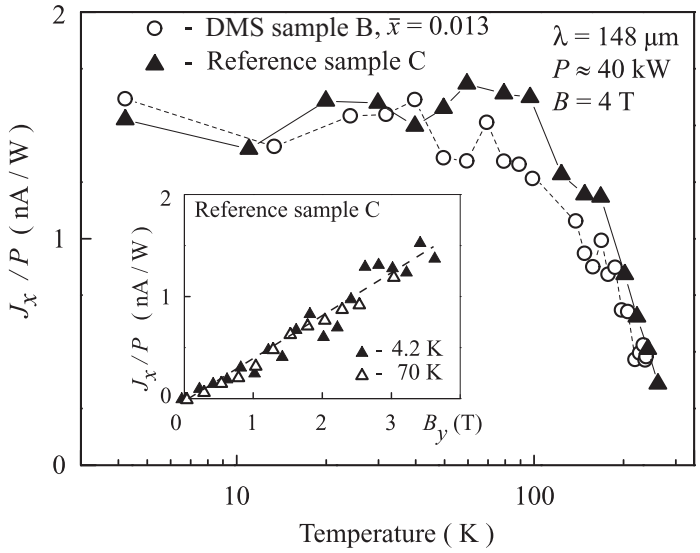

Figure 32: Temperature dependence of J_x/P obtained at high excitation power for DMS samples B and C. The inset shows the $\boldsymbol{B}$ dependence of the photocurrent for sample C at $T = 4.2$ K and $T = 70$ K.

5.2 Discussion

The characteristic behavior, such as a reversal and transition from a linear into a flattening of the magnetic field dependent signal, was obtained for the DMS sample A and B, displayed in Figs. 29 and 30(a), respectively, and is a typical feature for the magnetization of DMS, see Section 2.5. This effect is controlled by the exchange interaction of electrons with Mn^{2+} ions and described by the well-known giant Zeeman splitting [40], also detected in the samples by PL measurements [Fig. 14(c)]. It is attributed to the magnetic field dependence of the electron spin splitting in (Cd,Mn)Te samples, given by [40, 57]

$$E_Z = g_e \mu_B B + \bar{x} S_0 N_0 \alpha \mathrm{B}_{5/2} \left(\frac{5 \mu_B g_{\mathrm{Mn}} B}{2 k_B (T_{\mathrm{Mn}} + T_0)} \right) . \tag{52}$$

The first term on the right hand side of Eq. (52) describes the intrinsic Zeeman spin splitting which is linear in the magnetic field and proportional to the electron g-factor, with $g_e = -1.64$ in the investigated (Cd,Mn)Te samples [72]. The second term is related to the exchange interactions between the Mn^{2+} ions and the conduction band electrons, being proportional to the effective average concentration of Mn $\bar{x}$, the average spin per unity cell S_0 and the exchange

integral $N_0\alpha = 220\,\mathrm{meV}$. It is known as the extrinsic Giant Zeeman spin splitting and its characteristic behavior stems from the modified Brillouin function $\mathrm{B}_{5/2}(\xi)$. Here the magnetic field $\boldsymbol{B}$, the g-factor of the Mn^{2+} ions $g_{\mathrm{Mn}} = 2$, and the Mn-spin system temperature T_{Mn} enters, as well as the parameters S_0 and T_0 taking into account the Mn-Mn antiferromagnetic interaction. This term arises from the description of the magnetization in a paramagnetic system, described by Eq. (19) in Section 2.5.2. Due to the influence of $T_{\mathrm{Mn}} + T_0$ in the denominator of $\mathrm{B}_{5/2}(\xi)$ in Eq. (52) and the opposite signs of g_e and $N_0\alpha$, the strong temperature dependence of the Zeeman splitting, the sign inversion and the saturation of the current can be described. This is illustrated in Figs. 29 and 30(a), where the direction of the photocurrent between $T \approx 22\,\mathrm{K}$ and $T \approx 6\,\mathrm{K}$ changes. This is directly connected to the heating of the lattice temperature T_0. However, the point of sign inversion of the photocurrent does not coincide with the temperature $T \approx 40\,\mathrm{K}$ detected in the PL measurements of the Zeeman splitting. This is related to the heating of the Mn^{2+} spin system above the lattice temperature, indicated by $T_{\mathrm{Mn}} + T_0$ in Eq. (52), and has been reported in [73].

Due to this, intensity dependent measurements were performed, shown in the inset of Fig. 29 for DMS sample A. The data indicates that an increase of the radiation power results in a decrease of the normalized signal, caused by a heating of Mn, affecting T_{Mn}. This reduces the influence of the giant Zeeman splitting. Figure 31 shows the temperature dependence of J_x in DMS sample B at low excitation power and $B = +5$ T. While at high temperatures the intrinsic Zeeman splitting determines the current formation, the influence of Mn^{2+} arises at low temperature and giantly enhances the photocurrent for $T < 10$ K, including an sign inversion.

The application of high power radiation emitted from the pulsed laser induces a very strong heating of the Manganese system and thus, drastically reduces the giant Zeeman interaction. Both, the low and the high power excitation data are shown in Fig. 30(a) and (b). As already discussed, the DMS sample B, displayed in Fig. 30(a), behaves under low power excitation similar to DMS sample A, characterized by a strong temperature dependence and a change in sign of the photocurrent. This behavior vanishes completely for high radiation

power, displayed in Fig. 30(b). The detailed T-dependence under pulsed excitation shown in Fig. 32 indicates that DMS sample B and reference sample C behave similar and reflect the typical temperature dependence of the MPGE in non-magnetic systems. It is explained by Eq. (48) in Section 4.3, emerging a $1/T$ dependence for $T > 100\,\mathrm{K}$ and a nearly constant current for $T < 100\,\mathrm{K}$. Furthermore, this is similar to the discussion of the (110)-grown GaAs heterojunction shown previously in Fig. 27 of Chapter 4.3 and the (001)-grown GaAs heterostructures in [18]. Both methods, high and low excitation, yield a comparable current strength for DMS sample B and reference sample C in the high temperature range. Here, the high intensity leads to a strong heating of the Mn^{2+} spins, destroying the exchange contribution of the magnetic ions to the current formation. The fact that the slopes of the $J_x(B)$ dependences in Fig. 30 detected for $T \approx 20\,\mathrm{K}$ are the same for both excitations indicates that the photocurrent in both cases is due to the intrinsic effect only.

The microscopic mechanisms of the photocurrent are based on σ- and k-dependent terms in the electron phonon interaction $V_{kk'}$, which is the origin of the zero-bias spin separation. It leads to an asymmetry in the Drude like excitation and relaxation of a heated electron gas, see Eq. (9) [18]. While the first mechanism depends on the light's polarization, the latter one is polarization independent. Since only a weak polarization dependence of the photocurrent in DMS at low temperature is observed experimentally (not shown here), the here dominating spin separation mechanism is the energy relaxation of the THz radiation heated electron gas. The model used to describe the asymmetry of the electron-phonon interaction in (110)-and (001)-grown GaAs heterostructures, shown in Fig. 3 of Section 2.3.2, can be applied to describe this effect in (001)-grown CdTe-based QWs. It results in two oppositely directed electron flows $\boldsymbol{i}_{\pm 1/2}$ in each spin subband, which cancel each other until an external magnetic field introduces an imbalance between both fluxes and thus, gives rise to a net electric current $\boldsymbol{j} = e(\boldsymbol{i}_{+1/2} + \boldsymbol{i}_{-1/2})$. As indicated in Fig. 4, this imbalance is induced by the Zeeman splitting of the spin subbands and leads to different free carrier densities $n_{\pm 1/2}$. In DMS the exchange interaction between free electrons and Mn^{2+} ions has a strong influence on this electron spin splitting.

If a very low electron spin polarization is considered, which means $E_Z < \bar{E}$, the equilibrium electron spin per electron is given by $s = -E_Z/(4\bar{E})$. As the charge current is proportional to s, j_Z is given by

$$\boldsymbol{j}_Z = -4e\frac{E_Z}{4\bar{E}}\left(n_e\frac{\partial \boldsymbol{J}_s}{\partial n_e}\right) , \tag{53}$$

where $\bar{E}$ is the characteristic electron energy, equal to k_BT for the non-degenerate gas and ε_F for the degenerate electron gas. Equation (53) relates the spin current to the carrier density n_e and can be separated into two different temperature regimes to solve $\partial \boldsymbol{J}_s/\partial n_e$. The first one is the case in which the Boltzmann statistics is valid. Here $\boldsymbol{J}_s \propto n_e$ and therefore, $n_e\partial \boldsymbol{J}_s/\partial n_e = \boldsymbol{J}_s$. As a consequence for high T Eq. (53) reduces to

$$\boldsymbol{j}_Z = -e\frac{E_Z}{k_BT}\boldsymbol{J}_s . \tag{54}$$

The second case is the very low temperature region, described by the Fermi distribution. Here $\partial \boldsymbol{J}_s/\partial n_e$ vanishes, if the spin current is only caused by linear in $\boldsymbol{k}$ terms in the matrix element of the electron-phonon interaction, whereas it is non-zero for taking into account higher orders of $\boldsymbol{k}$ terms in the spin current formation.

Equation (53) shows the direct connection between the spin current and the total Zeeman splitting, $j_Z \propto E_Z$, described by Eq. (52). This explains the strong dependence of the current on the temperature and its sign reversal. While at high T only the intrinsic Zeeman splitting contributes to the current formation and results in a positive slope of the photocurrent, shown in Figs. 29 and 30(a), at low T the contribution of the giant Zeeman splitting increases and overcomes the intrinsic one, leading to a change in sign. This interplay between the first and the second term on the right hand side of Eq. (52) is not only affected by the lattice temperature, but as well by the radiation induced heating of the Mn spin system, see Fig. 30(b).

So far, the intrinsic and exchange contributions to the current can explain the experimental results qualitatively, but not quantitatively. A significant difference between the data obtained from photocurrent and PL measurements is, how strong the temperature influences the measurable value, which is in

both cases affected by the exchange enhanced E_Z in DMS. For instance, the PL data of DMS sample B at $B = 3\,\mathrm{T}$, shows that the spin splitting in the presence of Mn^{2+} increases from $-0.25\,\mathrm{meV}$, given by the intrinsic value by $g_e\mu_B B$, to $2.6\,\mathrm{meV}$ at 4.2 K by a factor of about 10. In contrast to this, the magnitude of the photocurrent at $T = 4.2\,\mathrm{K}$ is by a factor of about 40 larger than the intrinsic one obtained at $T = 22\,\mathrm{K}$, see Fig. 30. To explain the observed strong enhancement of the photocurrents, a further contribution has to be taken into account besides the giant Zeeman splitting. It is ascribed to the well known spin-dependent electron scattering by polarized Mn spins [40], which is specific for DMS.

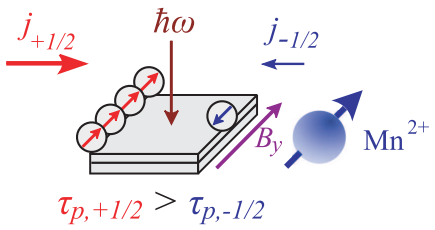

Figure 33: Scattering rates of spin-up and spin-down electrons influenced by Mn spins polarized in an external magnetic field. It results in different momentum relaxation times $\tau_{p,+1/2}$ and $\tau_{p,-1/2}$ in the two spin subbands.

This term is similar to Eq. (20), discussed in Section 2.5.2, and arises from Mn spins polarized in an external magnetic field influencing the scattering rates of spin-up and spin-down electrons [55]. It results in different momentum relaxation times $\tau_{p,+1/2}$ and $\tau_{p,-1/2}$ in the two spin subbands, shown in Fig. 33. Due to the proportionality of $\tau_{p,\pm1/2}$ and the electron fluxes $\boldsymbol{i}_{\pm1/2}$ the polarization of Mn spins adds an extra contribution to the conversion of a spin current into an electric current, denoted by $\boldsymbol{j}_{Sc}$ below. The theoretical calculation of $\boldsymbol{j}_{Sc}$ takes into account the momentum relaxation of the electrons via their interaction with the Mn^{2+} ions located within the QW and is described by the corresponding Hamiltonian given by [40]

$$H_{\text{e-Mn}} = \sum_i \left[u - \alpha\,(\boldsymbol{S}_i \cdot \boldsymbol{\sigma})\right] \delta(\boldsymbol{r} - \boldsymbol{R}_i)\,. \tag{55}$$

Here i is the Mn ion index, $\boldsymbol{S}_i$ the vector composed of the matrices of the angular momentum 5/2, $u\delta(\boldsymbol{r}-\boldsymbol{R}_i)$ the scattering potential without exchange interaction, $\boldsymbol{r}$ the electron coordinate, and $\boldsymbol{R}_i$ the Mn ion position. Usually the electron scattering by the Mn potential, characterized by u, is stronger than the exchange scattering described by α, known from the giant Zeeman splitting in Eq. (52). For the case of $|\alpha| \ll |u|$ the scattering induced current $\boldsymbol{j}_{Sc}$ reads as follows

$$\boldsymbol{j}_{Sc} = 4e\frac{\alpha}{u}\,\boldsymbol{J}_s S_{\mathrm{Mn}}\,, \tag{56}$$

where S_{Mn} is the average Mn spin along $\boldsymbol{B}$ (see [74]).

This term adds up to $\boldsymbol{j}_Z$ at low temperatures, because the average electron spin caused by the giant Zeeman effect is aligned parallel to $\boldsymbol{S}_{\mathrm{Mn}}$ and then the photocurrent is given by the sum of both contributions $\boldsymbol{j} = \boldsymbol{j}_Z + \boldsymbol{j}_{Sc}$. The strength of the observed electric photocurrent can be explained by means of this additional and very effective scattering induced contribution, which does not influence the PL measurements. In DMS a fully spin polarized electron gas due to the Zeeman effect can be realized at reasonable low magnetic fields. In this case the electron flow in one spin subband vanishes and the electric current becomes independent of the magnetic field strength and carrier statistics. It is then given by $\boldsymbol{j} = \mp 2e\boldsymbol{J}_s$, where $\mp$ corresponds to $\pm$ sign of the Zeeman splitting. Experimentally, this situation was not observed, because $\varepsilon_Z < \varepsilon_F$.

In the experiment a shift of the zero point in the temperature dependence was observed relative to the data obtained from the PL data. This shift of about 20 K was attributed mostly to the heating of the Mn system due to the radiation, which directly affects T_{Mn} and thus reduces the effect of the exchange interaction. However, to this shift the orbital MPGE may also have a minor contribution and thus will be discussed briefly. This spin-independent mechanism is based on the influence of the magnetic field on the electron scattering [70]. It emerges for example from impurities or interfaces in quantum wells and can contribute to the MPGE, because it shows almost the same dependence on the magnetic field $\boldsymbol{B}$ [70]. The strength of the spin independent contribution increases strongly in systems with a weak or vanishingly small spin-orbit coupling. The effect itself is described taking into account

the Lorentz force which acts on a heated electron gas in the presence of a magnetic field. The force acting on carriers propagating in opposite directions modifies their wave functions differently, resulting in a diamagnetic contribution, shown in Fig. 34. Hence, the applied in-plane magnetic field yields an

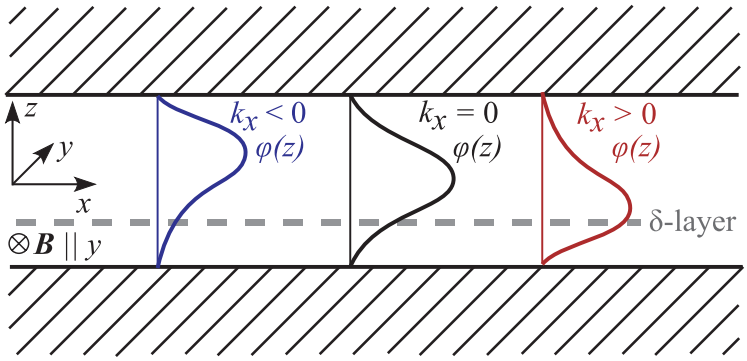

Figure 34: Quantum well with an built-in asymmetry due to the non-symmetric δ-layer (dotted line). The in-plane magnetic field B_y induces the Lorentz force on moving particles, which pushes the electrons with positive and negative velocities k_x to the lower and upper interface, respectively. This results in different scattering rates for both directions.

additional asymmetric term to the scattering matrix element, which is linear in wave vector $\boldsymbol{k}$ and magnetic field $\boldsymbol{B}$. This diamagnetic contribution leads to a photocurrent in the case of free-carrier absorption as well as in the energy relaxation of hot carriers. Therefore, this effect can superimpose the photocurrent generated by the spin dependent mechanism, which shows a similar behavior on $\boldsymbol{B}$, but the orbital mechanism independent of the g^*-factor.

5.3 Summary

This work demonstrates that in low dimensional diluted magnetic semiconductors electron gas heating generates pure spin currents and results in the zero-bias spin separation. An applied magnetic field transforms the pure spin current into an electric current. It has been shown theoretically and experimentally that this conversion is amplified by the carrier exchange interaction with the localized magnetic ions. Besides the giant Zeeman splitting of the

conduction band states, a new conversion mechanism of pure spin currents into an electric current appears due to the spin-dependent carrier scattering from localized Mn^{2+} spins polarized by an external magnetic field. In the case of a degenerate electron gas and weak magnetic fields the scattering mechanism dominates the current conversion. In addition care has to be taken to avoid high radiation power, as this introduces a heating of Manganese and thus strongly influences the giant Zeeman splitting.

6 Photocurrents in lateral structured samples

In the previous chapters it was demonstrated that photogalvanic effects strongly depend on the symmetry of the investigated sample and reflect the contributions of BIA and SIA. Here it will be shown that semiconductor heterostructures with a one dimensional lateral potential excited by THz radiation emerge a new root to the generation of photocurrents. They allow a controllably variation of the symmetry by changing the pattern parameters. The resulting influence of this one dimensional potential can be seen in transport properties [75, 76]. Moreover they may give rise to an additional access to the formation of spin photocurrents. Thus the experiments were aimed to investigate mainly magnetic field dependent effects. However, in contrast to the reference samples a huge photocurrent at zero magnetic field was observed in the lateral structured samples, yielding exciting new results. The generation of the photocurrent is due to a modulation of the local electron gas temperature. It results from a combined action of a spatially periodic in-plane potential and a spatially modulated light, known as the Seebeck ratchet effect [77]. The observed photocurrent consists of a polarization independent and dependent part, for which a microscopic mechanism to interpret the experimental findings is proposed [59, 60]. Both the phenomenological and microscopic description of these effects have been suggested and extended to the case of polarized radiation by Prof. Ivchenko in parallel to the experiments. Furthermore, the effect of an external magnetic field on the photocurrent formation is probed, as this is allowed to yield additional contributions to the MPGE in (001)-grown structures.

6.1 Magnetic field independent photocurrents

6.1.1 Photocurrent experiment

The photocurrents were generated in the samples, described in Section 3.4.3, applying free carrier absorption of THz radiation of a pulsed NH_3 laser operating at a wavelength $\lambda = 280\,\mu m$ with a maximum power $P \simeq 2\,kW$ and pulse duration $t_s \approx 100\,ns$ [43]. Via the voltage drop across a $50\,\Omega$ resistor the

photoresponse of the sample, picked up along a pair of ohmic contacts centered on opposite sample edges (Fig. 35), was recorded with a storage oscilloscope. The samples were measured under normal and oblique incidence, in which θ_0 describes the angle of radiation incidence in respect to the sample normal, varied from $-35°$ to $+35°$. By means of a $\lambda/4$-plate the initially linearly polarized radiation was transformed into circularly polarized radiation according to $P_{\rm circ} = \sin 2\varphi$, where φ is the angle between the initial polarization plane and plates c-axis.

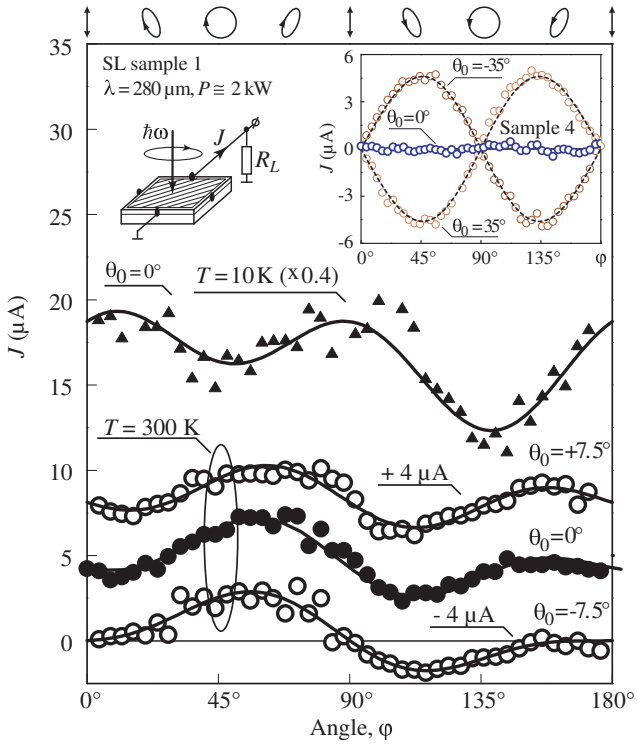

Figure 35: Photocurrent as function of the angle φ measured in SL sample 1. Full lines are fits to Eq. (57). Insets show the experimental geometry (left) and $J(\varphi)$ in the reference sample 4 (right). Doted lines are fits to $J = A_{\rm ref} \sin\theta_0 \sin 2\varphi$. The ellipses on top illustrate the polarization for various angles φ.

In Fig. 35 the photocurrent observed in SL sample 1 (slits along <010> direction) is plotted as a function of the angle φ for $T = 300$ K and 10 K. The signal emerges a dependence on the helicity and on the linear polarization, as well

as it shows a polarization independent offset for normal and oblique incidence. In the inset of Fig. 35 the photocurrent of the reference sample 4 is shown. Here, a helicity dependent signal is observed only for oblique incidence. In both samples the room temperature data were obtained for various angles θ_0 and are presented with their corresponding fit parameters in the discussion of the experimental results, see Fig. 38. For the SL samples 2 and 3, both with slits along the crystallographic axes <110>, a similar behavior was observed for the α and φ dependences. The data are not shown, as the discussion is mainly focused on SL sample 1 and reference sample 4.

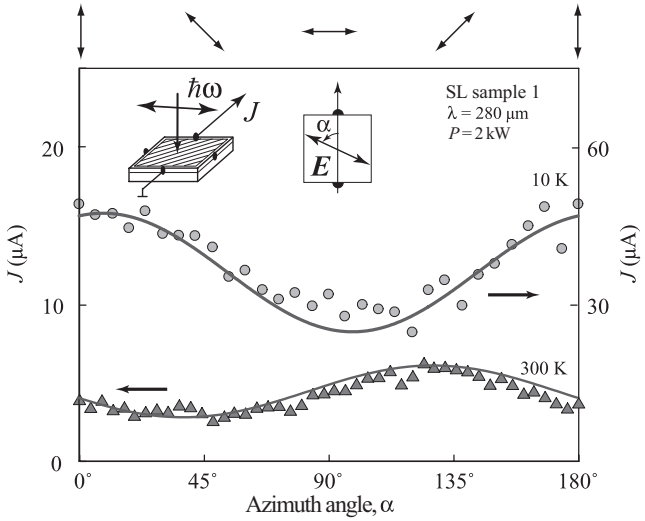

Figure 36: Photocurrent as function of the angle α measured in SL sample 1 for $T = 300$ K and 10 K. Full lines are fits to Eq. (58). Insets show the experimental geometry (left). The top middle inset shows the rotation of the linear polarization by a $\lambda/2$-plate.

Figure 36 shows the photocurrent in dependence of the azimuth angle α obtained by the rotation of a $\lambda/2$-plate. The presented data was obtained in SL sample 1 for $T = 300$ K and 10 K.

6.1.2 Discussion

In two-dimensional electron systems (2DES) like the investigated (001)-grown GaAs QWs, the illumination with THz radiation can lead to the generation

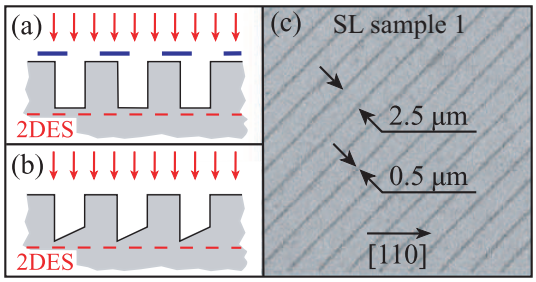

Figure 37: Sample design. (a) Blanter and Büttiker's geometry. (b) Our experimental geometry. (c) Electron micrograph.

of a current, whose strength and direction depend on the symmetry of the system, as well as on the experimental geometry and the light's polarization state [3, 43]. Similarly in nonequilibrium spatially-periodic noncentrosymmetric systems, like a sawtooth potential, a transport of particles is even possible in the absence on an average macroscopic force. Such a directed transport due to the interaction of an asymmetric potential and an oscillating *ac* force is known as ratchet effect and plays an important role in different fields of physics [77–85]. For the case this effect emerges as a result of an applied electro-magnetic radiation, it belongs to the group of the photogalvanic effects [86–88].

A situation, which directly links photogalvanic and ratchet effects, exhibits if a lateral superlattice is superimposed upon a 2DES and is irradiated by THz radiation. Here the light is shining through a periodic grating and drives an additional current through the modulated 2DES. This example represents a novel ratchet effect, which was considered in a similar way and investigated theoretically by Blanter and Büttiker [89, 90]. In their work it has been shown that the irradiation of a lateral SL through a mask with slits, but both with the same period, results in a *dc* carrier flow due to a local electron gas heating, only for the case the SL is shifted in phase with respect to the mask. In the system realized in the experiment, the mask is replaced by a one-dimensional array of grooves, introduced in the top cap of a semiconductor heterostructure via an etching process. These periodic grooves on the one hand modulate the intensity of the incident light field due to near field diffraction, which is spatially periodic in the plane of the 2DES [43] and therefore, leads to a periodic modulation of

the effective electron temperature. On the other hand they generate a weak one-dimensional periodic potential, which is superimposed upon the 2DES. Due to the fact that this ratchet effect results from a spatial modulation of the temperature, it is called a Seebeck ratchet [77]. The necessary relative phase shift between the mask and the periodic potential in the geometry of Blanter and Büttiker was introduced by an asymmetry of the grooves, allowing a directed carrier flow. In Figs. 37(a) and (b) both geometries are compared. The phase shift between the mask and the SL in Fig. 37(a) has the same effect as the asymmetric profile of the grating in Fig. 37(b) as both result in a phase shift of the spatially periodic near field intensity with respect to the periodic potential acting on the 2DES. In the following a is used for the period of the SL and the axis perpendicular and parallel to the grating are labelled as x and y, respectively. According to this notation the function describing the potential of the SL, $V(x+a) = V(x)$, is periodic in x and independent on y.

While the above described photothermal ratchet effect emerges a large photocurrent for unpolarized radiation at normal incidence, in the experiment two additional photocurrent contributions, excited by linearly and circularly polarized radiation, have been observed. The theoretical analysis is based on the theory of Refs. [89, 90] and was extended by Prof. Ivchenko parallel to the experiments to the case of polarized radiation. Additionally this expansion allows to propose new mechanisms of the observed circular and linear photogalvanic effect in the presence of the combined action of an out-of-phase periodic potential and in-plane modulated pumping of the 2DES.

The experimentally observed photocurrent in SL sample 1 is maximal for $\theta_0 = 0°$ (Fig. 35). In contrast the signal vanishes for the unpatterned reference sample 4, see inset of Fig. 35. The dependence in the reference sample under oblique incidence can be fitted after $J = A_{\mathrm{ref}} \sin\theta_0 \sin 2\varphi$, which stems from the circular photogalvanic effect (CPGE) and is allowed in (001)-grown GaAs QW structures, belonging to the C_{2v} symmetry. The photocurrent in the SL sample, however, shows a more complex behavior, described by

$$J = A \sin 2\varphi + B \sin 4\varphi + C \cos 4\varphi + D \,, \tag{57}$$

where A, B, C, and D are fitting parameters. The application of Eq. (57) to the experimental results obtained from the reference sample 4 yields that the fit parameters B, C, $D \approx 0$, whereas the parameter A is nonzero for $\theta_0 \neq 0°$.

Similar to this the rotation of a $\lambda/2$-plate results in a rotation of the linearly polarized radiation and yields an directed dc current in SL sample 1. It can be described in terms of the coefficients entering Eq. (57), by

$$J = 2B \sin 2\alpha + 2C \cos 2\alpha + D - C \,, \tag{58}$$

where α is the azimuth angle assigning the plane of polarization. The last part, $D - C$, of Eq. (58) constitutes the polarization independent ratchet effect proposed in [89, 90]. This is due to the fact, that the C-portion of the current takes into account the ratchet contributions from linearly polarized light, described by the term $2C \cos 2\alpha$, and has to be subtracted to get the current driven solely by unpolarized radiation. The dependence of the current on the azimuth angle α was checked experimentally and is well fitted by this equation, shown in Fig. 36 for $T = 300$ K and 10 K. The photogalvanic currents, which depend on linearly polarized radiation were not observed in the reference sample 4 and in correspondence to the previous results for Eq. (58) the fit parameters B, C, $D \approx 0$.

A similar behavior was observed in all SL samples and can be described phenomenologically by symmetry arguments. Additionally, the magnitude of the photocurrent at $\theta_0 = 0°$ detected in SL sample 1 with an orientation of the grooves along $\langle 010 \rangle$ exceeds the one observed in the reference sample even at large angles of incidence ($\theta_0 = \pm 30°$). These helicity dependent signals, described after Eq. (57) and (58), have been found in a wide temperature range from 300 K to 10 K. For the latter case (T=10 K) the corresponding trace is included in Fig. 35 and 38 and demonstrates that the photocurrent increases with decreasing temperature. In the following the measurements are limited to room temperature data, because the presented microscopic theory is only valid for elevated temperatures. The grooves in the SL samples 2 and 3 are, in contrast to SL sample 1, oriented along the $\langle 110 \rangle$ directions. Here, the observed photocurrents at normal incidence of radiation are one order of magnitude smaller compared to the one detected in SL sample 1. This result reflects the

strong influence of the grooves profile shape, being strongly asymmetric in SL sample 1 and almost symmetric in SL samples 2 and 3. The extracted fit parameters of SL sample 1 and and reference sample 4 are plotted in Fig. 38 according to Eq. (57) against the angle of incidence θ_0.

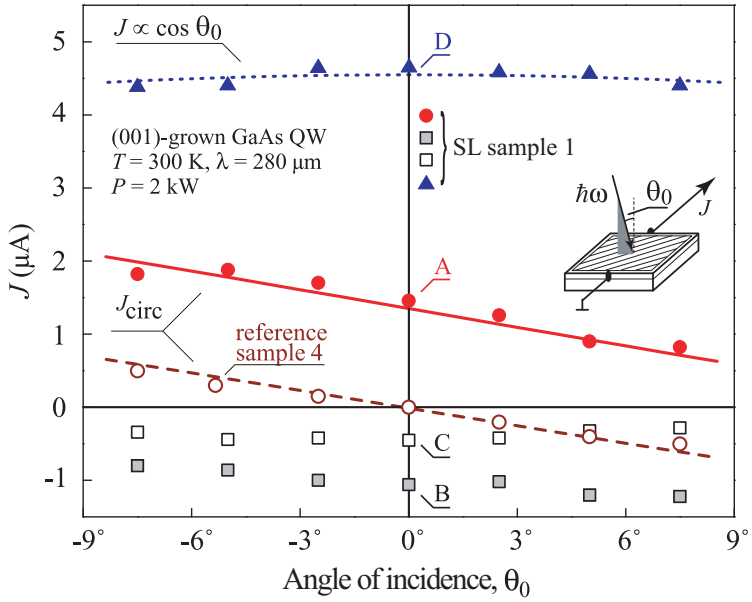

Figure 38: Angle of incidence dependence of the photocurrent. • and ∘: J_{circ} measured in SL sample 1 and reference sample 4, respectively. The different symbols represent the current contributions proportional to B, C and D. Dotted line is the fit after $J = D\cos\theta_0$. Solid and dashed lines are fits to $J \propto (A_{\mathrm{ref}}\sin\theta_0 + A\cos\theta_0)$.

6.1.3 Phenomenological explanation

The phenomenological theory according to the point-group symmetry C_{2v} to which the unpatterned QWs belong excludes all in-plane photocurrents under normal incidence [43, 91]. This corresponds to the experimental observations in the reference sample 4 at $\theta_0 = 0°$ (see inset in Fig. 35)). In the case an unpatterned QW is superimposed by an asymmetric SL its C_{2v} symmetry is overwritten by the potential's C_s point group symmetry. This reduction of the symmetry gives rise to photocurrents induced under normal-incidence

excitation along and normal to the grooves. Phenomenologically the currents are described by

$$\begin{aligned} j_x &= I[\chi_1 + \chi_2(|e_x|^2 - |e_y|^2)] \,, \\ j_y &= I\chi_3(e_x e_y^* + e_y e_x^*) + I\gamma P_{\mathrm{circ}} \,, \end{aligned} \tag{59}$$

where e_x, e_y are the components of the light's polarization unit vector $\boldsymbol{e}$, I is the light intensity, χ_{1-3} and γ are phenomenological parameters. For SL sample 1, in which the current is measured under an angle of 45° with respect to the SL axis x and y (see inset of Fig. 35), the photocurrent J at $\theta_0 = 0°$ consists of a superposition of the currents j_x and j_y of Eq.(59). If the initial polarization of the laser beam is aligned parallel to the direction the signal is picked up in the experiment, then the terms in Eqs. (59) transform according to the rotation of the $\lambda/4$-plate to $(|e_x|^2 - |e_y|^2) = -\sin 4\varphi/2$ and $(e_x e_y^* + e_y e_x^*) = (1 + \cos 4\varphi)/2$. The superposition of j_x and j_y reduces Eqs. (59) to Eq. (57) with the coefficients $A = \gamma/\sqrt{2}$, $B = -\chi_2/2\sqrt{2}$, $C = \chi_3/2\sqrt{2}$, $D = C + \chi_1/\sqrt{2}$. For the rotation of the $\lambda/2$-plate the terms $(|e_x|^2 - |e_y|^2)$ and $(e_x e_y^* + e_y e_x^*)$ are equal to $-\sin 2\alpha$ and $\cos 2\alpha$, respectively. Here Eqs. (59) reduce to Eq. (58), in which the helicity dependent part is absent, accordingly.

The fit after Eq. (57) of the signals at different angles θ_0 (shown in Fig. 35) which constitute from a superposition of Eq. (59), yields the dependence of the photocurrent coefficients A, B, C and D on the angle of incidence, plotted in Fig. 38. A very significant contribution is the large dominating value of D, which as well as B and C only weakly depends on θ_0. It reaches its maximum at normal incidence and can be well fitted by $J \propto \cos\theta_0$. The contributions given by the coefficients B and C, describing the dependence of the photocurrent on linearly polarized radiation, are substantially smaller than D.

In the following the helicity dependent contributions of both the patterned sample 1 and the reference sample 4 under illumination with circularly polarized light are compared. The signal from the reference sample stems from the circular photogalvanic effect. A characteristic feature of this photon helicity dependent current is the change in sign upon switching the radiation helicity. While taking the difference of the photocurrents, induced by right- and left-handed, the other terms in Eq. (57) remain unchanged. As a result

of this the contribution A can be extracted from the total current by $J_{\mathrm{circ}} = [J(\varphi = 45°) - J(\varphi = 135°)]/2$. From Fig. 38 it is easy to see that J_{circ} in SL sample 1 consists of two contributions $(A_{\mathrm{ref}} \sin\theta_0 + A\cos\theta_0)$. The first term, which is proportional to A_{ref}, emerges from the host material and is the same as in the reference sample. Whereas the second term presents a new contribution originating from the lateral pattern.

6.1.4 Microscopic origin of the photocurrent

In the following the microscopic origin of the observed photocurrents at normal incidence will be discussed as well as the microscopic expressions for the relevant parameters χ_1 and γ, limited to the case of unpolarized and circularly polarized light, respectively. The analysis of these two contributions to the ratchet effects is crucial for the understanding of the data summarized in Fig. 38. For this the classical Boltzmann equation for the electron distribution function $f_{\boldsymbol{k}}$,

$$\left(\frac{\partial}{\partial t} + v_{\boldsymbol{k},x}\frac{\partial}{\partial x} + \frac{\boldsymbol{F}}{\hbar}\frac{\partial}{\partial \boldsymbol{k}}\right) f_{\boldsymbol{k}}(x) + Q_{\boldsymbol{k}}^{(p)} + Q_k^{(\varepsilon)} = 0\,, \tag{60}$$

has to be taken into account. Here $\boldsymbol{k}$ is the in-plane electron wave vector, $\boldsymbol{F}$ the sum of the time-dependent electric-field force $e\boldsymbol{E}(t) = 2e\,\mathrm{Re}[\boldsymbol{E}_0 \exp(-\mathrm{i}\omega t)]$ of the light wave and the static force $-dV(x)/dx$, ω the light frequency, $\boldsymbol{v}_{\boldsymbol{k}} = \hbar\boldsymbol{k}/m^*$ the electron velocity, e and m^* the electron charge and effective mass, $Q_{\boldsymbol{k}}^{(p)}$ and $Q_k^{(\varepsilon)}$ the collision terms responsible for the electron momentum and energy relaxation, respectively. The operator $Q_{\boldsymbol{k}}^{(p)}$ is taken in its simplest form $(f_{\boldsymbol{k}} - \langle f_{\boldsymbol{k}}\rangle)/\tau$, where τ is the momentum relaxation time and the brackets imply an averaging over $\boldsymbol{k}$ directions. The operator $Q_k^{(\varepsilon)}$ acts on the distribution function averaged over the directions of $\boldsymbol{k}$ and depends only on the modulus $k = |\boldsymbol{k}|$. The assumptions for Eq. (60) are only valid for a weak and smooth potential, which satisfies the conditions $|V(x)| \ll \varepsilon_e$ and $q \equiv 2\pi/a \ll k_e$, where k_e is the typical electron wave vector and ε_e the typical energy assumed to be larger than the photon energy $\hbar\omega$.

6.1.4.1 Polarization-independent photocurrent: The photocurrent contribution, which constitutes the polarization-independent ratchet effect, is given by

the term including χ_1 in Eqs. (59) and describes the photocurrent proportional to $D - C = \chi_1/\sqrt{2}$ in Eq. (58). It can be related to the heating of free carriers by an electromagnetic wave. In the case of high temperatures the kinetic Eq. (60) can be reduced to the macroscopic equations for the two-dimensional electron density $N(x)$, local nonequilibrium temperature $\Theta(x)$, current density j_x and energy flux density $i_{\varepsilon,x}(x)$ in x-direction. Under homogeneous optical excitation these equations have the solutions, given by

$$\begin{aligned} k_B\Theta &= k_BT + \hbar\omega G\tau_\varepsilon \,, \\ N(x) &\equiv N(x,\Theta) = N_0 \mathrm{e}^{-V(x)/k_B\Theta} \,, \end{aligned} \tag{61}$$

where G is the Drude absorption rate per particle, and N_0 is x-independent. For the general solution, shown in Eqs. (61), the current j_x, and thus the carrier flow $i_{\varepsilon,x}$, are absent. Only if the generation rate G varies spatially, a nonzero j_x arises. Such an inhomogeneous distribution of the radiation electric field is generated in the patterned samples due to near field effects, which occur because the distance between the surface pattern and the QW is smaller than the wavelength [43]. Resulting from this, the amplitude of a plane electromagnetic field shining through the superimposed grating becomes a periodic function of x with the period a. In addition an asymmetrical SL leads to a relative phase shift between the potential $V(x)$ and the light intensity $I(x)$, yielding a net current even for unpolarized radiation because in this case the product $I(x)(dV/dx)$ averaged over the space does not vanish. This spatial variation of G is described by the steady-state generation $G(x) = G_0 + G_1\cos(qx + \varphi_G)$, which produces a stationary periodic electron temperature $\Theta(x) - \overline{\Theta} \equiv \delta\Theta(x) = \tau_\varepsilon\hbar\omega[G(x) - G_0]$ accompanied by a light-induced periodic correction of the space-oscillating contribution to the electron density $\delta N(x) \approx -N_0\delta\Theta(x)/\overline{\Theta}$. Microscopically the current is described by a sum of drift and diffusion terms,

$$j_x = \mu\left\{N(x)\frac{dV(x)}{dx} + \frac{d}{dx}[k_B\Theta(x)N(x)]\right\} \,, \tag{62}$$

where $\mu = |e|\tau/m^*$ is the electron mobility . Both terms in Eq. (62) depend on x, whereas the total j_x is x-independent. As the diffusion term averaged

over a period d vanishes and the average of the product $N(x,\overline{\Theta})dV(x)/dx$ is zero the current can be calculated as an average $\mu\overline{[dV(x)/dx]\delta N(x)}$.

The lateral potential can be modeled in the simple and periodic in x function $V(x) = V_1 \cos(qx + \varphi_V)$. Due to a phase shift between $V(x)$ and the periodic electron temperature $\Theta(x)$ a current along x, given by Eq. (63), arises.

$$j_x = \chi_1 I = \mu N_0 \hbar q \zeta' G_0 \frac{V_1}{2k_B T} \omega\tau_\varepsilon \tag{63}$$

In this equation the asymmetry parameter $\zeta' = (G_1/G_0)\sin(\varphi_V - \varphi_G)$, describing the inhomogeneous photoexcitation, enters. For the derivation leading to Eq. (63) a model function $V(x)$ was used, which is similar to the one considered in Ref. [90] and is applicable to ratchets with a phase shift between its sinusoidal potential and the temperature variation. Generally, such nonequilibrium asymmetric systems based on a periodic potential $V(x)$ and a periodic temperature profile $\Theta(x)$ are referred to as Seebeck ratchets [77]. As an important result Eq. (63) yields a polarization independent current, which increases with decreasing temperature T, as observed in the experiment (see Fig. 35) and is proportional to the energy relaxation time τ_ε.

6.1.4.2 Helicity-dependent photocurrent: The helicity-dependent photocurrent which is described in Eqs. (59) by the parameter γ or in Eq. (57) by A, is driven by circularly polarized light and is therefore, called circular ratchet effect. Similar to the polarization-independent part this contribution is generated in a lateral SL with a phase shift between the periodic potential $V(x)$ and the generation rate $G(x)$. A photocurrent, which depends on the helicity at normal incidence of radiation ($\theta_0 = 0°$) is allowed by symmetry arguments, but only along the y-direction. Circularly polarized radiation excludes the χ_3-term in Eqs. (59), by which the remaining current is given by $j_y = \pm I\gamma$, with $\pm$ corresponding to right- and left-handed circular polarized radiation, respectively. More precisely, the resulting photocurrent along the direction of grooves reads

$$j_y = \frac{2e^2\tau}{m^*} \mathrm{Re}\{\overline{E^*_{0y}(x)\delta N_\omega(x)}\}\,, \tag{64}$$

where $\delta N_\omega(x)$ is the electron density oscillation linear in the THz electric field E_{0x}. Considering the continuity equation $-\mathrm{i}\omega e\delta N_\omega + dj_{x,\omega}/dx = 0$ and the

equation for the linear-response electric current $j_{x,\omega}(x)$ modulated in space the circular photocurrent is described by

$$\gamma = \frac{\pi e^2}{\hbar c n_\omega} \zeta' \mu N_0 \frac{\hbar q}{m^*} \frac{\tau}{\omega(1+\omega^2\tau^2)} \frac{V_1}{k_B T} \,. \tag{65}$$

This kind of directed current, which changes its sign upon switching the light helicity and thus is proportional to the circular polarization P_{circ}, is based on two phase shifts relative to the periodic variation $\delta N(x,t)$. One of them is a spatial phase shift between the potential $V(x)$ and generation rate $G(x)$, proportional to $\varphi_V - \varphi_G$. The second one is a temporal phase shift, given by $\arctan(\omega\tau)$ with respect to $E_x(t)$. In comparison to the polarization-independent the helicity-dependent current is by a factor of $2\omega\tau_\varepsilon$ smaller but increases in the same way with decreasing T, also confirmed by the experiment. Here the current is proportional to the momentum relaxation time τ.

6.2 Magnetic field dependent photocurrents

6.2.1 Photocurrent Experiments

For the measurements of the magnetic field dependent and independent photocurrents the same experimental setup was used as described in Section 6.1.1. The magnetic field $\boldsymbol{B} = \pm 0.7$ T was applied along the x-axis of the sample. All experiments were carried out on SL sample 5, prepared with grooves along the y-direction, see inset of Fig 39. The lateral potential, shown in the upper inset of Fig. 39, differs from the one superlattice of SL samples 1 to 3 but allows a controllable variation of the asymmetry, described in Chapter 3.4.3.

Figure 39 shows the photocurrent J_x parallel to the magnetic field in dependence of the angle φ at $T = 300$ K for $B_x = \pm 0.7$ T and 0 T. While for $\boldsymbol{B} \neq 0$ the current shows a strong polarization dependence, for $\boldsymbol{B} = 0$ only a polarization independent signal was observed. The corresponding results for J_y are presented in Fig. 40. In this direction the signal vanishes completely for the case $\boldsymbol{B} = 0$.

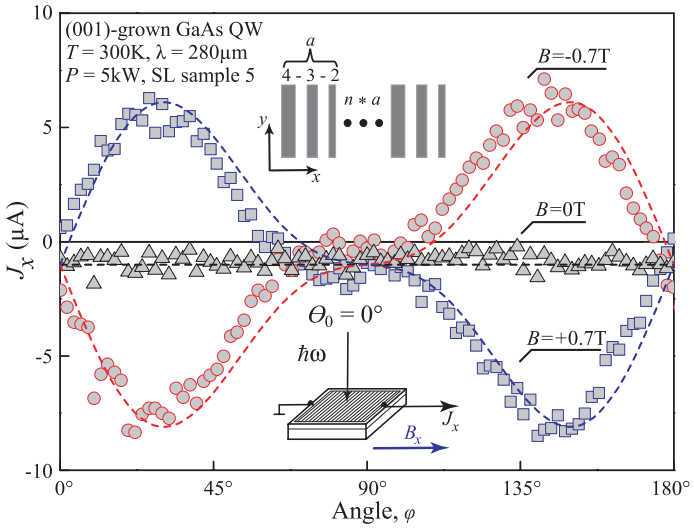

Figure 39: Photocurrent along the x-axis as a function of the angle φ measured in SL sample 5 at $\theta_0 = 0°$ for $B_x = \pm 0.7$ T and 0 T. Full lines are fits to Eq. (66). Insets show the experimental geometry (bottom) and the geometry of the grooves etched in the top of the sample.

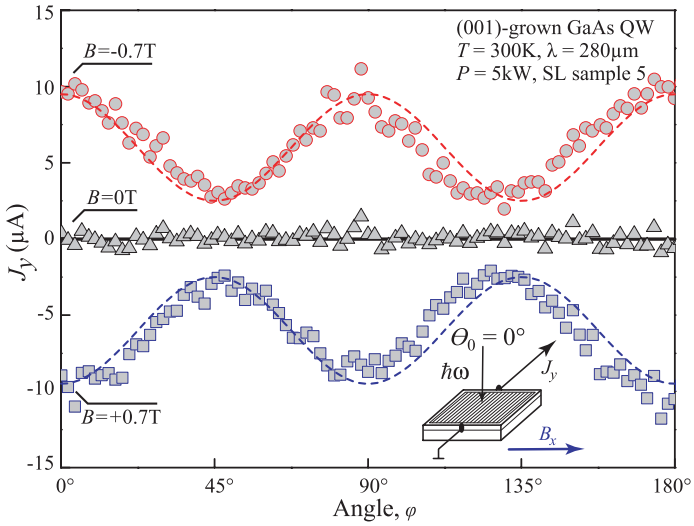

Figure 40: Photocurrent along the y-axis as a function of the angle φ measured in SL sample 5 at $\theta_0 = 0°$ for $B_x = \pm 0.7$ T and 0 T. Full lines are fits to Eq. (67). The inset shows the experimental geometry.

6.2.2 Discussion

In contrast to SL sample 1, in SL sample 5 a current under normal incidence of radiation and without an applied magnetic field $\boldsymbol{B}$ is only observed along the x-axis, describing the SL potential $V(x)$. A superposition of j_x and j_y like in SL sample 1 is not allowed due to the fact, that the x-axis of $V(x)$ coincides with one of the mirror planes contained in the host material's C_{2v} point group. The application of Eq. (57) to fit the photocurrent J_x at $B = 0$ T obtained from the SL sample 5 yields that the fit parameters A, B, $C \approx 0$, whereas the parameter D is nonzero for $\theta_0 = 0°$. The host material does not allow photocurrents at normal incidence, due to its C_{2v} symmetry. Thus the parameter D stems from the lateral potential and represents in full correspondence with Eqs. (59) the polarization independent contribution χ_1, see Fig. 39. Figure 40 shows J_y, for which no signal is obtained at $B = 0$ T and thus all fit parameters are zero. The small photocurrent J_x at $B = 0$ T observed in SL sample 5, compared to SL sample 1, can be a result of the different periodicities of both superlattices in which $a_{SL5} > a_{SL1}$. As the polarization-independent (Eq.(62)) and the helicity-dependent photocurrents (Eq.(65)) depend linear on the parameter $q \equiv 2\pi/a \ll k_e$ and thus, decreases with the periodicity a, this can lead to a smaller signal in SL sample 5.

The situation changes under application of an external magnetic field $\boldsymbol{B}$ aligned along the x-axis. While J_x and J_y for $B = 0$ T did not depend on the variation of the angle φ the currents now reveal additional polarization independent and dependent contributions. Both J_x and J_y show a linear in $\boldsymbol{B}$ photocurrent for $B_x = \pm 0.7$ T (Fig. 39 and 40, respectively) and originate from the MPGE, which was already discussed in Sections 2.3.1 and 4.2.1. Its magnitude is by a factor of about 8 higher compared to the one observed at $B = 0$ T. The dependence on the angel φ can be described taking into account Eqs. (6) and (7) together with Eqs. (41) to (43), leading to the following equations

$$j_x/I = A' B_x \sin 2\varphi + B' B_x \sin 4\varphi, \tag{66}$$

$$j_y/I = D' B_x + C'_2 B_x (1 + \cos 4\varphi), \tag{67}$$

where A', B', C' and D' are fitting parameters.

6.3 Summary

The lateral grating, which is etched into the surface of the sample induces a periodic lateral potential acting on the 2DES. As a result the grating modulates the incident radiation in the near field and emerges polarization-independent, circular and linear ratchet effects in the plane of the 2DES. For an asymmetric lateral SL the product of the static force $-dV(x)/dx$ and the photothermal modulation of the electron density $\delta N(x)$ is nonzero, if it is averaged over the space. This effect causes the flow of a stationary current and was predicted for the case of unpolarized light in Ref. [90]. In addition to this contribution a helicity-dependent photocurrent was observed resulting from a phase shift between the periodic potential and the periodic light field. Another difference among both currents is their dependence on the relaxation time. While the polarization-independent one is governed by the energy relaxation time, the helicity-dependent is controlled by the momentum relaxation time only. The observed magnetic field depended photocurrents in the samples with a lateral SL may give an additional access to further investigations of ratchet effects. While the appearance of these current is clearly demonstrated and confirms the phenomenological equations for the MPGE, the understanding of magnetic field induced effect modified by the lateral potential and its microscopic origin is a task for the future.

7 Conclusion

To summarize, in this work spin polarized currents were observed and studied in various low dimensional semiconductor systems under excitation with THz radiation. The measurements demonstrate that the microscopic origin of the photocurrents is the asymmetric spin-dependent scattering, which results in a spatial separation of electrons with opposite spins. During the spin separation a spin current flows, which is transformed into a net electric current by the application of an external magnetic field. This effect, known as the MPGE, was observed in different types of low dimensional GaAs structures and DMS (CdMn)Te QWs. Besides the fundamental question on the origin of the spin current formation, the variation of the inversion asymmetry in low dimensional systems, which is of particular interest for spintronics related research, was studied. To achieve this goal spin polarized currents, as an experimental access to the inversion asymmetry, have been utilized.

In the first part of this work, the MPGE has been observed in (110)-grown GaAs heterostructures. The phenomenological equations as well as the microscopic pictures developed to describe the zero-bias spin separation and the MPGE in (001)-grown GaAs QW structures have been extended in parallel to this work to describe the effects in heterostructures grown along the (110)-direction. The corresponding dependences on the light's polarization, magnetic field and temperature prove the spin-dependent origin of these two effects. Here, it has been shown that the MPGE provides a versatile tool to probe the symmetry of (110)-grown quantum wells at room temperature. The photocurrent in the presence of an in-plane magnetic field is only observed for asymmetric structures, but vanishes for symmetric QWs. By means of time-resolved Kerr rotation it has been independently confirmed that in the latter case the spin relaxation time is maximal and therefore, these structures set the upper limit of spin dephasing in GaAs QWs. In addition, it was demonstrated that the structure inversion asymmetry can be controllably tuned to zero by the variation of the δ-doping layer positions. Furthermore, the results prove that in (110)-grown GaAs heterostructures the segregation of doping impurities is suppressed due to a lower growth temperature, allowing to grow structures with zero SIA [19, 31]. These results of the MPGE are addition-

ally supported by experiments with (001)-grown QWs showing that a reduced doping temperature suppresses segregation processes, shown in [32].

The second part was aimed to the observation and detailed study of the zero-bias spin separation and the MPGE in diluted magnetic semiconductors based on (001)-grown CdTe doped with Mn^{2+} ions. The spin current, generated by electron gas heating under terahertz radiation, is converted into a net electric current by the application of an external magnetic field. The experimental data show that the spin polarization of the magnetic ion system enhances this conversion process drastically. This is on the one hand, due to the Giant Zeeman splitting of the conduction band and on the other, a result of a spin-dependent electron scattering on localized Mn^{2+} ions, polarized by an external magnetic field. The latter mechanism dominates the current conversion in a degenerate electron gas at weak magnetic fields. The observed data, reflecting a strong dependence of the exchange interaction enhanced Zeeman splitting of the conduction band electrons on the temperature, intensity and concentration of Mn^{2+}, give a further evidence to the spin-dependent origin of the MPGE [20]. This question arose since the magnetic field dependent and independent effects can be obtained alternatively by orbital effects [70, 92]. These competing spin-independent effects would emerge similar results but are not affected by a change of the effective g^*-factor.

The last part of this work demonstrates that the inversion asymmetry can also be controllably varied by the preparation of lateral superlattices. While the aim of this part was to study the MPGE, surprisingly new and interesting results at zero magnetic field were obtained, which became a central subject of this chapter. These experiments allowed for the first time to demonstrate the Seebeck ratchets, predicted theoretically ten years ago. Here, the photocurrent generation is based on the combined action of a spatially periodic in-plane potential and a spatially modulated light, which gives rise to a modulation of the local temperature. Moreover, in addition to the polarization-independent current due to the Seebeck ratchet effect, a sample response on linear and circular polarized light was observed. For the helicity dependent effects a microscopic mechanism to interpret the experimental findings is proposed [59, 60]. Finally, the magnetic field induced photogalvanic effect in lateral structured samples

was observed and investigated at room temperature. The obtained results are in good agreement with the phenomenological equations, describing the MPGE in (001)-grown heterostructures.

References

[1] S.A. Wolf, D.D. Awschalom, R.A. Buhrman, J.M. Daughton, S. von Molnár, M.L. Roukes, A.Y. Chtchelkanova, and D.M. Treger, *A Spin-Based Electronics Vision for the Future*, *Science* **294**, 1488 (2001).

[2] J. Fabian, A. Matos-Abiague, C. Ertler, P. Stano, and I. Žutić, *Semiconductor Spintronics*, *Acta Phys. Slovaca* **57**, 565 (2007).

[3] E.L. Ivchenko, *Optical Spectroscopy of Semiconductor Nanostructures*. Alpha Science Int., Harrow, 2005.

[4] M.I. Dyakonov, *Spin Physics in Semiconductors*. Springer, Berlin, 2008. (ed. M. I. Dyakonov).

[5] M.I. Dyakonov and V.I. Perel, *Optical Orientation (Modern Problems in Condensed Matter Sciences)*. North-Holland Physics Publishing, Amsterdam, 1984. (ed. F. Meier and B.P. Zakharchenya).

[6] V.M. Edelstein, *Spin polarization of electrons by an electric current*, *Solid State Communications* **73**, 233 (1990).

[7] A.G. Aronov, Yu.B. Lyanda-Geller, and G.E. Pikus, *Spin polarization of conduction electrons induced by electric current in two-dimensional asymmetric electron systems*, *Sov. Phys. JETP* **73**, 537 (1991).

[8] S.D. Ganichev, S.N. Danilov, Petra Schneider, V.V. Bel'kov, L.E. Golub, W. Wegscheider, D. Weiss, and W. Prettl, *Can electric current orient spins in quantum wells?*, *arXiv: cond-mat* 0403641 (2004).

[9] S.D. Ganichev, S.N. Danilov, Petra Schneider, V.V. Bel'kov, L.E. Golub, W. Wegscheider, D. Weiss, and W. Prettl, *Electric current-induced spin orientation in quantum well structures*, *J. Magn. and Magn. Materials* **300**, 127 (2006).

[10] A.Yu. Silov, P.A. Blajnov, J.H. Wolter, R. Hey, K.H. Ploog, and N.S.Averkiev, *Current-induced spin polarization at a single heterojunction*, *Appl. Phys. Lett.* **85**, 5929 (2004).

[11] Y.K. Kato, R.C. Myers, A.C. Gossard, and D.D. Awschalom, *Current-Induced Spin Polarization in Strained Semiconductors*, *Phys. Rev. Lett.* **93**, 176601 (2004).

[12] V. Sih, R.C. Myers, Y.K. Kato, W.H. Lau, A.C. Gossard, and D.D. Awschalom, *Spatial imaging of the spin Hall effect and current-induced polarization in two-dimensional electron gases*, *Nature Phys.* **1**, 31 (2005).

[13] T. Dietl, *Handbook on Semiconductors.* North-Holland, Amsterdam, 1994. (ed. T.S. Moss).

[14] R. Winkler, *Spin-Orbit Coupling Effects in Two-Dimensional Electron and Hole Systems.* Springer, Berlin, 2003.

[15] R. Winkler, *Spin-Dependent Transport of Carriers in Semiconductors (Handbook of Magnetism and Advanced Magnetic Materials).* John Wiley & Son, New York, 2007.

[16] R.D.R. Bhat, F. Nastosv, A. Najmaie, and J.E. Sipe, *Pure Spin Current from One-Photon Absorption of Linearly Polarized Light in Noncentrosymmetric Semiconductors*, *Phys. Rev. Lett.* **94**, 096603 (2005).

[17] H. Zhao, X. Pan, A.L. Smirl, R.D.R. Bhat, A. Najmaie, J.E. Sipe, and H.M. van Driel, *Injection of ballistic pure spin currents in semiconductors by a single-color linearly polarized beam*, *Phys. Rev. B* **72**, 201302 (2005).

[18] S.D. Ganichev, V.V. Bel'kov, S.A. Tarasenko, S.N. Danilov, S. Giglberger, Ch. Hoffmann, E.L. Ivchenko, D. Weiss, W. Wegscheider, Ch. Gerl, D. Schuh, J. Stahl, J. De Boeck, G. Borghs, and W. Prettl, *Zero-bias spin separation*, *Nature Phys.* **2**, 609 (2006).

[19] V.V. Bel'kov, P. Olbrich, S.A. Tarasenko, D. Schuh, W. Wegscheider, T. Korn, C. Schüller, D. Weiss, W. Prettl, and S.D. Ganichev, *Symmetry and Spin Dephasing in (110)-Grown Quantum Wells*, *Phys. Rev. Lett.* **100**, 176806 (2008).

[20] S.D. Ganichev, S.A. Tarasenko, V.V. Bel'kov, P. Olbrich, W. Eder, D.R. Yakovlev, V. Kolkovsky, W. Zaleszczyk, G. Karczewski, T. Wojtowicz, and D. Weiss, *Spin currents in diluted magnetic semiconductors*, *Phys. Rev. Lett.* **102**, 156602 (2009).

[21] E.L. Ivchenko and S.D. Ganichev, *Spin Physics in Semiconductors*. Springer, Berlin, 2008. (ed. M. I. Dyakonov).

[22] L.D. Landau, E.M. Lifshits, and L.P. Pitaevskii, *Electrodynamics of Continues Media*. Elsevier, Amsterdam, 1984.

[23] J.F. Nye, *Physical Properties of Crystals: Their Representation by Tensors and Matrices*. Oxford Univ. Press, Oxford, 1985.

[24] V.M. Agranovich and V.L. Ginzburg, *Crystal Optics with Spatial Dispersion, and Excitons*. Springer, Berlin, 1984. (Springer Series in Solid-State Sciences Vol. 42).

[25] V.A. Kizel', Yu.I. Krasilov, and V.I. Burkov, *Experimental studies of crystal gyrotropy*, *Usp. Fiz. Nauk* **114**, 295 (1974).

[26] J. Jerphagnon and D.S. Chemla, *Optical activity of crystals*, *J. Chem. Phys.* **65**, 1522 (1976).

[27] J. Singh, *Electronic and Optoelectronic Properties of Semiconductor Structures*. Cambridge Univ. Press, New York, 2003.

[28] Ch. Schüller, *Inelastic Light Scattering of Semiconductor Nanostructures: Fundamentals and Recent Advances*. Springer Tracts in Modern Physics. Springer, Berlin, 2006.

[29] S.D. Ganichev, V.V. Bel'kov, L.E. Golub, E.L. Ivchenko, Petra Schneider, S. Giglberger, J. Eroms, J. De Boeck, G. Borghs, W. Wegscheider, D. Weiss, and W. Prettl, *Experimental Separation of Rashba and Dresselhaus Spin Splittings in Semiconductor Quantum Wells*, *Phys. Rev. Lett.* **92**, 256601 (2004).

[30] V.V. Bel'kov, S.D. Ganichev, E.L. Ivchenko, S.A. Tarasenko, W. Weber, S. Giglberger, M. Olteanu, H.-P. Tranitz, S.N. Danilov, Petra Schneider,

W. Wegscheider, D. Weiss, and W. Prettl, *Magneto-gyrotropic photogalvanic effects in semiconductor quantum wells*, *J. Phys.: Condens. Matter* **17**, 3405 (2005).

[31] P. Olbrich, J. Allerdings, V.V. Bel'kov, S.A. Tarasenko, D. Schuh, W. Wegscheider, T. Korn, C. Schüller, D. Weiss, and S.D. Ganichev, *Magnetogyrotropic photogalvanic effect and spin dephasing in (110)-grown $GaAs/Al_xGa_{1-x}As$ quantum well structures*, *Phys. Rev. B* **79**, 245329 (2009).

[32] V. Lechner, L.E. Golub, P. Olbrich, S. Stachel, D. Schuh, W. Wegscheider, V.V. Bel'kov, and S.D. Ganichev, *Tuning of structure inversion asymmetry by the δ-doping position in (001)-grown GaAs quantum wells*, *Appl. Phys. Lett.* **94**, 242109 (2009).

[33] V.V. Bel'kov and S.D. Ganichev, *Magneto-gyrotropic effects in semiconductor quantum wells*, *Semicond. Sci. Technol.* **23**, 114003 (2008).

[34] M.I. D'yakonov and V.I. Perel', *Possibility of orienting electron spins with current*, *JETP Lett.* **13**, 467 (1971).

[35] F. Meier and B.P. Zakharchenya, *Optical Orientation (Modern Problems in Condensed Matter Sciences)*. North-Holland Physics Publishing, Amsterdam, 1984. (ed. F. Meier and B.P. Zakharchenya).

[36] G.L. Bir, A.G. Aronov, and G.E. Pikus, *Spin relaxation of electrons scattered by holes*, *Zh. Eksp. Teor. Fiz.* **69**, 1382 (1975).

[37] T. Adachi, Y. Ohno, F. Matsukura, and H. Ohno, *Spin relaxation in n-modulation doped GaAs/AlGaAs (110) quantumwells*, *Physica E* **10**, 36 (2001). [Sov. Phys. JETP 42, 705 (1975)].

[38] S. Döhrmann, D. Hägele, J. Rudolph, M. Bichler, D. Schuh, and M. Oestreich, *Anomalous Spin Dephasing in (110) GaAs Quantum Wells: Anisotropy and Intersubband Effects*, *Phys. Rev. Lett.* **93**, 147405 (2004).

[39] W.J.H. Leyland, G.H. John, R.T. Harley, M.M. Glazov, E.L. Ivchenko, D.A. Ritchie, I. Farrer, A.J. Shields, and M. Henini, *Enhanced spin-relaxation time due to electron-electron scattering in semiconductor quantum wells*, *Phys. Rev. B* **75**, 165309 (2007).

[40] J.K. Furdyna, *Diluted Magnetic Semiconductors*, *J. Appl. Phys.* **64**, R29 (1988).

[41] Y.R. Lee, A.K. Ramdas, and R.L. Aggarwal, *Origin of the Mn^{2+} optical transition in Mn-based II-VI diluted magnetic semiconductors*, *Phys. Rev. B* **33**, 7383 (1986).

[42] J.A. Gaj, W. Grieshaber, C. Bodin-Deshayes, J. Cibert, G. Feuillet, Y. Merle d'Aubigné, and A. Wasiela, *Magneto-optical study of interface mixing in the CdTe-(Cd,Mn)Te system*, *Phys. Rev. B* **50**, 5512 (1994).

[43] S.D. Ganichev and W. Prettl, *Intense Terahertz Excitation of Semiconductors*. Oxford Univ. Press, Oxford, 2006.

[44] E. Bründermann and H.P. Röser, *First operation of a far-infrared p-germanium laser in a standard close-cycle machine at 15 K*, *Infrared Physics and Technology* **38**, 201 (1997).

[45] C.A. Brau, *Free-Electron Lasers*, *Science* **239**, 1115 (1988).

[46] J. Faist, F. Capasso, D.L. Sivco, C. Sirtori, A.L. Hutchinson, and A.Y. Cho, *Quantum Cascade Laser*, *Science* **264**, 553 (1994).

[47] M. Hangyo, M. Tani, and T. Nagashima, *Terahertz Time-Domain Spectroscopy of Solids: A Review*, *International Journal of Infrared and Millimeter Waves* **26**, 1661 (2005).

[48] G.W. Chantry, *Long-wave optics Vol. 2: Applications*. Academic Press, London, 1984.

[49] P.K. Cheo, *Handbook of molecular lasers*. Marcel Dekker Inc, New York, 1987.

[50] E.V. Loewenstein, R.R. Smith, and R.L. Morgan, *Optical Constants of Far Infrared Materials. 2: Crystalline Solids*, *Applied Optics* **12**, 398 (1973).

[51] F. Brehat and B. Wyncke, *Measurement of the optical constants of crystal quartz at 10 K and 300 K in the far infrared spectral range*, *International Journal of Infrared and Millimeter Waves* **18**, 1663 (1997).

[52] S.D. Ganichev, W. Weber, J. Kiermaier, S.N. Danilov, P. Olbrich, D. Schuh, W. Wegscheider, D. Bougeard, G. Abstreiter, and W. Prettl, *All-electric detection of the polarization state of terahertz laser radiation*, *J. Appl. Phys.* **103**, 114504 (2008).

[53] S.N. Danilov, B. Wittmann, P. Olbrich, W. Eder, W. Prettl, L.E. Golub, E.V. Beregulin, Z.D. Kvon, N.N. Mikhailov, S.A. Dvoretsky, V.A. Shalygin, N.Q. Vinh, A.F.G. van der Meer, B. Murdin, and S.D. Ganichev, *Fast detector of the ellipticity of infrared and terahertz radiation based on HgTe quantum well structures*, *J. Appl. Phys.* **105**, 013106 (2009).

[54] S.A. Crooker, D.A. Tulchinsky, J. Levy, D.D. Awschalom, R. Garcia, and N. Samarth, *Enhanced Spin Interactions in Digital Magnetic Heterostructures*, *Phys. Rev. Lett.* **75**, 505 (1995).

[55] J.C. Egues and J.W. Wilkins, *Spin-dependent phenomena in digital-magnetic heterostructures: Clustering and phase-space filling effects*, *Phys. Rev. B* **58**, R16012 (1998).

[56] J. Jaroszynski, T. Andrearczyk, G. Karczewski, J. Wróbel, T. Wojtowicz, E. Papis, E. Kaminska, A. Piotrowska, D. Popovic, and T. Dietl, *Ising Quantum Hall Ferromagnet in Magnetically Doped Quantum Wells*, *Phys. Rev. Lett.* **89**, 266802 (2002).

[57] M.K. Kneip, D.R. Yakovlev, M. Bayer, G. Karczewski, T. Wojtowicz, and J. Kossut, *Engineering of spin-lattice relaxation dynamics by digital growth of diluted magnetic semiconductor CdMnTe*, *Appl. Phys. Lett.* **88**, 152105 (2006).

[58] D. Keller, D.R. Yakovlev, G.V. Astakhov, W. Ossau, S.A. Crooker, T. Slobodskyy, A. Waag, G. Schmidt, and L.W. Molenkamp, *Magneto-optics of two-dimensional electron gases modified by strong Coulomb interactions in ZnSe quantum wells*, *Phys. Rev. B* **72**, 235306 (2005).

[59] P. Olbrich, E.L. Ivchenko, R. Ravash, T. Feil, S.D. Danilov, J. Allerdings, D. Weiss, D. Schuh, W. Wegscheider, and S.D. Ganichev, *Ratchet Effects Induced by Terahertz Radiation in Heterostructures with a Lateral Periodic Potential*, *Phys. Rev. Lett.* **103**, 090603 (2009).

[60] P. Olbrich, E.L. Ivchenko, R. Ravash, T. Feil, S. D. Danilov, J. Allerdings, D. Weiss, D. Schuh, W. Wegscheider, and S.D. Ganichev, *Erratum: Ratchet Effects Induced by Terahertz Radiation in Heterostructures with a Lateral Periodic Potential [Phys. Rev. Lett. 103, 090603 (2009)]*, *Phys. Rev. Lett.* **103**, 199901 (2009).

[61] S. Adachi and K. Oe, *Chemical Etching Characteristics of (001)GaAs*, *J. Electrochem. Soc.* **130**, 2427 (1983).

[62] S.D. Ganichev, E.L. Ivchenko, V.V. Bel'kov, S.A. Tarasenko, M. Sollinger, D. Weiss, W. Wegscheider, and W. Prettl, *Spin-galvanic effect*, *Nature* **417**, 153 (2002).

[63] T.C. Damen, L. Viña, J.E. Cunningham, J.E. Shah, and L.J. Sham, *Subpicosecond spin relaxation dynamics of excitons and free carriers in GaAs quantum wells*, *Phys. Rev. Lett.* **67**, 3432 (1991).

[64] G.M. Müller, M. Römer, D. Schuh, W. Wegscheider, J. Hübner, and M. Oestreich, *Spin Noise Spectroscopy in GaAs (110) Quantum Wells: Access to Intrinsic Spin Lifetimes and Equilibrium Electron Dynamics*, *Phys. Rev. Lett.* **101**, 206601 (2008).

[65] D. Stich, J. Zhou, T. Korn, R. Schulz, D. Schuh, W. Wegscheider, M.W. Wu, and C. Schüller, *Effect of Initial Spin Polarization on Spin Dephasing and the Electron g Factor in a High-Mobility Two-Dimensional Electron System*, *Phys. Rev. Lett.* **98**, 176401 (2007).

[66] P.S. Eldridge, W.J.H. Leyland, J.D. Mar, P.G. Lagoudakis, R. Winkler, O.Z. Karimov, M. Henini, D. Taylor, R.T. Phillips, and R.T. Harley, *Absence of the Rashba effect in undoped asymmetric quantum wells*, *arXiv* 0807.4845 (2008).

[67] P.S. Eldridge, W.J.H. Leyland, P.G. Lagoudakis, O.Z. Karimov, M. Henini, D. Taylor, R.T. Phillips, and R.T. Harley, *All-optical measurement of Rashba coefficient in quantum wells*, *Phys. Rev. B* **77**, 125344 (2008).

[68] S. Giglberger, L.E. Golub, V.V. Bel'kov, S.N. Danilov, D. Schuh, C. Gerl, F. Rohlfing, J. Stahl, W. Wegscheider, D. Weiss, W. Prettl, and S.D. Ganichev, *Rashba and Dresselhaus spin splittings in semiconductor quantum wells measured by spin photocurrents*, *Phys. Rev. B* **75**, 035327 (2007).

[69] L. Pfeiffer, K.W. West, H.L. Stormer, J.P. Eisenstein, K.W. Baldwin, D. Gershoni, and J. Spector, *Formation of a high quality two-dimensional electron gas on cleaved GaAs*, *Appl. Phys. Lett.* **56**, 1697 (1990).

[70] S.A. Tarasenko, *Electron scattering in quantum wells subjected to an in-plane magnetic field*, *Phys. Rev. B* **77**, 085328 (2008).

[71] C. Gorini, P. Schwab, M. Dzierzawa, and R. Raimondi, *Spin polarizations and spin Hall currents in a two-dimensional electron gas with magnetic impurities*, *Phys. Rev. B* **78**, 125327 (2008).

[72] A.A. Sirenko, T. Ruf, M. Cardona, D.R. Yakovlev, W. Ossau, A. Waag, and G. Landwehr, *Electron and hole g factors measured by spin-flip Raman scattering in* $CdTe/Cd_{1-x}Mg_xTe$ *single quantum wells*, *Phys. Rev. B* **56**, 2114 (1997).

[73] D. Keller, D.R. Yakovlev, B. König, W. Ossau, Th. Gruber, A. Waag, L.W. Molenkamp, and A.V. Scherbakov, *Heating of the magnetic ion system in (Zn, Mn)Se/(Zn, Be)Se semimagnetic quantum wells by means of photoexcitation*, *Phys. Rev. B* **65**, 035313 (2002).

[74] S.D. Ganichev, S.A. Tarasenko, V.V. Bel'kov, P. Olbrich, W. Eder, D.R. Yakovlev, V. Kolkovsky, W. Zaleszczyk, G. Karczewski, T. Wojtowicz, and D. Weiss, *Spin currents in diluted magnetic semiconductors*, *arXiv: cond-mat* 0811.4327 (2009).

[75] D. Weiss, K.V Klitzing, K. Ploog, and G. Weimann, *Magnetoresistance Oscillations in a Two-Dimensional Electron Gas Induced by a Submicrometer Periodic Potential*, *Europhys. Lett.* **8**, 8 (1989).

[76] M. Tornow, D. Weiss, A. Manolescu, R. Menne, K. v. Klitzing, and G. Weimann, *Even-odd filling-factor switching in one-dimensional lateral superlattices*, *Phys. Rev. B* **54**, 16397 (1996).

[77] P. Reimann, *Brownian motors: Noisy transport far from equilibrium*, *Phys. Rep.* **361**, 57 (2002).

[78] E.M. Baskin, L.I. Magarill, and M.V. Entin, *Photogalvanic effect in crystals without inversion center*, *Phys. Sol. State* **20**, 1403 (1978).

[79] V.I. Belinicher and B.I. Sturman, *The photogalvanic effect in media lacking a center of symmetry*, *Phys. Usp.* **23**, 199 (1980).

[80] P. Hänggi, F. Marchesoni, and F. Nori, *Brownian Motors*, *Ann. Phys.* **14**, 51 (2005).

[81] P. Reimann, M. Grifoni, and P. Hänggi, *Quantum Ratchets*, *Phys. Rev. Lett.* **79**, 10 (1997).

[82] A. Lorke, S. Wimmer, B. Jager, J.P. Kotthaus, W. Wegscheider, and M. Bichler, *Far-Infrared and Transport Properties of Antidot Arrays with Broken Symmetry*, *Physica B* **249**, 312 (1998).

[83] H. Linke, T.E. Humphrey, A. Lofgren, A.O. Sushkov, R. Newbury, R.P. Taylor, and P. Omling, *Experimental Tunneling Ratchets*, *Science* **286**, 2314 (1999).

[84] A.M. Song, P. Omling, L. Samuelson, W. Seifert, I. Shorubalko, and H. Zirath, *Room-temperature and 50 GHz operation of a functional nanomaterial*, *Appl. Phys. Lett.* **79**, 1357 (2001).

[85] J.B. Majer, J. Peguiron, M. Grifoni, M. Tusveld, and J.E. Mooij, *Quantum Ratchet Effect for Vortices*, *Phys. Rev. Lett.* **90**, 056802 (2003).

[86] L.I. Magarill, *Photogalvanic effect in asymmetric lateral superlattice*, *Physica E* **9**, 652 (2001).

[87] A.D. Chepelianskii, M.V. Entin, L.I. Magarill, and D.L. Chepelyansky, *Photogalvanic current in artificial asymmetric nanostructures*, *Eur. Phys. J. B* **56**, 323 (2007).

[88] W. Weber, L.E. Golub, S.N. Danilov, J. Karch, C. Reitmaier, B. Wittmann, V.V. Bel'kov, E.L. Ivchenko, Z.D. Kvon, N.Q. Vinh, A.F.G. van der Meer, B. Murdin, and S.D. Ganichev, *Quantum ratchet effects induced by terahertz radiation in GaN-based two-dimensional structures*, *Phys. Rev. B* **77**, 245304 (2008).

[89] M. Büttiker, *Transport as a Consequence of State-Dependent Diffusion*, *Z. Phys. B* **68**, 161 (1987).

[90] Y.M. Blanter and M. Büttiker, *Rectification of Fluctuations in an Underdamped Ratchet*, *Phys. Rev. Lett.* **81**, 4040 (1998).

[91] S.D. Ganichev, S.N. Danilov, J. Eroms, W. Wegscheider, D. Weiss, W. Prettl, and E.L. Ivchenko, *Conversion of Spin into Directed Electric Current in Quantum Wells*, *Phys. Rev. Lett.* **86**, 4358 (2001).

[92] P. Olbrich, S.A. Tarasenko, C. Reitmaier, J. Karch, D. Plohmann, Z.D. Kvon, and S.D. Ganichev, *Observation of the orbital circular photogalvanic effect*, *Phys. Rev. B* **79**, 121302 (2009).

Danksagung

Ich möchte mich an dieser Stelle recht herzlich bei allen bedanken, die mir während meiner Doktorarbeit mit Rat und Tat zur Seite standen.

Besonderer Dank geht an Herrn Prof. Sergey D. Ganichev der mir die Möglichkeit gab diese Doktorarbeit in seiner Arbeitsgruppe durchzuführen. Er hat sich immer Zeit genommen meine Fragen zu beantworten und eingehend zu erklären.

Im weiteren möchte ich mich bei meinen Eltern dafür bedanken, dass sie mir mein Studium ermöglicht haben, sowie meinem Bruder Alex und seiner Frau Lisa, die mich motiverten Physik zu studieren ☺. Auch bei meinen Geschwistern Sabine und Thomas möchte ich für ihre Unterstützung bedanken.

Einen weiteren Dank möchte ich an Herrn Dr. Sergey Danilov und Herrn Prof. Dr. Vasily Bel'kov aussprechen, die mir bezüglich des experimentellen Aufbaus und der durchgeführten Experimente immer gute und nützliche Ratschläge erteilen konnten. Ganz herzlich möchte ich mich auch für die theoretische Unterstützung von Prof. Dr. Eugeneous Ivchenko, Prof. Dr. Sergey Tarasenko und Prof. Dr. Leonid Golub.

Auch bei meinen Kollegen in der Arbeitsgruppe und allen Ehemaligen, die stets für eine gute Stimmung und Zusammenarbeit sorgten, möchte ich mich herzlichst bedanken. Ich danke hierbei Johannes Karch (Vielen Dank auch fürs Korretkturlesen!), Christoph Drexler, Vera Lechner, Sebastian Stachel, Christina Zoth, Ines Caspers, Josef Kamann, Cynthia Karl, Faina Lomakina, Thomas Stangl, Markus Fehrenbacher, Wolfgang Eder, Christoph Brinsteiner, Michael Schmalzbauer, Juri Allerdings, Wolfgang Weber, Bernhard Wittmann, Helgi Diehl und Thomas Schönberger. Besonderer Dank geht auch an Anton Humbs für die Hilfe bei technischen Problemen, sowie Ulla Turba und Hannelore Lanz für die Unterstützung bei formalen Problemen.

Zuguterletzt möchte ich mich bei meiner Freundin Antje Kunze für ihre Unterstüzung bedanken.